

## **INFORMATION TO USERS**

This manuscript has been reproduced from the microfilm master. UMI films the text directly from the original or copy submitted. Thus, some thesis and dissertation copies are in typewriter face, while others may be from any type of computer printer.

**The quality of this reproduction is dependent upon the quality of the copy submitted.** Broken or indistinct print, colored or poor quality illustrations and photographs, print bleedthrough, substandard margins, and improper alignment can adversely affect reproduction.

In the unlikely event that the author did not send UMI a complete manuscript and there are missing pages, these will be noted. Also, if unauthorized copyright material had to be removed, a note will indicate the deletion.

Oversize materials (e.g., maps, drawings, charts) are reproduced by sectioning the original, beginning at the upper left-hand corner and continuing from left to right in equal sections with small overlaps.

Photographs included in the original manuscript have been reproduced xerographically in this copy. Higher quality 6" x 9" black and white photographic prints are available for any photographs or illustrations appearing in this copy for an additional charge. Contact UMI directly to order.

ProQuest Information and Learning  
300 North Zeeb Road, Ann Arbor, MI 48106-1346 USA  
800-521-0600

**UMI<sup>®</sup>**



**University of Alberta**

**Geology and Geochemistry of the Mallery Lake Precious Metal-Bearing  
Epithermal System, Nunavut, Canada**

by

William Allan Turner



A thesis submitted to the Faculty of Graduate Studies and Research in partial  
fulfillment of the requirements for the degree of Master of Science

**Department of Earth and Atmospheric Sciences**

**Edmonton, Alberta**

**Spring 2000**



**National Library  
of Canada**

**Acquisitions and  
Bibliographic Services**

**395 Wellington Street  
Ottawa ON K1A 0N4  
Canada**

**Bibliothèque nationale  
du Canada**

**Acquisitions et  
services bibliographiques**

**395, rue Wellington  
Ottawa ON K1A 0N4  
Canada**

*Your file Votre référence*

*Our file Notre référence*

**The author has granted a non-exclusive licence allowing the National Library of Canada to reproduce, loan, distribute or sell copies of this thesis in microform, paper or electronic formats.**

**The author retains ownership of the copyright in this thesis. Neither the thesis nor substantial extracts from it may be printed or otherwise reproduced without the author's permission.**

**L'auteur a accordé une licence non exclusive permettant à la Bibliothèque nationale du Canada de reproduire, prêter, distribuer ou vendre des copies de cette thèse sous la forme de microfiche/film, de reproduction sur papier ou sur format électronique.**

**L'auteur conserve la propriété du droit d'auteur qui protège cette thèse. Ni la thèse ni des extraits substantiels de celle-ci ne doivent être imprimés ou autrement reproduits sans son autorisation.**

**0-612-60205-2**

**University of Alberta**

**Library Release Form**

**Name of Author:** William A. Turner

**Title of Thesis:**       **Geology and Geochemistry of the Mallery Lake  
Precious Metal-Bearing Epithermal System, Nunavut,  
Canada**

**Degree:** Master of Science

**Year this Degree was Granted:** 2000

Permission is hereby granted to the University of Alberta Library to reproduce single copies of this thesis and to lend or sell such copies for private, scholarly, or scientific research purposes only.

The author reserves all other publication and other rights in association with the copyright in the thesis, and except as hereinbefore provided, neither the thesis nor any substantial portion thereof may be printed or otherwise reproduced in any material form whatever without the author's prior written permission.



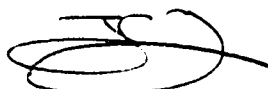
9235 - 117 St.  
Edmonton, Alberta  
Canada  
T6G 1S3

Date Jun 5/2000

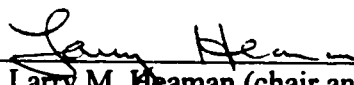
**University of Alberta**

**Faculty of Graduate Studies and Research**

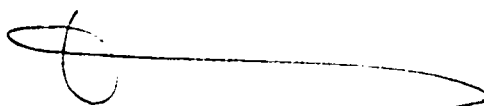
The undersigned certify that they have read, and recommended to the Faculty of Graduate Studies and Research for acceptance, a thesis entitled **Geology and Geochemistry of the Mallery Lake Precious Metal-Bearing Epithermal System, Nunavut, Canada** submitted by William A. Turner in partial fulfillment of the requirements for the degree of Master of Science.



\_\_\_\_\_  
Dr. Jeremy R. Richards (supervisor)



\_\_\_\_\_  
Dr. Larry M. Heaman (chair and examiner)



\_\_\_\_\_  
Dr. Karlis Muehlenbachs (committee member)



\_\_\_\_\_  
Dr. Moritz Heimpel (committee member)

Date 4 Jan 2000

## **Dedication**

**To Bruce Nesbitt,  
James Morris,  
Doug and Olive Turner**

## **Abstract**

The Mallery Lake precious metal-bearing vein system, located in Nunavut, Canada, is hosted by  $1706 \pm 7$  Ma Pitz Formation rhyodacite flows. Fluorite from the deposit gives an Sm-Nd fluorite age of  $1435 \pm 21$  Ma, making this one of the oldest pristine epithermal systems in the world. The veins display primary and secondary silica textures, and are associated with phyllic, propylitic, and minor argillic alteration.

Two fluid inclusion populations were identified in the veins. Type 1 fluid inclusions are dilute ( $<3$  wt. % NaCl) with moderate temperatures ( $150^\circ\text{C}$  to  $200^\circ\text{C}$ ), and show textural evidence of boiling and/or the presence of trace  $\text{CO}_2$ . Type 2 fluid inclusions contain saline (23 to 31 wt. %  $\text{CaCl}_2$ -NaCl), oxidized, slightly acidic, lower temperature ( $90^\circ\text{C}$  to  $150^\circ\text{C}$ ) fluids that are linked to precious metal transport.

The approximate 270 m.y. age difference between the precious metal deposit and the Pitz Formation host rocks suggests the involvement of a later regional thermal event in driving the hydrothermal system, unrelated to the early Proterozoic volcanic activity.



# **TABLE OF CONTENTS**

## **CHAPTER 1**

### **INTRODUCTION**

Introduction (1)

Classification of epithermal systems (2)

## **CHAPTER 2**

### **GENERAL GEOLOGY OF THE BAKER LAKE AND THELON BASINS**

Introduction (4)

Archean and early Proterozoic Group (4)

Dubawnt Supergroup (7)

Baker Lake Group (7)

Wharton Group (10)

Barrenland Group (11)

## **CHAPTER 3**

### **PETROLOGY, ALTERATION, AND BASE AND PRECIOUS METALS ASSOCIATED WITH THE PITZ FORMATION RHYOLITE FLOWS**

Exploration in the Mallery Lake area since 1995 (12)

Pitz Formation (15)

Pitz Formation petrology (15)

Phenocryst assemblage (15)

Accessory mineral assemblage (18)

Textures of the Pitz Formation rhyolite flows (19)

Observations (22)

Discussion (22)

Alteration of the Chalcidonic Stockwork Zone (28)

Petrographic evidence of base and precious metal association in the hydrothermal veins (33)

Observations (33)

## **CHAPTER 4**

### **TEXTURES OF BARREN AND PRECIOUS METAL BEARING VEINS**

Introduction (42)

Observations (42)

Quartz textures interpretation (45)

Primary textures (Type A) (45)

Secondary Textures (Type B) (45)

Replacement textures (54)

Recrystallization textures (74)

## **CHAPTER 5**

### **FLUID INCLUSION STUDY OF THE HYDROTHERMAL VEINS AT MALLERY LAKE**

Introduction (75)

Methodology (75)

Criteria for selection of fluid inclusions (76)

Fluid inclusion type classification (77)

    Type 1 dilute fluid inclusions (77)

        Results (80)

            Type 1A fluid inclusions (80)

            Type 1B fluid inclusions (80)

            Type 1C fluid inclusions (95)

        Discussion (95)

    Type 2 saline fluid inclusions (100)

        Non-destructive analysis: melting behavior in mixed salt system (101)

            Stable CaCl<sub>2</sub>-hydrate melting behavior (104)

            Metastable CaCl<sub>2</sub>-hydrate melting behavior (104)

        Behavior of the mixed salt-hydrates of the Type 2 fluids (107)

            Results (107)

            Discussion (108)

    Association of fluid inclusion types with precious metal deposition (113)

## **CHAPTER 6**

### **STABLE ISOTOPE ANALYSIS OF HYDROTHERMAL VEINS IN THE MALLERY LAKE AREA**

Introduction (116)

Stable isotope systematics and errors (116)

    Expression of isotope ratios (116)

    Isotope fractionation (117)

Sample selection (118)

Analytical procedure (120)

Results (121)

    Isotopic composition of the fluid (123)

Discussion (124)

## **CHAPTER 7**

### **RADIOGENIC ANALYSIS OF THE PITZ FORMATION AND NUEL TIN INTRUSIVE SUITE IN THE MALLERY LAKE AREA**

Introduction (129)

Analytical procedures (129)

Results (130)

Discussion (134)

## **CHAPTER 8**

### **Sm-Nd ANALYSIS OF HYDROTHERMAL FLUORITE IN THE MALLERY LAKE AREA**

Introduction (135)

Isotope calculations and notation (136)

Samples (137)

REE analysis (137)

Sm-Nd analytical procedures (140)

Results (141)

Isotopic ratios (Integrity of the isochron) (141)

Initial Nd isotopic compositions (146)

## **CHAPTER 9**

### **DISCUSSION**

Metal transport and deposition in the ore-bearing fluid at Mallery Lake (148)

Metal ligand classification (148)

Physical-chemical conditions of the ore-bearing fluid (149)

Solubility and metal transport (150)

Mechanisms of precious metal deposition (151)

Comparison of the Mallery Lake vein system to Phanerozoic low sulfidation epithermal systems (155)

Age of the hydrothermal system (158)

## **CHAPTER 10**

### **CONCLUSIONS (162)**

### **REFERENCES (165 – 176)**

## **LIST OF TABLES**

- Table 2.1. Stratigraphy of the regional geological units (5)
- Table 3.1. ICP whole rock analysis through Lithium Metaborate Fusion for both altered and unaltered Pitz Formation rhyolite flows (17)
- Table 3.2. XRD analytical results of Chalcedonic Stockwork Zone samples (31)
- Table 3.3. Au, Ag, and Cu abundance obtained from EDS microprobe analysis of precious metal grains that were analysed from veins in the Chalcedonic Stockwork Zone (36)
- Table 5.1. Microthermometric measurements of the veins in the Mallery Lake area (80)
- Table 6.1. Oxygen (silica) and Deuterium (fluid inclusion) stable isotope data (117)
- Table 6.2. Average trapping temperatures (Tt) and calculated  $\delta^{18}\text{O}$  water values of two possible fluids that may have been involved in forming the veins in the Mallery Lake area (122)
- Table 7.1. U-Pb isotopic data of zircon fractions from Pitz Formation rhyodacite (ATPR-2) and Nueltin syenite (ATSD-1) (129)
- Table 8.1. Fluorite rare earth elements normalized to chondritic elemental values (138)
- Table 8.2. Sm-Nd fluorite data (Mallery Lake) (142)
- Table 8.3. 79LAA-T250 Pitz Formation (147)
- Table 9.1. Classification of some metals and ligands in terms of Class “a” and “b” behavior (149)
- Table 9.2. Comparison of the Mallery Lake epithermal system to four Phanerozoic low sulfidation epithermal systems (156)
- Table 9.3. Hydrothermal events recorded in the vicinity of the mid Proterozoic Thelon Basin (160)

## LIST OF FIGURES

- Figure 2.1. Simplified map of the regional geology of the central Churchill Province (6)
- Figure 3.1. Mallery Lake, Nunavut: Regional geology and vein classification (13)
- Figure 3.2. Mallery Lake peninsula geology and vein type classification (14)
- Figure 3.3. Chaledonic Stockwork Zone: Geology, sample locations, alteration, and vein classification (front cover pocket of thesis)
- Figure 3.4. IUGS classification of the Pitz Formation (16)
- Figure 4.1a. Classification of primary (Type A) silica textures (41)
- Figure 4.1b. Classification of secondary (Type B) silica textures (42)
- Figure 5.1. Frequency of the homogenization temperatures for fluid Types 1 and 2 (79)
- Figure 5.2. Melt behavior of the stable NaCl-CaCl<sub>2</sub>-H<sub>2</sub>O ternary fluid system (104)
- Figure 5.3. Hydrohalite stability field for Type 2 fluids (107)
- Figure 5.4. Precious metals associated with decrepitation residue (Sample 703534) (113)
- Figure 6.1.  $\delta^{18}\text{O}$  isotopic composition of quartz from the Mallery Lake veins (120)
- Figure 6.2. Possible isotopic compositions of fluids from the Mallery Lake epithermal system (126)
- Figure 7.1. U-Pb host rock ages (131)
- Figure 8.1. Rare earth element pattern of four fluorite samples from the Mallery Lake epithermal system (139)
- Figure 8.2.  $^{147}\text{Sm}/^{144}\text{Nd}$  versus  $^{143}\text{Nd}/^{144}\text{Nd}$  isochron diagram for 12 fluorite vein samples from the Mallery Lake area (143)
- Figure 8.3.  $^{143}\text{Nd}/^{144}\text{Nd}$  vs. 1/Nd (ppm) (144)
- Figure 9.1a,b. Log fH<sub>2</sub>-pH gold solubility diagrams (153)

## **LIST OF PLATES**

<b>Plate 3.1</b> .....	<b>21</b>
<b>Plate 3.2</b> .....	<b>23</b>
<b>Plate 3.3</b> .....	<b>26</b>
<b>Plate 3.4</b> .....	<b>28</b>
<b>Plate 3.5</b> .....	<b>33</b>
<b>Plate 3.6</b> .....	<b>38</b>
<b>Plate 4.1</b> .....	<b>45</b>
<b>Plate 4.2</b> .....	<b>47</b>
<b>Plate 4.3</b> .....	<b>49</b>
<b>Plate 4.4</b> .....	<b>51</b>
<b>Plate 4.5</b> .....	<b>54</b>
<b>Plate 4.6</b> .....	<b>57</b>
<b>Plate 4.7</b> .....	<b>59</b>
<b>Plate 4.8</b> .....	<b>61</b>
<b>Plate 4.9</b> .....	<b>63</b>
<b>Plate 4.10</b> .....	<b>65</b>
<b>Plate 4.11</b> .....	<b>67</b>
<b>Plate 4.12</b> .....	<b>69</b>
<b>Plate 4.13</b> .....	<b>71</b>
<b>Plate 5.1</b> .....	<b>77</b>
<b>Plate 5.2</b> .....	<b>88</b>
<b>Plate 5.3</b> .....	<b>90</b>
<b>Plate 5.4</b> .....	<b>92</b>
<b>Plate 5.5</b> .....	<b>95</b>
<b>Plate 5.6</b> .....	<b>97</b>
<b>Plate 5.7</b> .....	<b>101</b>
<b>Plate 5.8</b> .....	<b>110</b>

## **CHAPTER 1**

### **INTRODUCTION**

This MSc project focuses on the geological and geochemical evolution of a middle Proterozoic epithermal gold occurrence. Typically, epithermal gold deposits are produced by the shallow circulation of moderate temperature (< 250 - 350°C) hydrothermal fluids in volcanic-plutonic terranes. The aim of the project is to examine the Mallery Lake gold occurrence in Nunavut, Canada, to understand better the development of Precambrian epithermal systems. Most known epithermal gold deposits are younger than 200 million years, with a few (i.e. the Hope Brook deposit, Canada and the Enåsen gold deposit, central Sweden) dating back to the Precambrian (Dube *et al.*, 1998; Hallberg, 1994). Typically, the ancient epithermal examples have been extensively metamorphosed and overprinted, and therefore provide poor material for study. The Mallery Lake epithermal system, hosted by mid-Proterozoic volcanic and sedimentary rocks, has undergone little deformation, metamorphism, or alteration since emplacement, and is thus relatively pristine. This deposit therefore provides an excellent opportunity to study an ancient epithermal system.

The fundamental question to be addressed by this thesis is: Are the processes that formed this ancient deposit similar or different to those that formed epithermal gold systems during the Phanerozoic? An understanding of this ancient deposit may lead to better exploration techniques for other Precambrian epithermal systems.

### ***Classification of Epithermal Systems***

Many approaches have been taken to classify epithermal systems based on the differences in fluid chemistry, mineralogy/alteration, and precious metal abundances. Heald *et al.* (1987) used the terms adularia-sericite, and acid -sulphate to describe the differences between two main groups of deposits based largely on mineralogy, alteration assemblages, and spatial zoning. Bonham (1986) proposed a system of classification based on sulfur content of the ore forming fluid (i.e. high and low sulfur contents). The problem with this criterion is that epithermal systems are not homogeneous with respect to their sulfide percentages on a deposit scale, and therefore the depth of erosion of the system will change the perceived economic potential of the system (i.e. if the system is examined at a high level, the system may be incorrectly interpreted to be barren of precious metals).

Berger and Henley (1989) separated the epithermal deposits primarily based on mineralogy rather than fluid chemistry by using the terms kaolinite - alunite and adularia - sericite. The weakness of classifying by mineralogy is: (1) not all adularia - sericite type deposits contain adularia (Sillitoe, 1993); (2) the classification scheme does not take into account late stages of supergene enrichment and the subsequent development of secondary kaolinite - alunite mineralogy.

Classification of epithermal systems in the last five years has focussed on using the redox state of the sulfur as a means of division. By this criterion, epithermal systems are separated into two broad classifications: high sulfidation, and low sulfidation



(Hedenquist, 1987; White and Hedenquist, 1990; Panteleyev, 1994; Evans, 1993; and Sillitoe, 1993). Hedenquist (1987) chose this general classification scheme to refer to the redox state of the sulfur present in the mineralizing fluid, and proposed a secondary description of the form of the deposit (i.e. vein, stockwork, disseminated). Sillitoe (1993) further divided the low sulfidation classification system into three subtypes: sulfide poor (subalkalic rhyolitic rocks); sulfide poor (alkalic rocks); and sulfide rich (subalkalic andesitic to rhyodacitic rocks). Taylor (1996) uses the general classification scheme to define the differences in alteration and ore assemblages based on differences in the acidity and oxidation state of the fluid.

As is obvious by the above discussion, few definitive criteria can be used to classify epithermal systems. Instead of attempting to fit the Mallery Lake epithermal system to a specific model, the characteristics of the system are examined without bias, and a model is proposed to explain the observations.

## **CHAPTER 2**

### **GENERAL GEOLOGY OF THE BAKER LAKE AND THELON BASINS**

#### ***Introduction***

Collision of the Churchill province with the Superior province at approximately 1.8 Ga. resulted in extensive volcanism and sedimentation, causing the Baker Lake and Thelon Basins to be formed (Gall *et al.*, 1992). The Mallery Lake epithermal system is located on the western edge of Baker Lake Basin (Figure 2.1). Gall *et al.* (1992) revised the stratigraphic nomenclature of the lithological units found in the Thelon and Baker Lake Basins, and called them collectively the Dubawnt Supergroup. Lithologically, the basins are filled with sedimentary sequences of redbed conglomerates and arkosic units, as well as intercalated ultrapotassic and rhyolitic volcanic rocks and their intrusive counterparts (Table 2.1). Previous mapping projects have been conducted by the Geological Survey of Canada in the early 1980s as well as regional reconnaissance mapping by Phelps Dodge from 1995 to 1997.

#### ***Archean and Paleoproterozoic Basement***

The basement rocks underlying the Dubawnt Supergroup are Archean to early Proterozoic in age, and have been described by Peterson and Born (1994). The Archean group is comprised of two main rock units: a suite of metasedimentary rocks made up of migmatized biotite schist and a grey psammitic to quartzofeldspathic gneiss; and the Snow Island Intrusive Suite, which comprises four rock units: a basal peridotite unit, an overlying biotite hornblende diorite, crosscutting megacrystic granite, and a late stage

**Table 2.1. Stratigraphy of the regional geological units**

<u>Age</u>	<u>Division</u>	<u>Lithologies</u>
1.72-1.84 Ga.	<b>Dubawnt Supergroup</b>	
1.72 Ga.	<i>Barrenland Group</i> Lookout Point Fm Kuungmi Fm Thelon Fm	Stromatolitic dolostone Aphanitic mafic volcanics Conglomerates, sandstones, siltstones
-----Mattonabee Unconformity-----		
1.75 Ga.	<i>Wharton Group</i> Nueltin Intrusive Suite  Pitz Fm	Granite (rapakivi, miarolitic or porphyritic), syenite, granodiorite.  Rhyolite, rhyodacite and dacite flows, minor tuffs, sandstone and conglomerate.
-----unconformity-----		
1.84 Ga.	<i>Baker Lake Group</i> Kunwak Fm  Christopher Island Fm  Kazan Fm South Channel Fm	Conglomerate, sandstone, rebeds.  Ultrapotassic volcanic flows & pyroclastics (minettes, lamproite), felsic alkaline flows, related volcanoclastic sediments. Arkose. Conglomerate.
-----unconformity-----		
<i>Early Proterozoic</i>	<i>Amer Group</i>	Quartzite, quartz-muscovite schist, chlorite schist
-----unconformity-----		
>2.6 Ga.	<i>Snow Island Intrusive Suite</i>	Peridotite, diorite, granite, leucogranite dyke. Migmatitic and quartzofeldspathic gneisses.

(Adapted from Gall *et al.* (1992) and Biczok (1996))

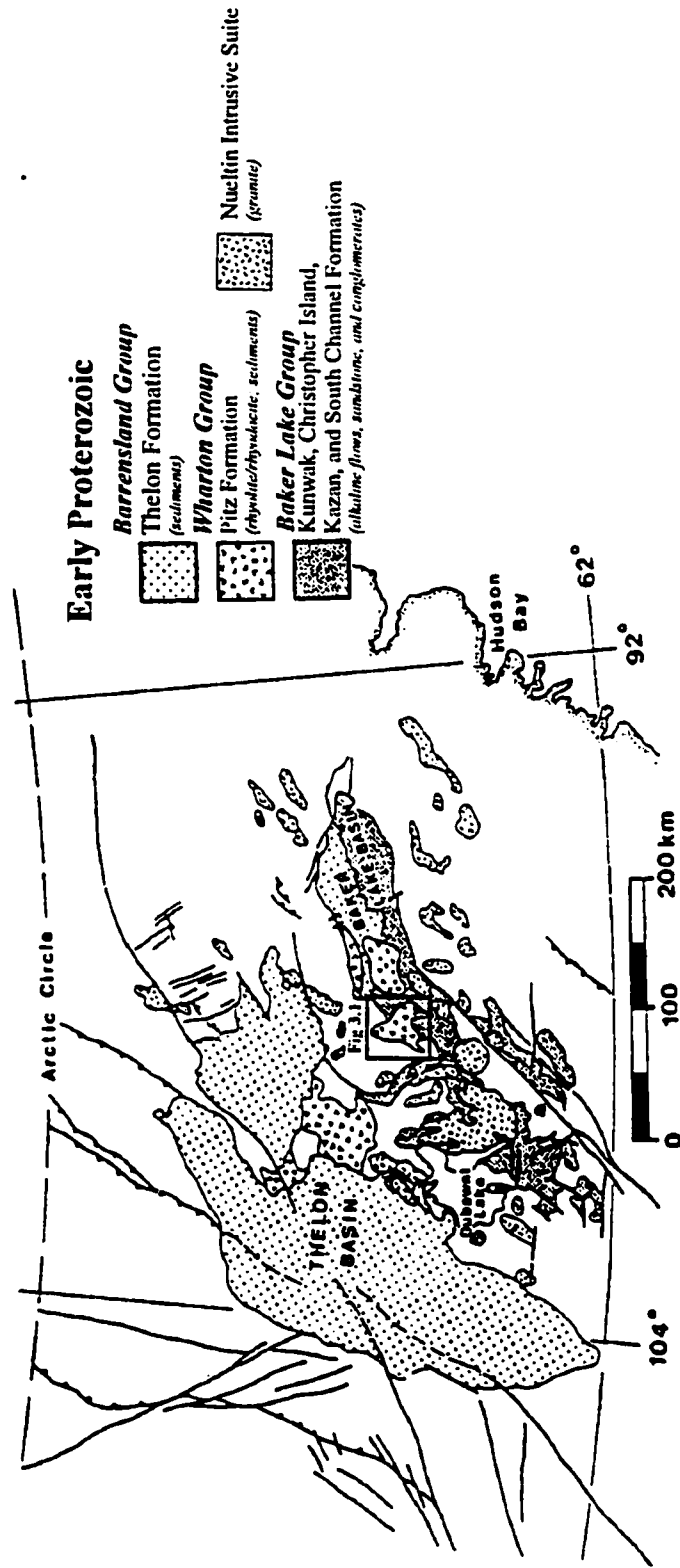


**Figure 2.1.** Simplified map of the regional geology of the central Churchill Province. Location area of the Mallery Lake Epithermal System marked by a box (refer to Figure 3.1 for enlargement of area). Modified from Peterson et al., 1989.

biotite leucogranite dyke. Examination of cross-cutting relationships indicates that there is a distinct mafic to felsic trend with time.

The early Proterozoic Amer Group unconformably overlies the Archean units. This group is composed of three different rock units: a lower section of quartzite, an overlying quartz-muscovite schist, and late-stage chlorite schist. An accurate age for the Amer Group has not been obtained yet. However, in terms of lithology and metamorphic grade it is similar to the Hurwitz Group of the Hearne Province, which has an age greater than 2111 Ma (Aspler, 1989).

### **Dubawnt Supergroup**

#### ***Baker Lake Group***

The Baker Lake Group, which unconformably overlies the Amer Group, consists of four formations: the South Channel, Kazan, Christopher Island, and Kunwak Formations.

The South Channel Formation has a thickness of around 1800 m, and consists of massive, immature, polymictic conglomerate intercalated with sandstone, siltstone, and mudstone lenses, possibly originating from an alluvial fan or braided stream (Blake 1980; Gall *et al.*, 1992).

The Kazan Formation, about 1000 m thick, conformably overlies the South Channel Formation (Gall *et al.*, 1992). The Kazan Formation is composed primarily of medium- to fine-grained maroon, pink, and reddish-brown arkosic sandstones that display

sedimentary structures such as crossbeds, ripple marks, channel scours, and intraformational slumps (Donaldson, 1965; Blake, 1980). Subordinate units in the Kazan Formation include conglomerate lenses, siltstone and mudstone layers, and thin calcarenite beds (Blake, 1980). The siltstone and mudstone layers commonly contain desiccation cracks. These textures associated with the arkosic sandstone and siltstone / sandstone layers indicate not only a strong fluvial component to the Kazan formation, but also evidence of an aeolian environment (Blake, 1980; Gall *et al.*, 1992). An upper section of the Kazan Formation contains a conglomeratic volcanic clast-rich marker bed (Gall *et al.*, 1992).

The Christopher Island Formation (CIF) marks the first period of intense volcanic activity in the stratigraphic sequence of the Baker Lake Group. Previous descriptions of the mineralogy, geology, and tectonic evolution of the CIF have been provided by Donaldson (1965), Blake (1980), LeCheminant *et al.* (1987a), Peterson *et al.* (1989), Peterson and Rainbird (1990), Rainbird and Peterson (1990), Peterson (1992), and Gall *et al.* (1992). Peterson *et al.* (1994) separated the CIF into lower felsic flows, mafic lamprophyre flows, and an upper felsic flow sequence based on studies conducted at Dubawnt Lake. The CIF is up to 2500 m in thickness in some areas (Gall *et al.*, 1992).

The lower felsic flow occurs as subaerial eruptions. Preservation of the lower felsic flows takes the form of domes, pyroclastic flows, and flat-lying flows (Peterson *et al.*, 1994). The mafic lamprophyre flows are intercalated with turbiditic sediments and were erupted subaqueously into deep, narrow basins that formed during a period of rift

faulting. Stratigraphically above the mafic lamprophyre flows is the upper felsic flow unit (Peterson *et al.*, 1994); these felsic flows are aphanitic and free of xenoliths, and characteristics of both subaqueous and subaerial eruption are observed in the upper felsic flow sequence (Peterson *et al.*, 1994).

The term lamprophyre is used above strictly in a textural sense, implying no compositional or genetic significance. Compositionally, the CIF lamprophyres are transitional to lamproites, although mineral assemblages are typical of minettes (Peterson, 1992). Because of the discrepancy between compositional and mineralogical classification for the CIF, a unique identification in terms of the IUGS nomenclature has not proved possible (Peterson *et al.*, 1994).

The CIF is cut by a younger suite of lamprophyric, feldspar porphyritic and syenitic intrusions (Blake 1980; Gall *et al.*, 1992). A U-Pb zircon age of  $1850 \pm 30/-10$  Ma was obtained for a quartz syenite intrusion at Amer Lake, Nunavut, that may be comagmatic with the CIF (Tella *et al.*, 1985).

The Kunwak Formation, the youngest formation in the Baker Lake Group, conformably overlies the CIF. This formation is approximately 2000 m thick, and ranges in composition from coarse redbeds of no distinct vertical stratigraphy at Prince Mary Lake, to poorly bedded conglomerates and debris flows at Dubawnt Lake, possibly originating as alluvial fan deposits (Gall *et al.*, 1992; Peterson *et al.*, 1989, 1994).

### ***Wharton Group***

The Wharton Group is separated from the Baker Lake Group by an angular unconformity. The Wharton Group consists of a sequence of volcanic flows, sedimentary rocks, and granitic and granodioritic anorogenic intrusions (Gall *et al.*, 1992). The volcanic and sedimentary rocks belong to the Pitz Formation whereas the granitic and granodioritic intrusions comprise the Nueltin Intrusive Suite (Gall *et al.*, 1992).

Most of the literature on the petrology of the Pitz Formation was accumulated during the late 1970s and early 1980s as uranium exploration peaked in the Keewatin. Donaldson (1965), Blake (1980), LeCheminant *et al.* (1979, 1980, 1981, and 1984), and Peterson *et al.* (1989) conducted petrographic work on the Pitz Formation. The lavas of this unit are composed of potassic silica-rich rhyolite, and subordinate rhyodacite to dacite flows with minor intercalated sediments (LeCheminant *et al.*, 1981; Biczok, 1996). The Pitz volcanic rocks are pink-red to purple in colouration, and typically contain 5 to 35% potassium feldspar phenocrysts that reach up to 2 cm in length, subordinate quartz 'eyes' that are up to 3 mm in diameter, as well as minor plagioclase and altered mafic phenocrysts (LeCheminant *et al.*, 1981; Biczok, 1996). Gall *et al.* (1992) estimated a thickness of around 200 m for the Pitz Formation. LeCheminant *et al.* (1987b) conducted U-Pb zircon analysis on the Pitz Formation flows south of the Wager Bay Shear Zone, and constrained their age to between 1.75 and 1.78 Ga.

The Pitz Formation was targeted for uranium exploration because the rhyolite flows are fluorine-rich, topaz bearing, and enriched in lithophile elements (LeCheminant



*et al.*, 1981). Compositionally the Pitz Formation rhyolite flows share similarities to the Topaz rhyolite flows of the western United States (Christiansen *et al.*, 1986).

The Nueltin Intrusive Suite is composed of porphyritic granites that commonly have rapakivi textures (Peterson and van Breemen, 1999). Radiometric age dates obtained for the rapakivi granitic plutons range from 1751 to 1756 Ma (Peterson and van Breemen, 1999). LeCheminant *et al.* (1979) examined the petrology of the anorogenic Pamiutuq granites and concluded that the phenocryst assemblage is identical to that of the Pitz Formation volcanic rocks in the Pamiutuq Lake area. Based on the radiogenic age results and the phenocryst assemblages, the Nueltin Intrusive Suite is proposed to be the intrusive equivalent of the Pitz Formation (Gall *et al.*, 1992; Peterson and van Breemen, 1999).

### ***Barrenslund Group***

The unmetamorphosed succession overlying the Wharton Group was termed the Barrenslund Formation by Gall *et al.* (1992). The Barrenslund Formation does not outcrop near Mallery Lake, and so it is only discussed briefly here. This group encompasses three formations: the basal siliciclastic Thelon Formation (1920 m thick); the middle volcanic Kuungmi Formation (10 m thick); and the overlying 40 m thick dolomitic succession of the Lookout Point Formation (Gall *et al.*, 1992). Previous work has been conducted on the sequence by the following authors: Donaldson (1965, 1969), Blake (1980), LeCheminant *et al.* (1979, 1981, 1984) and Peterson *et al.* (1989).

## **CHAPTER 3**

### **PETROLOGY, ALTERATION, AND BASE AND PRECIOUS METALS ASSOCIATED WITH THE PITZ FORMATION RYOLITE FLOWS**

#### **Exploration in the Mallery Area since 1995**

The Mallery Lake Project is owned by Phelps Dodge Corporation of Canada, Limited. The project was initiated as a gold reconnaissance program in the Baker Lake Basin in 1995 (Figure 2.1). Twenty-three quartz stockwork zones have been located in the Mallery Lake permit area (Figure 3.1, 3.2). The Chalcedonic Stockwork zone contains several auriferous quartz veins which assay ~ 1 g/t gold (Figure 3.1, 3.3). A resource estimate has not been released by Phelps Dodge to date. The Chalcedonic Stockwork zone was gridded in 1996, followed by detailed geological mapping and sampling, IP, MAG, and VLF surveys.

The Chalcedonic Stockwork zone covers an approximate area of 500 m by 900 m (Figure 3.3). The veins generally strike at 057° and are sub-vertical. The stockwork is dominated by one central vein averaging 10-20 m wide, which locally bifurcates around blocks of the Pitz Formation. A 60 m wide zone of 2 - 20% veins, generally <30cm in width, flanks the dominant vein. Further sampling of quartz veins in the Chalcedonic Stockwork zone in 1997 revealed one small vein 350 m south of the main vein which assayed up to 24 g/t Au over 30 cm (17 Vein zone; Figure 3.3).

### Figure 3.1 Mallery Lake, Nunavut Regional Geology and Vein Type Classification

- Wharton Group (~1.75 Ga)
- mafic intrusions
  - Nuelin granite and syenite
  - Pitz Formation, rhyolite, dacite
- Baker Lake Group (~1.8 Ga)
- Kunwak Formation, conglomerate, sandstone, redbeds
- Christopher Island Volcanics  
ultrapotassic volcanic flows,  
minor pyroclastics
- Archean (>2.6 Ga)  
migmatitic gneiss
- large quartz stockwork  
auriferous silica stockwork  
Parts per thousand  
A, B Vein Type Classification  
★ Radiogenic isotope sample site

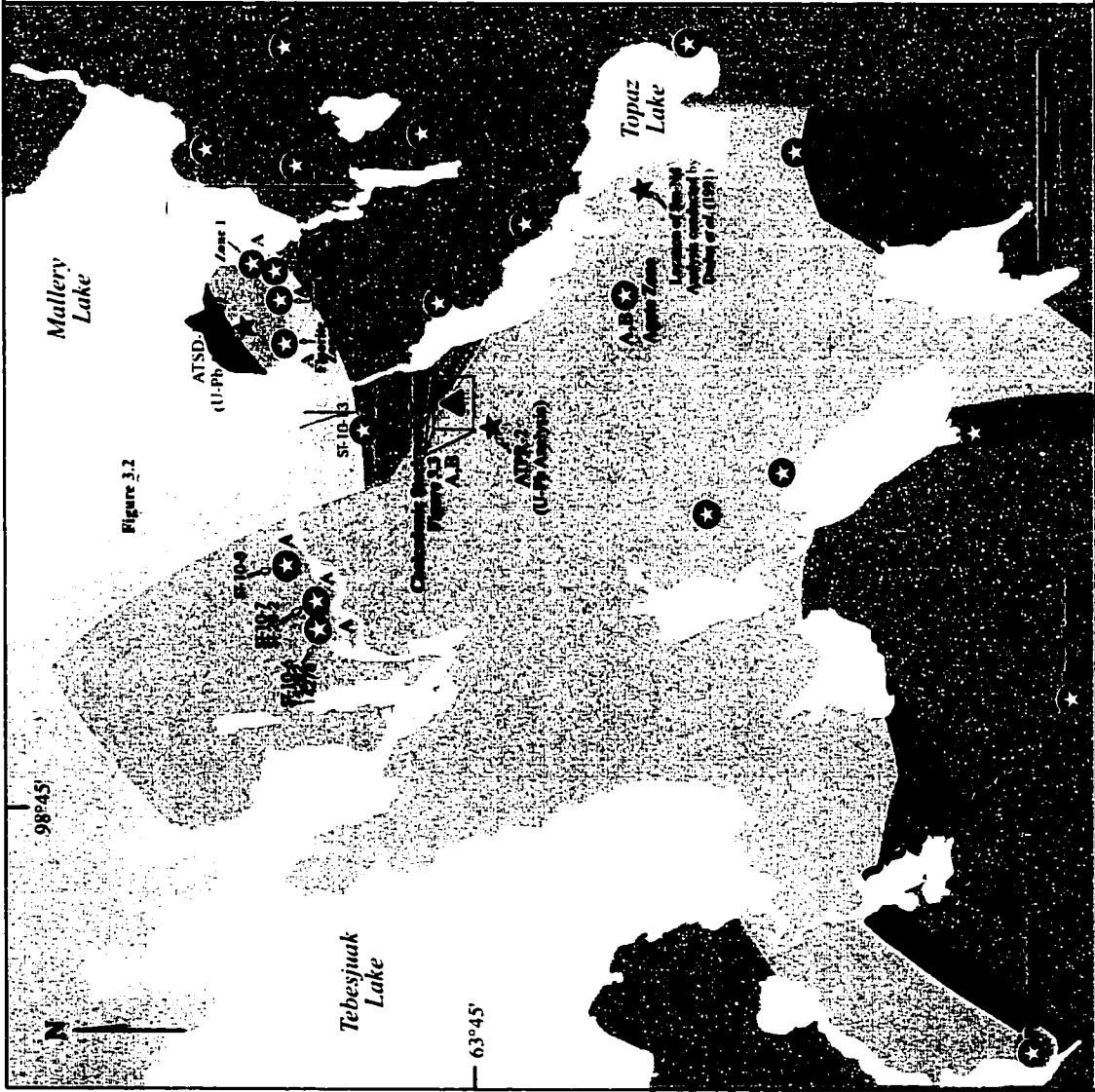
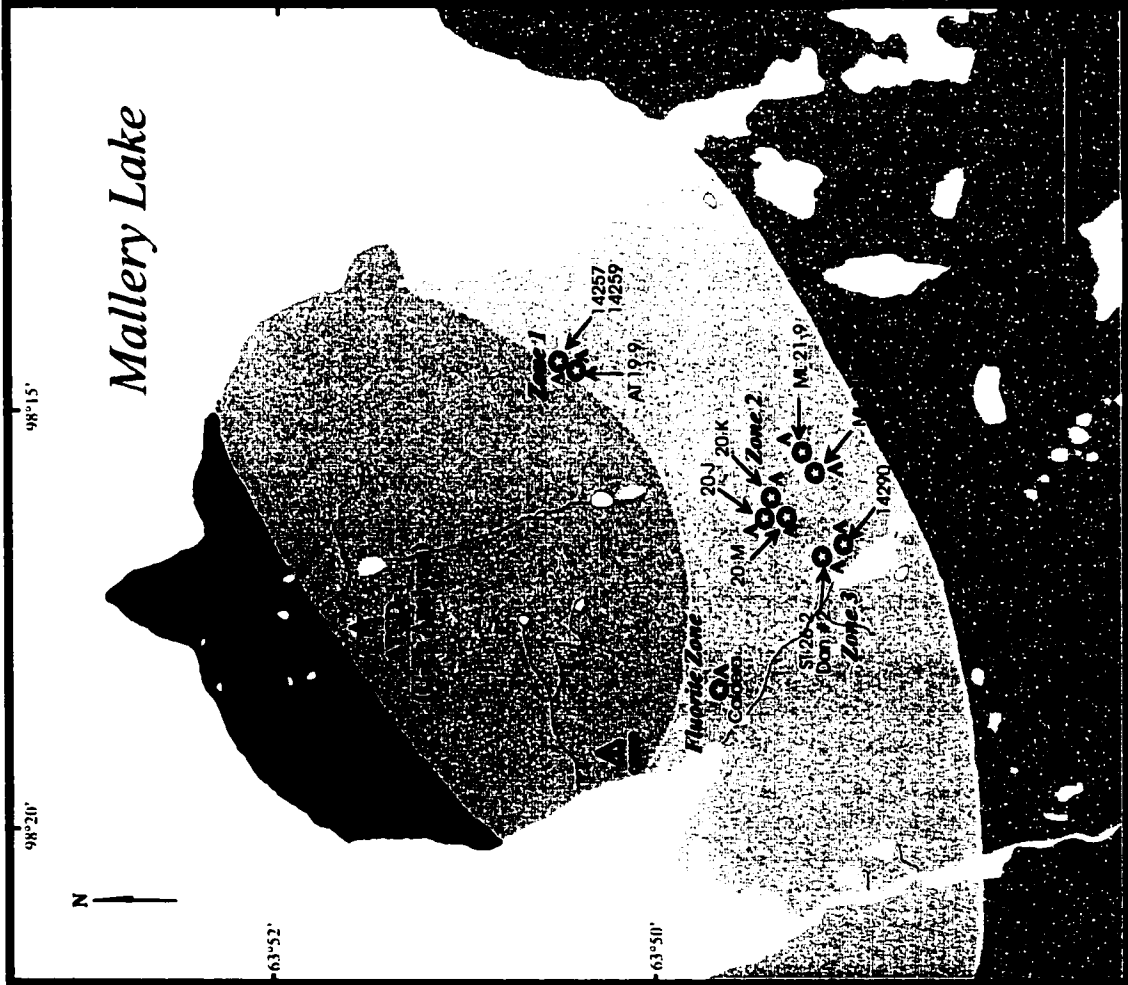
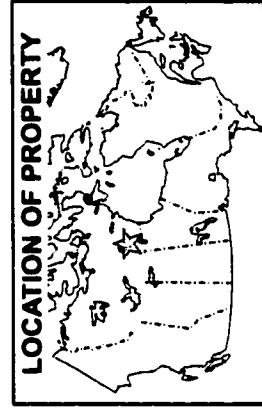


# Figure 3.2 Mallery Lake Peninsula Geology and Vein Type Classification

- Wharton Group (~1.75 Ga)
    - mafic intrusions
    - Nueltin granite and syenite
  - Baker Lake Group (~1.8 Ga)
    - Christophers Island Volcanics  
ultraprotassic volcanic flows,  
minor pyroclastics
  - Archean (>2.6 Ga)
    - migmatitic gneiss
- 
- large quartz stockwork
  - ▲ auriferous silica stockwork
  - % Parts per thousand
  - A, B Vein Type Classification
  - ★ Radiogenic isotope sample site



## **Pitz Formation**

The Pitz Formation hosts the auriferous silica stockworks in the Chaledonic Stockwork zone. The Pitz Formation flows are defined as subalkaline rhyodacite (extrusive equivalent of monzogranite) by IUGC classification using the quartz (Q), alkali feldspar (A), and plagioclase (P) ternary diagram (Figure 3.4). This conclusion was based on ICP-AES (Inductively Coupled Plasma Atomic Emission Spectroscopy) whole rock analysis of the unaltered Pitz Formation samples PR1A and PR2B (TSL Assayers Saskatoon; Table 3.1), and is in agreement with the classification by Blake (1980).

### ***Pitz Formation Petrology***

The Pitz Formation rhyodacite flows in the Mallery Lake area are porphyritic, with textures ranging from massive to flow banded, and spherulitic. Modal abundance of phenocrysts typically ranges from 20 to 25%, but an abundance of up to 45% has been documented in the Agate Zone area 12 km south of Mallery Lake (Layton-Matthews, 1997). Phenocrysts include potassium feldspar, plagioclase feldspar, quartz, and Fe-Ti oxides. The groundmass assemblage consists largely of quartz, potassium feldspar, plagioclase feldspar, and accessory minerals such as Fe-Ti oxides, monazite, and zircon.

### ***Phenocryst Assemblage***

Potassium feldspar is the dominant phenocryst phase, comprising about 80% of the phenocryst assemblage in the Pitz Formation volcanic flows. Compositionally, the dominant form of potassium feldspar is sanidine, with crystals averaging 5 mm in length

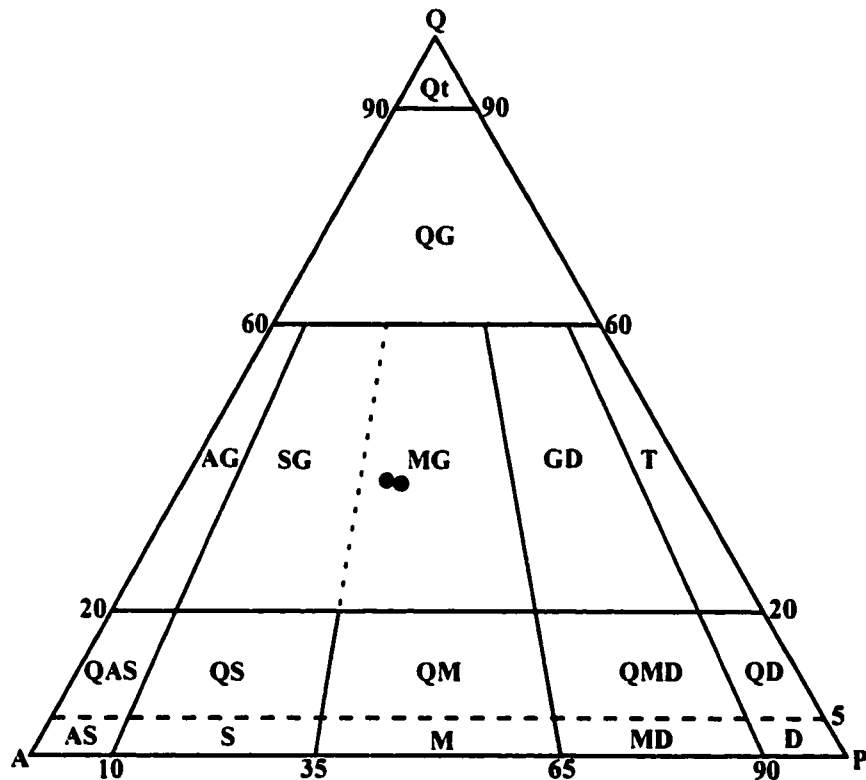


**Figure 3.4.** IUGS classification of the Pitz Formation. Two unaltered Pitz Formation samples (PR1A and PR2B) were analysed by ICP (LithiumMetaborate Fusion) whole rock analysis. IUGS classification defines the Pitz Formation flows as subalkaline rhyodacites by the above quartz (Q), alkali feldspar (A), plagioclase (P) ternary diagram. QAP ternary fields (defined by the plutonic suite names) are as follows: Qt = quartzite; QG = quartz-rich granitoids; AG = alkali-feldspar granite; SG = syenogranite; MG = monzogranite; GD = granodiorite; T = tonalite; QAS = quartz alkali-feldspar syenite; QS = quartz syenite; QM = quartz monzonite; QMD = quartz monzodiorite; QD = quartz diorite; AS = alkali-feldspar syenite; S = syenite; M = monzonite; MD = monzodiorite; D = diorite.

**Table 3.1. ICP whole rock analysis through Lithium Metaborate fusion for both altered and unaltered Pitz Formation rhyolite flows**

Location	Sample #	Alteration	SiO <sub>2</sub> (%)	Al <sub>2</sub> O <sub>3</sub> (%)	Fe <sub>2</sub> O <sub>3</sub> (%)	CaO (%)	MgO (%)	Na <sub>2</sub> O (%)	K <sub>2</sub> O (%)	TiO <sub>2</sub> (%)	MnO (%)	P <sub>2</sub> O <sub>5</sub> (%)	Ba (ppm)	Sr (ppm)	Zr (ppm)	Y (ppm)	Sc (ppm)	LOI (%)	Total
Chal #1	704068	phyllitic	76.91	11.05	1.73	0.39	0.25	0.09	7.22	0.15	0.02	0.06	320	60	300	36	3	1.84	99.51
Chal #4	704069	phyllitic	76.76	11.00	1.75	0.11	0.20	0.07	6.02	0.15	0.02	0.04	220	50	270	36	2	1.36	99.48
Chal #6	704070	phyllitic	79.69	9.80	1.41	0.22	0.14	0.11	6.98	0.13	0.01	0.06	230	60	230	28	2	1.36	99.90
Chal #8B	704071	phyllitic	83.49	7.76	1.91	0.63	0.42	0.15	2.08	0.09	0.03	0.06	100	50	180	28	4	1.58	98.21
Chal #16	704084	phyllitic	76.21	11.73	2.66	0.04	0.22	0.11	6.62	0.13	0.03	0.04	100	20	340	54	2	1.85	99.64
Chal #18	704085	phyllitic	76.54	10.94	1.45	0.04	0.16	0.08	7.66	0.13	0.01	0.06	110	40	310	44	2	1.53	98.60
Chal 1101	704072	phyllitic	79.97	9.70	1.45	0.08	0.15	0.08	6.78	0.13	0.01	0.04	210	50	220	26	2	1.14	99.49
Chal 1102	704073	phyllitic	79.37	9.89	1.35	0.34	0.16	0.09	6.06	0.09	0.02	0.04	90	30	230	40	1	1.94	98.35
Chal 1103	704074	phyllitic	83.86	8.13	1.02	0.08	0.22	0.05	4.56	0.31	0.02	0.04	300	40	470	38	4	1.25	98.53
Chal 1105	704075	phyllitic	78.18	10.42	1.15	0.06	0.15	0.13	7.00	0.15	0.01	0.04	290	50	230	30	3	1.01	98.30
Chal 1106	704076	phyllitic	78.00	11.21	1.61	0.04	0.27	0.07	6.62	0.10	0.03	0.04	190	50	260	46	2	1.73	99.71
Chal 1107	704077	phyllitic	77.65	10.67	1.21	0.03	0.10	0.09	7.24	0.09	0.02	0.02	90	50	240	36	2	1.40	98.55
Chal 1108	704078	phyllitic	73.31	12.21	1.65	0.04	0.17	0.08	8.62	0.11	0.02	0.04	190	50	260	54	3	1.62	97.66
Chal 1109	704079	phyllitic	76.31	10.99	1.49	0.23	0.12	0.08	6.92	0.09	0.02	0.04	100	40	240	46	2	1.54	97.84
Chal 1110	704080	propylitic	74.84	11.78	1.61	0.20	0.12	1.13	7.24	0.09	0.02	0.02	70	40	260	42	1	2.19	99.24
Chal 1111	704081	phyllitic	76.07	12.33	2.58	0.46	0.22	0.29	5.20	0.11	0.06	0.04	50	30	300	66	2	2.02	99.38
Chal 1112	704082	propylitic	73.33	12.86	2.31	1.30	0.39	1.89	4.90	0.13	0.05	0.06	210	40	350	54	3	2.62	99.85
Chal 1113	704083	propylitic	75.65	11.83	1.61	0.14	0.15	1.60	6.54	0.10	0.02	0.04	50	40	280	38	2	1.38	99.15
ATPR-2	PR1A	unaltered	74.57	11.94	2.72	0.67	0.17	2.55	5.59	0.13	0.04	0.01	50	20	350	55	<5	1.07	98.51
ATPR-2	PR2B	unaltered	75.04	12.13	2.09	0.51	0.14	2.44	5.89	0.13	0.03	<0.01	50	20	360	60	<5	1.10	99.55
SY-4 Std.		Canmet Value	50.06	20.63	6.20	8.05	0.53	7.07	1.64	0.29	0.10	0.14	350	1180	520	120	<5	4.56	
MRG-1 Std.		Canmet Value	40.04	8.15	17.84	14.67	13.3	0.7	0.19	3.73	0.16	0.1	50	270	100	10	50	1.56	
Canmet Value			39.32	8.5	17.85	14.77	13.49	0.71	0.18	3.69	0.17	0.13	50	260	105	16	48	1.56	

All samples were analysed through ICP-AES (Inductively Coupled Plasma Atomic Emission Spectroscopy) whole rock analysis by TSL Assayers, Saskatoon, Saskatchewan. SY-4 and MRG-1 are two standards that were run with samples PR1A and PR2B with reference to their Canmet (Canadian Certified Reference Material Standards) values. For the locations of the altered Pitz Formation rhyolite flows see Figure 3.3, and Figure 3.1 for the unaltered flows

in the Chalcedonic Stockwork zone, but up to 2 cm in the Agate Zone. Plagioclase feldspar makes up approximately 3% of the modal abundance of the Pitz Formation flows, with grains averaging 5 mm in size. Compositionally, plagioclase feldspar was determined to be 45% anorthite and 55% albite by the Michel Levy Method of plagioclase discrimination. Intergrowths of plagioclase and quartz form a distinct myrmekitic texture at some alkali and plagioclase feldspar contacts. Quartz phenocrysts comprise about 10% of the modal abundance of the flows.

### ***Accessory Mineral Assemblage***

Accessory minerals in the system are separated into two types: opaque accessory minerals and non-opaque accessory minerals. The opaque accessory minerals include the following: ilmenite and/or titanomagnetite, pyrophanite, rutile, ilmenorutile, hematite, and pyrite. Non-opaque accessory minerals include monazite and zircon. Accessory minerals were identified in pristine and altered Pitz Formation host rocks, as well as in association with silica veins.

Transmitted and reflected light microscopy, as well as semi-quantitative EDS microprobe analysis were used to determine the compositions of the opaque minerals. The oxide phases fall into four categories: (1) Fe-Ti-oxides: ilmenite ( $\text{FeTiO}_3$ ) or titanomagnetite (depending of Fe - Ti ratio), and rutile ( $\text{TiO}_2$ ); (2) solid solution reaction minerals between manganese and iron:  $(\text{Fe,Mn})\text{TiO}_3$  (solid solution between ilmenite and pyrophanite) and pyrophanite ( $\text{MnTiO}_3$ ); (3) Substitution of  $\text{Nb}^{+5}$  for  $\text{Ti}^{+4}$  in the rutile



structure causing the formation of the mineral ilmenorutile ( $\text{Ti}(\text{Nb})\text{O}_2$ ); and (4) bladed hematite that was most likely deposited by oxidized hydrothermal fluids (Plate 3.1).

Trace amounts of chalcopyrite, pyrite, galena, sphalerite, and barite were identified in the system. These sulfides were most likely precipitated from the hydrothermal fluids. The coexistence of rutile with pyrite (Plate 3.2A), and barite with pyrite (Plate 3.2B) indicate that the metal transport ligand, as well as the oxidation state of the fluid was in flux.

Non-opaque accessory minerals in the Pitz Formation rhyolite flows include zircon and monazite. The majority of the zircons associated are shattered, although some crystals with euhedral terminations do exist. The average length of the zircons is from ~ 20  $\mu\text{m}$  to 50  $\mu\text{m}$ . Typically, the zircons from the Pitz Formation flows are transparent with a slight pinkish tint. Lanthanum-rich monazite ( $(\text{Ce},\text{La})\text{PO}_4$ ), occurring as bleb to lath shaped crystals that range from 2  $\mu\text{m}$  to 10  $\mu\text{m}$  in length, may have also been precipitated from the hydrothermal fluid in the system (Plate 3.2C).

### ***Textures of the Pitz Formation rhyolite flows***

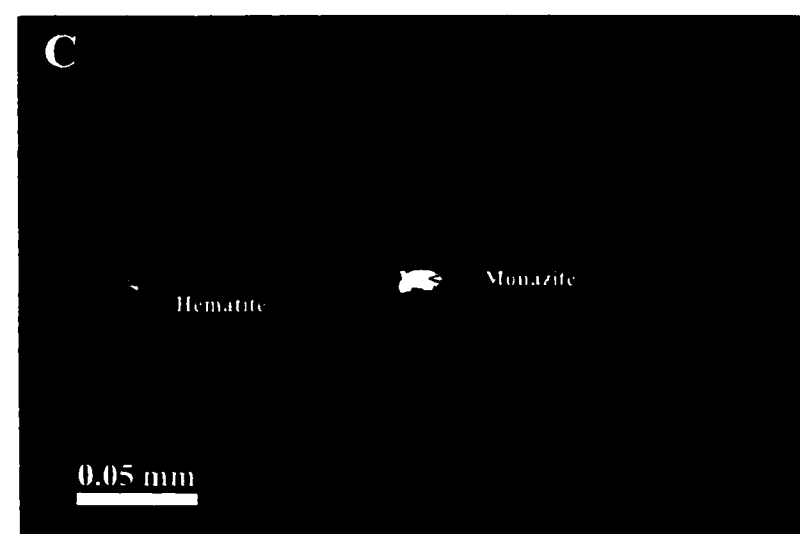
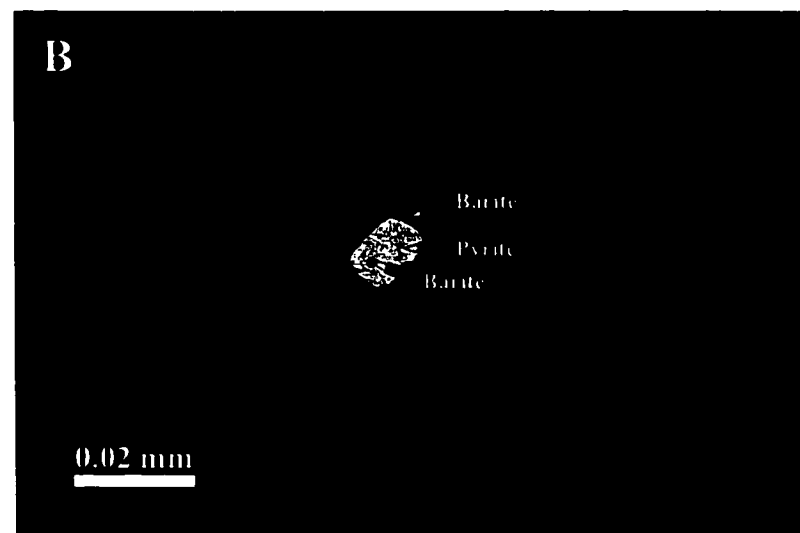
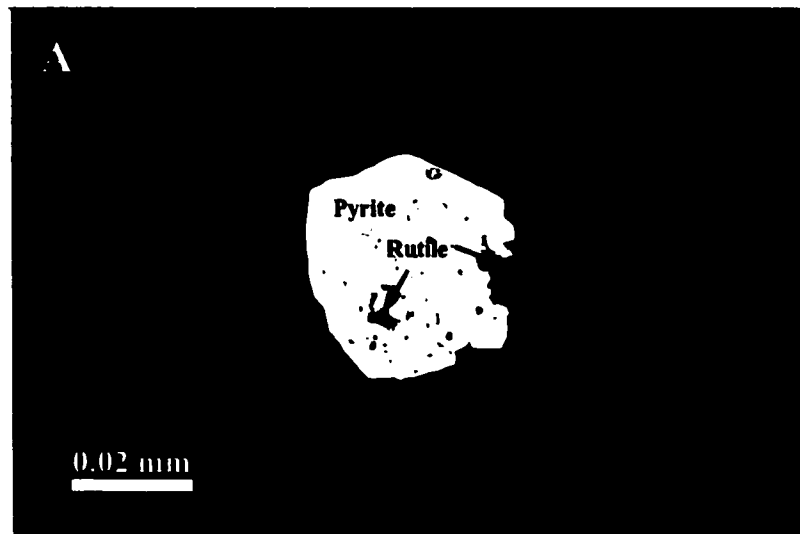
The Pitz Formation flows in the Mallery Lake area show textures produced by the devitrification of rhyolitic glasses. Devitrification involves the sub-solidus crystallization of metastable glass (Wilson, 1989). Lofgren (1970, 1971a, 1971b) studied the devitrification of rhyolitic glasses under varying conditions of temperature, pressure, time, and fluid composition. He classified devitrification of glasses into three stages to categorize the textures observed in partially or wholly devitrified rhyolitic glass: a Glassy

**Plate 3.1.** Metals associated with the later depositional event (Sample 703527). Pictures **A** (reflected light) and **B** (transmitted light) show lath hematite blades in later cross-cutting quartz-hematite silica veins. The hematite blades deposited in the quartz vein are an indication of the oxidization state of the fluids at the time of the vein formation.



**Plate 3.2.** Mineral associations in Sample 712608 (A, B, C; reflected light).

(A) Bleb of rutile ( $\text{TiO}_2$ ) cogenetically precipitated with pyrite ( $\text{FeS}_2$ ). The association of oxide with sulfides indicates that the system was undergoing a fluctuation in oxidation state at the time of precipitation. (B) Barite ( $\text{BaSO}_4$ ) associated with a pyrite ( $\text{FeS}_2$ ) grain in a quartz vein. Barite precipitated syngenetically with the pyrite as seen by the incorporation of a small barite bleb within the pyrite grain (reflected light). Iron-stained barite is later precipitated around the pyrite grain. The fluctuations between sulfide and sulfate states indicate that the fluid was undergoing rapid changes in the oxidation conditions. (C) A monazite bleb  $(\text{Ce,L a})\text{PO}_4$ , proximal to a bleb of hematite, is identified in the silicified Pitz Formation host rock adjacent to a quartz vein.



stage; a Spherulitic stage; and a Granophyric or Granitic stage. The Glassy stage contains isolated spherulites in a glassy matrix. The Spherulitic stage has a matrix of devitrified glass that is pervasively spherulitic or micropoikilitic in texture. The Granophyric or Granitic stage occurs as a late stage event, destroying all previous textures.

Experimentally, Lofgren (1971b) constrained the conditions of formation for the three textural stages. A rock containing the Glassy stage texture represents a water undersaturated magma that underwent rapid cooling, and therefore little nucleation. The Spherulite stage characteristically forms from magma with higher water contents and temperatures than that of the Glassy stage. The Granitic or Granophyric stage forms as a result of maintaining magma at a constant temperature and pressure for an extended period of time.

### ***Observations***

The Pitz Formation contains textures characteristic of both the Spherulitic stage and the Granitic or Granophyric stage. Plates 3.3 and 3.4 are microphotographs of textures taken from the Pitz Formation in the area of the Chalcedonic Stockwork Zone. The textures include micropoikilitic and axiolitic spherulitic growth patterns as well as granophyric quartz-feldspar intergrowths.

### ***Discussion***

The incorporation of spherulitic needles within the later stage micropoikilitic Plate

**Plate 3.3.** Spherulitic growth textures in the Pitz Formation flows (samples Chal 1203 and 1202; plane-light). (A) This circular spherical mass is composed of acicular feldspar crystals that radiate from a central nucleus. (B) A wheat sheaf spherulitic growth possibly caused by growth along a flow-banding layer. (C) Axiolite growth begins as a spherulite that nucleates on a tightly packed band of globulites. Nucleation occurs rapidly on the tightly packed band, resulting in the growth of spherulitic sheaves perpendicular to the globulitic layers.

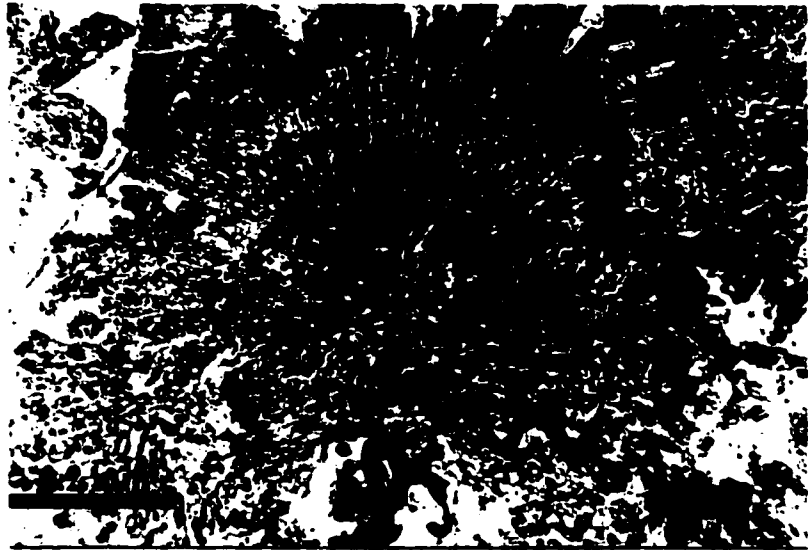




**Plate 3.4.** Spherulitic growth textures in the Pitz Formation rhyolite flows (samples Chal 1203 and 1202). Pictures **A** (crossed-polars), **B** (plane-light), and **C** (crossed-polars) depict skeletal growth textures formed by granophyric quartz-feldspar intergrowths. The process by which this skeletal growth textures forms is under considerable debate (see discussion in text).



quartz, as well as the granophyric quartz-feldspar intergrowths, indicates that supercooling may have occurred in the system after the formation of spherulites. Currently, two contrasting theories exist as to the conditions that cause the formation of granophyric quartz-feldspar (spherulitic) intergrowths in micropoikilitic quartz. The classical theory is that this texture represents embayment of quartz, and subsequent spherulitic growth, as a function of late stage reabsorption. The second theory, proposed by Candela (1997), postulates that undercooling of the magma is the driving force behind silica precipitation and growth. As the magma undercools, quartz solubility decreases rapidly, resulting in the rapid precipitation of silica. The rapid deposition of quartz, precipitated under disequilibrium conditions, may form skeletal growth textures (Plate 3.4).

In addition, the high density of spherulites in the system may indicate that the original magma contained a relatively high water content and/or higher temperatures and a relatively slow cooling rate, while the presence of axiolitic textures indicate that the system was subjected to micro-flow banding.

The above textural observations are in agreement with the conclusions of Blake (1980) on the Pitz Formation. He proposed that the presence of spherulites in the Pitz Formation be due to initial hydration of the system that resulted from trapping water in the lava flow during subaqueous extrusion. As the magma contacted the trapped waters, a high-pressure steam was formed and subsequently incorporated into the lava. The result was rapid cooling of the magma and the formation of a hydrated glass. Later devitrification of the glass resulted in the formation of spherulites.

## **Alteration of the Chalcedonic Stockwork Zone**

Micropetrography and XRD analysis were used to characterize alteration mineralogy in the Chalcedonic Stockwork zone (Table 3.2), while chemical changes were assessed from whole rock geochemical analysis (Table 3.1). Alteration varies across the Chalcedonic Stockwork zone (Figure 3.3). The alteration assemblages are as follows: a central zone of silicification with trace argillic alteration proximal to the silicification, surrounded by phyllic alteration characterized by sericite (Plate 3.5) and adularia, and a distal zone of propylitic alteration. The central silicification stage is composed of auriferous chalcedonically banded silica with intercalated bands of illite (Layton-Matthews, 1997). Further petrographic analysis as well as hydrofluoric acid etching and cobaltnitrite staining, indicated that banded adularia was also present between the chalcedonic silica bands. As well, some of the later stage silicification contains sporadic pockets of kaolinite (Table 3.2).

It was determined through petrographic analysis that the host rocks adjacent to the silica stockworks vary in the extent of phyllic alteration. This observation is further substantiated litho-geochemically, as samples are enriched in  $\text{SiO}_2$  and  $\text{K}_2\text{O}$  while depleted in  $\text{CaO}$  and  $\text{Na}_2\text{O}$  relative to unaltered Pitz Formation samples (PR1A, PR2B; Table 3.1). As well, there appears to be an increase in the elements Ba and Sr in the altered samples relative to the unaltered Pitz Formation. The presence of barite in some quartz veins (Plate 3.2B) indicates that hydrothermal fluids may have brought in these alkali earth elements.

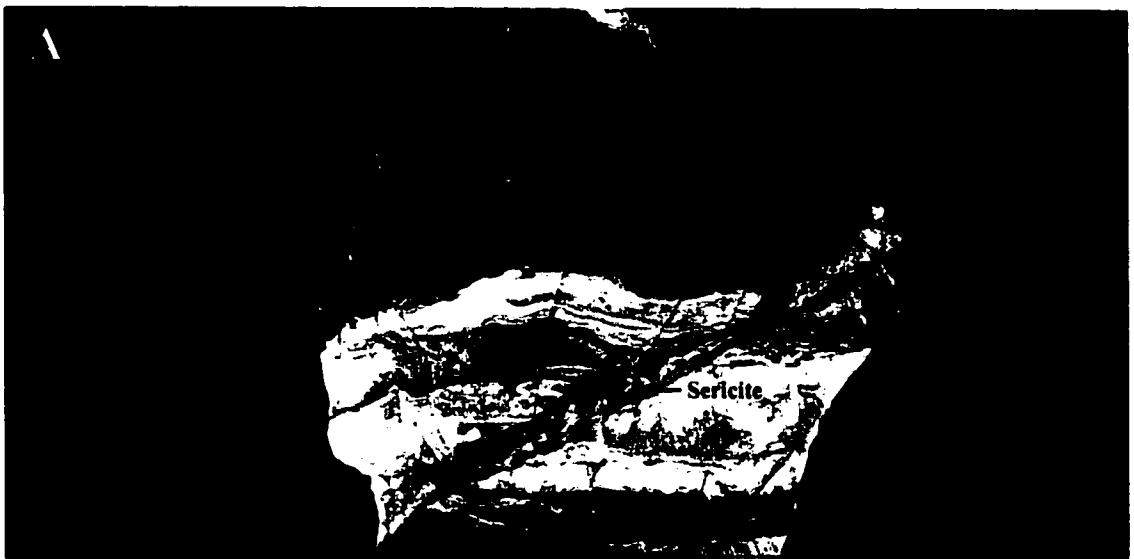
Although XRD does not distinguish between primary and hydrothermal potassium

**Table 3.2. XRD analytical results of Chalcedonic Stockwork Zone samples**

Sample Number	Albite	Microcline	Orthoclase	Sandine	Hematite	Illite	Muscovite	Quartz	Kaolinite	Pyrite	Chlorite
703524a		*					*	*			
703530a			*				*	*	*		
703535a		*			*		*	*			
17 VEINa		*				*	*	*			
Chal <sup>#</sup> 1a		*				*	*	*		*	
Chal <sup>#</sup> 3a			*				*	*			
Chal <sup>#</sup> 4a		*					*	*		*	
Chal <sup>#</sup> 5a			*			*	*	*		*	
Chal <sup>#</sup> 7b		*					*	*			
Chal <sup>#</sup> 8b						*	*	*		*	
Chal <sup>#</sup> 11a		*	*				*	*		*	
Chal <sup>#</sup> 12a					*	*	*	*			
Chal <sup>#</sup> 13a		*					*	*			
Chal <sup>#</sup> 14a		*					*	*			
Chal <sup>#</sup> 15a		*	*				*	*			
Chal <sup>#</sup> 16a		*					*	*			
Chal <sup>#</sup> 1101a		*					*	*			
Chal <sup>#</sup> 1102a		*		*		*	*	*			
Chal <sup>#</sup> 1103a				*			*	*			
Chal <sup>#</sup> 1104a		*					*	*		*	
Chal <sup>#</sup> 1105a		*					*	*			
703515a		*					*	*			
Chal <sup>#</sup> 1106a		*					*	*			
Chal <sup>#</sup> 1107a			*				*	*			
Chal <sup>#</sup> 1108a		*					*	*			
Chal <sup>#</sup> 1109a		*					*	*			
Chal <sup>#</sup> 1110a		*				*	*	*		*	
703518a						*	*	*			
Chal <sup>#</sup> 1111a		*				*	*	*		*	
Chal <sup>#</sup> 1112a	*	*					*	*		*	
Chal <sup>#</sup> 1113a	*		*			*	*	*			
Chal <sup>#</sup> 1114a	*	*				*	*	*			
Chal <sup>#</sup> 1202a		*					*	*			
Chal <sup>#</sup> 1203a		*					*	*			
Chal <sup>#</sup> 1205a	*	*					*	*		*	
Chal <sup>#</sup> 1206a		*					*	*			
Chal <sup>#</sup> 1208a	*	*					*	*		*	
Chal <sup>#</sup> 1209a		*					*	*		*	*
Chal <sup>#</sup> 1210a		*					*	*			
Chal <sup>#</sup> 1211a	*	*					*	*		*	
Chal <sup>#</sup> 1212a	*	*					*	*		*	
Chal <sup>#</sup> 1213a		*					*	*		*	
Chal <sup>#</sup> 1214a		*					*	*			
Chal <sup>#</sup> 1215a		*				*	*	*			
Chal <sup>#</sup> 1217a		*					*	*		*	

XRD analysis of altered Pitz Formation rhyolite flows in the vicinity of the Chalcedonic Stockwork Zone.  
 Suffix (a) defines analysis of whole rock, while suffix (b) indicates analysis of specific alteration patch in rock.

**Plate 3.5.** Late stage quartz vein cross-cutting previous chalcedonically banded vein (Sample Chal #7). Late in the paragenetic sequence of the cross-cutting quartz stringer is the precipitation of yellow-green sericite (A). Microphotography of this section shows the infill of sericite between earlier euhedral quartz (B; crossed-polars).



*Good Measure*

from the

**National Bure**



feldspar, thin section petrographic analysis indicates that some remnant primary potassium feldspar does exist in various stages of alteration to sericite. As conditions changed in the system (i.e. pH and temperature changes), hydrothermal potassium feldspar (adularia) and sericite were alternately stabilized. White (1995) proposed that as hydrothermal systems mature, there are fluctuations in pH and temperature, and possibly the level of the water table. This theory explains the alteration of adularia to sericite and subsequent replacement of sericite by silica in the Chalcedonic Stockwork zone. Further discussion of this alteration and replacement process is included in Chapter 4. Some of the phyllically altered Pitz Formation rhyolite samples have a dusting of native sulfur along fracture surfaces.

Further from the central area of silicification the alteration grades into propylitic. The propylitic alteration was determined optically by the presence of calcite and trace epidote and the preservation of plagioclase feldspar. This transition to propylitic alteration is further recorded lithogeochemically by the enrichment of CaO and the retention of Na<sub>2</sub>O relative to the unaltered Pitz Formation (Table 3.1). Surficial mapping of the Chalcedonic Stockwork zone was limited by the extent of tundra cover, therefore only an inferred contact between the phyllic and propylitic alteration is indicated in Figure 3.3. The patch of phyllic alteration at sample site Chal 1111 (704083) is due to increased fluid flow and subsequent silicification distal to the main silica stockwork, possibly a result of fluid induced host rock faulting at shallow depths.



## **Petrographic Evidence of Precious Metal Association in Hydrothermal Veins**

### ***Observations***

Evidence for precious metal deposition in the silica veins was observed in two samples from the Chalcedonic Stockwork zone (703530 and 703527) by reflected light microscopy and back-scattered electron EDS microprobe analysis. Texturally, ore metal deposition was associated with two events: (1) an early stage of precious metal deposition that cogenetically precipitated with quartz (703527); and (2) a later stage quartz-hematite vein event that brought in precious metals (703530).

Although assay results indicated abundant precious metals in the system (typically 1-5 g/t Au), actual identification of precious metals proved difficult due to the small grain size (frequently sub-micron scale). Native silver was identified in the early stages of quartz deposition in sample 703527 (Table 3.3).

Later precious metal-bearing quartz-hematite veins are observed in sample 703530. High electrum and trace Ag sulfide (argentite-acanthite?) concentrations were associated with the quartz-hematite veins (Plate 3.6). The Au:Ag ratios for the electrum typically range from 2:1 to 1:1, having compositional variation within a single Au:Ag grain.

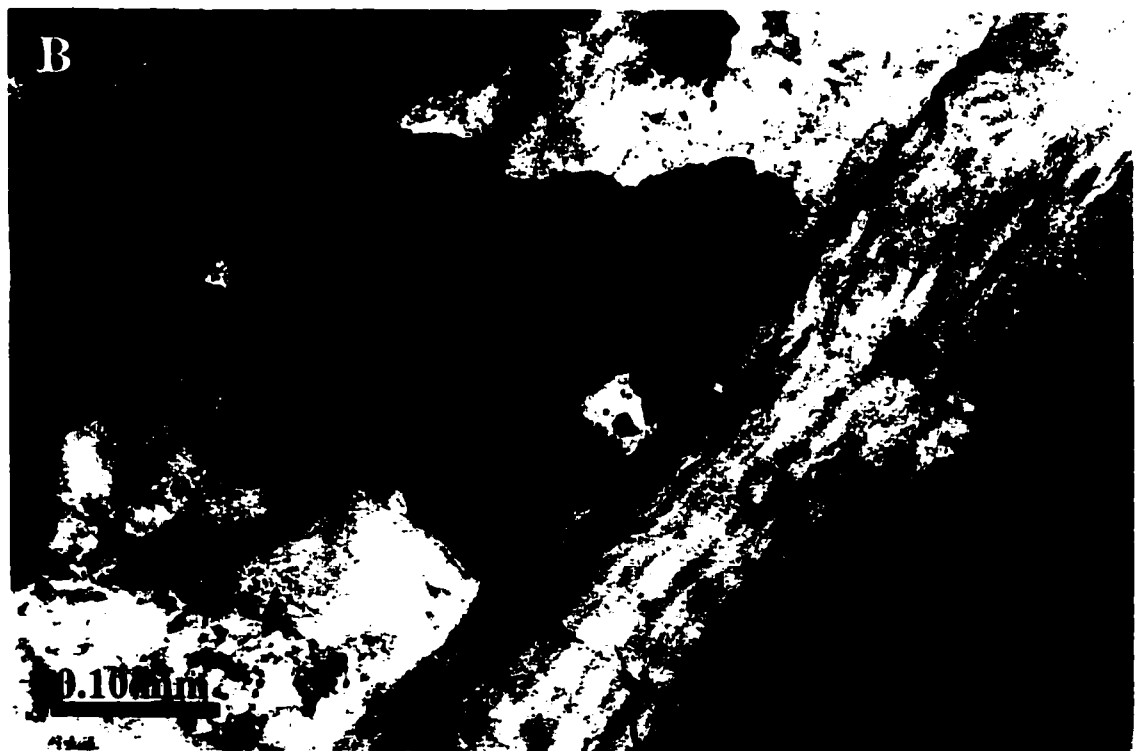
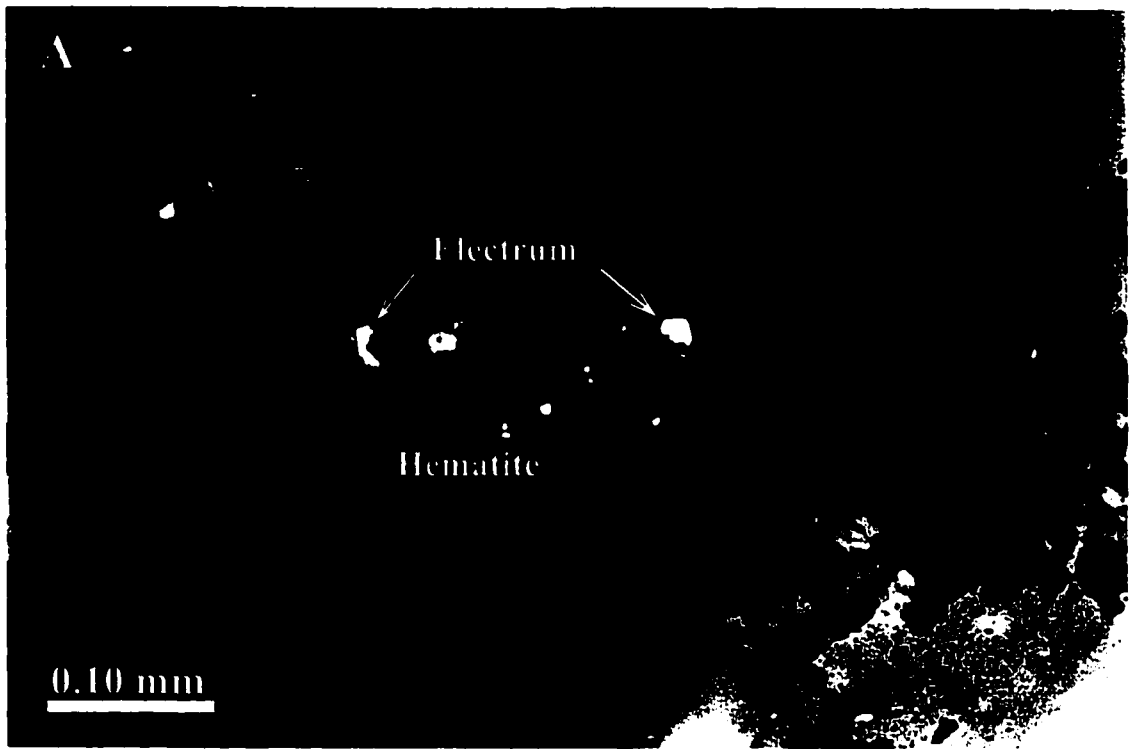
In summary, there are two distinct events of base and precious metal deposition associated with the quartz veins in samples 703527 and 703530. The early event of metal

**Table 3.3. Au, Ag, and Cu abundances obtained from EDS microprobe analysis of precious metal grains that were analysed from veins in the Chalcidonic Stockwork Zone**

Sample #	Au (wt %)	Ag (wt %)	Cu (wt %)	total	Relative Au wt %	Relative Ag wt %	Relative Cu wt %	
703530	67.9	29.6	0.5	98.1	69.3	30.2	0.5	
	72.4	26.1	0.4	98.9	73.2	26.4	0.4	
	57.7	34.4	0.0	92.1	62.6	37.4	0.0	
	63.8	31.6	0.0	95.4	66.9	33.1	0.0	
	54.6	45.1	0.2	99.8	54.7	45.2	0.2	
	79.9	19.5	0.1	99.4	80.3	19.6	0.1	
	66.0	32.9	1.1	100.0	66.0	32.9	1.1	
	68.4	30.3	0.6	99.3	68.9	30.5	0.6	
	71	28	0	99	71.7	28.3	0.0	
	62	36	0	98	63.3	36.7	0.0	
	80.0	19.5	0.5	100	80.0	19.5	0.5	
	55	45	0	100	55.0	45.0	0.0	
	57.0	41.5	0.0	98.5	57.9	42.1	0.0	
	70	30	0	100	70.0	30.0	0.0	
	66	33	0	99	66.7	33.3	0.0	
	63	34	0	97	64.9	35.1	0.0	
	85	15	0	100	85.0	15.0	0.0	
	703527	0.0	0.0	29.8	29.8	0.0	0.0	100.0
		0.0	75.6	1.5	77.1	0.0	98.0	2.0
		0.0	65.7	0.3	66.0	0.0	99.6	0.4
0.0		0.0	41.3	41.3	0.0	0.0	100.0	
0.0		95.4	2.3	97.7	0.0	97.6	2.4	
0.0		0.0	31.4	31.4	0.0	0.0	100.0	
0.0		0.3	36.2	36.5	0.0	0.7	99.3	
0.0		93.3	0.0	93.3	0.0	100.0	0.0	
0.8		94.1	0.0	94.9	0.8	99.2	0.0	
0.0		82.2	2.2	84.4	0.0	97.4	2.6	
0.0		97.7	1.9	99.6	0.0	98.1	1.9	

(All results attained via semi-quantitative back-scatter electron EDS microprobe analysis)

**Plate 3.6.** Precious metal association to the later depositional event (Sample 703530). Blebs of electrum are intimately associated with a later cross-cutting quartz-hematite vein (A: reflected light; B: plane light). Typically the Au:Ag ratios are around 2:1 for this later stage veining event (Table 3.3).



deposition appears to have occurred at the time of quartz precipitation, and therefore is cogenetic with primary vein formation. Veins deposited during this event contain native silver, but low amounts of gold. The next event of precious metal deposition is associated with paragenetically later quartz-hematite veins that brought in electrum and minor Ag-sulfides.

## **CHAPTER 4**

### **TEXTURES OF BARREN AND PRECIOUS METAL BEARING VEINS**





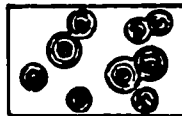


#### **Introduction**

Epithermal silica textures are grouped into two major categories: primary growth textures (Type A), and secondary textures (Type B) by Dowling and Morrison (1989), Bobis (1994), and Dong *et al.* (1995). Secondary textures are further divided into replacement and recrystallization textures. Primary growth textures form by silica being precipitated into open spaces, whereas recrystallization textures are produced by a transition of silica from a metastable phase such as chalcedony, opal, or cristobalite to quartz, and replacement textures result from partial or total replacement of earlier mineral phases such as carbonates or adularia by quartz (Bobis *et al.*, 1995). Silica vein textures, studied at both hand specimen and microscopic scale, aid in understanding the physical and chemical processes that affect silica and calcite solubilities in hydrothermal fluids (Bobis, 1994).










#### **Observations**

Textural studies of epithermal veins in the Mallery Lake area distinguish barren from precious metal-bearing veins. Veins are grouped into primary growth, replacement, and recrystallization textures, but barren and mineralized veins exhibit distinctive textures: barren veins display primary growth textures (Figure 4.1a), whereas recrystallization and replacement textures characterize mineralized veins (Figure 4.1b).

There are three general vein types that display primary growth textures: (1)

Texture Type	Sketch of Texture	Grain Size	Grain Form	Internal Feature of Individual Crystal	Morphology of Crystal Aggregate	References
<b>Primary Growth Textures</b>						
Massive		variable	anhedral	not applicable	homogenous	Smirnov (1962) Bates & Jackson (1987)
Crustiform		variable	variable	not applicable	successive banding	Adams (1920) Shaub (1934) Lindgren (1933) Buchanan (1981)
Cockade		variable	variable	not applicable	concentric banding	Adams (1920) Spurr (1926)
Colloform		fine	fibrous anhedral	not applicable	semi-spherical, reniform, mammillary	Rogers (1917) Adams (1920)
Moss		fine	variable	not applicable	spherical	Adams (1920)
Comb		variable	prismatic	not applicable	parallel-orientated	Adams (1920) Schieferdecker (1959) Boyle (1979)
Zonal		variable	prismatic	zonal	not applicable	Smirnov (1962)

**Figure 4.1a.** Classification of primary (Type A) silica textures (Dong *et al.*, 1995)

Texture Type	Sketch of Texture	Grain Size	Grain Form of Individual Crystal	Internal Feature	Crystal Morphology of Crystal Aggregate	References
<b>Recrystallization Textures</b>						
Mosaic		fine	anhedral	not applicable	interpenetrating	Lovering (1972) Saunders (1990)
Feathery		variable	prismatic	plumose	not applicable	Adams (1920) Sander and Black (1988)
Flamboyant		variable	round	radial	not applicable	Adams (1920) Sander and Black (1988)
Ghost-sphere		fine	anhedral	spherical	not applicable	Adams (1920)
<b>Replacement Textures</b>						
Pseudo-bladed Lattice-bladed		fine	anhedral to prismatic	not applicable	intersecting bladed	Lindgren (1899) Schrader (1912) Morgan (1925)
Ghost-bladed		fine	anhedral	not applicable	intersecting bladed	
Parallel-bladed		fine	anhedral to rectangular	not applicable	parallel bladed	Adams (1920)
Pseudo-acicular		fine	anhedral to rectangular	not applicable	acicular	Lindgren and Bancroft (1914) Adams (1920) Schrader (1923)
Saccharoidal		fine	anhedral to prismatic	not applicable	interlocking	Lindgren (1901) Adams (1920) Lovering (1972)

**Figure 4.1b.** Classification of secondary (Type B) silica textures (Dong *et al.*, 1995)



euhedral vuggy quartz commonly followed by fluorite, carbonate, specularite, adularia, or sericite precipitation; (2) brecciated host rock fragments cemented by silica; (3) euhedral micro-quartz bands intercalated with bands of purple and/or white fluorite.

Precious metal bearing veins are associated with replacement and recrystallization textures. Recrystallization textures include microcrystalline mosaic, flamboyant, feathery, ghost-sphere, and coarse crystalline quartz textures that formed from a chalcedonic or amorphous silica precursor (Figure 4.1b; Dong *et al.*, 1995). Late stage cross-cutting hematite stained quartz veins are evident in some samples. Replacement textures include quartz replacement of carbonate lattice blades and adularia crystals, and the formation of ghost-bladed textures (Figure 4.1b; Dong *et al.*, 1995).

## **Quartz Texture Interpretation**

### **Primary Textures (Type A)**

Barren veins are typically characterized by brecciated wall rock fragments that are infilled by quartz and intercalated with fluorite and micro- and macro-crystalline quartz. It is common for a stage of fluorite, adularia, or calcite precipitation to occur after the event of silica deposition (Plates 4.1, 4.2, 4.3, and 4.4).

Quartz is the stable silica polymorph under the typical low pressure / temperature conditions of epithermal systems (Fournier, 1985). Precipitation of quartz directly from hydrothermal fluids, in the case of zoned, faceted quartz crystals, occurs under low degrees of silica supersaturation, and slow rates of crystal growth. Growth of faceted quartz crystals into open vugs is an indication of crystal formation in shallow environments under low confining pressures (Gilbert and Park, 1986).

**Plate 4.1.** Primary textures (Type A). (A) Vuggy quartz with euhedral terminations followed by precipitation of late stage purple fluorite (Fluorite Zone). (B) Growth of vuggy quartz after hydrothermal fracturing and silicification of Pitz Formation host rock. Quartz crystals show euhedral, zoned terminations (ST 12-6).

A



9 10 11 12 13 14 15 16 17 18 19 20 21 :

B



**Plate 4.2.** Primary textures (Type A). (A) Euhedral milky quartz followed by a late stage of adularia precipitation (ST 6-3). (B) This close up of a drusy cavity shows the incorporation of adularia (or muscovite?) in the core of a clear euhedral quartz crystal terminations (ST 7-4).

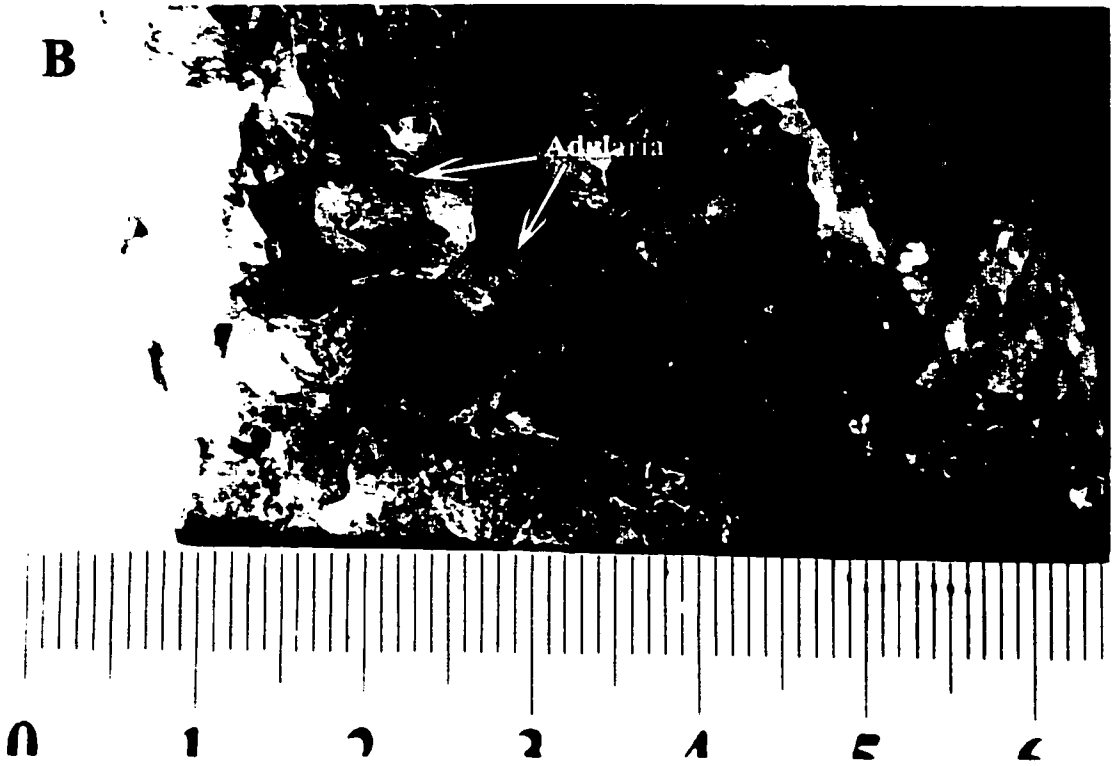
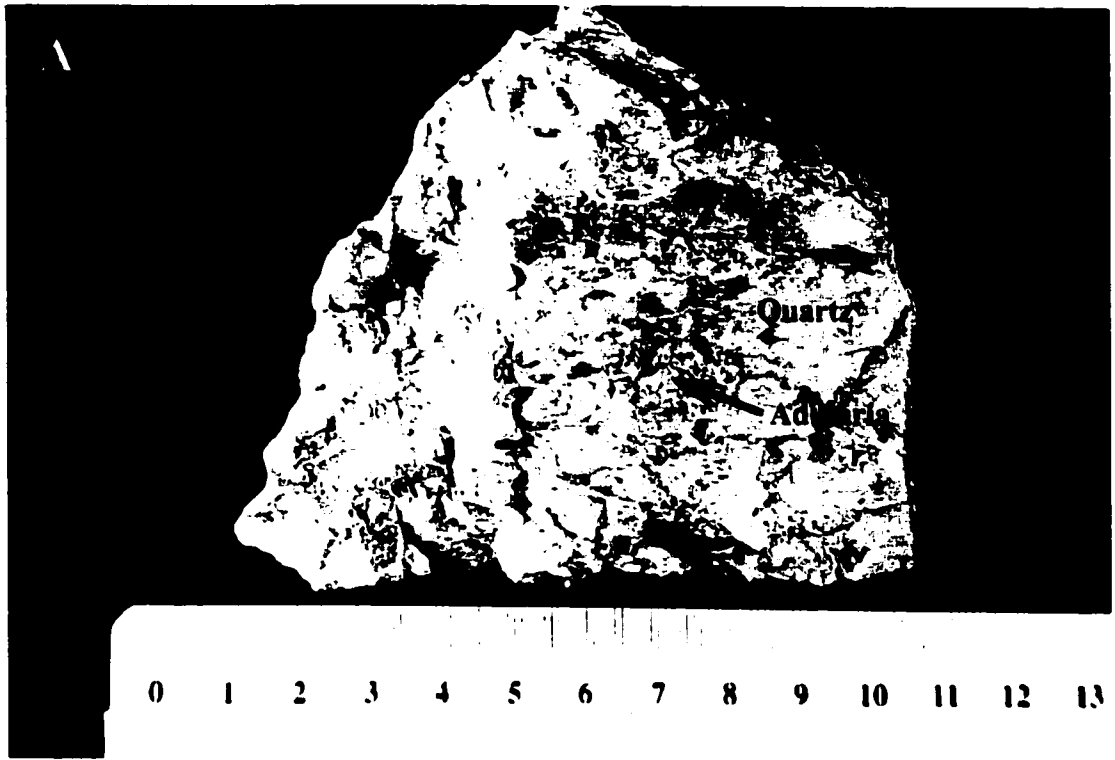


**Plate 4.3. Primary textures (Type A). Quartz followed by a later stage carbonate deposition (Sample 14259). (A) This sample shows bladed calcite in association with quartz. Pictures (B; plane light) and (C; crossed-polars) depict late stage euhedral silica growth around carbonate blades. Note that some of the carbonate blades are completely trapped by the silica growth. In plane light, carbonate blades cut obvious primary euhedral silica growth bands. Typically, silica would replace carbonate blades due to the prograde solubility of silica and the retrograde solubility of carbonate. Replacement of the calcite blades has not occurred in this sample, indicating that fluid flow may have waned soon after the calcite precipitation (possibly after boiling).**

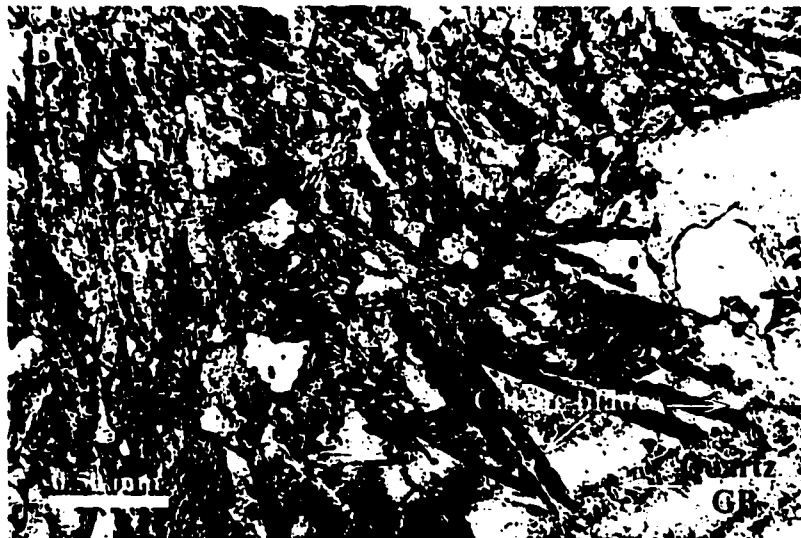
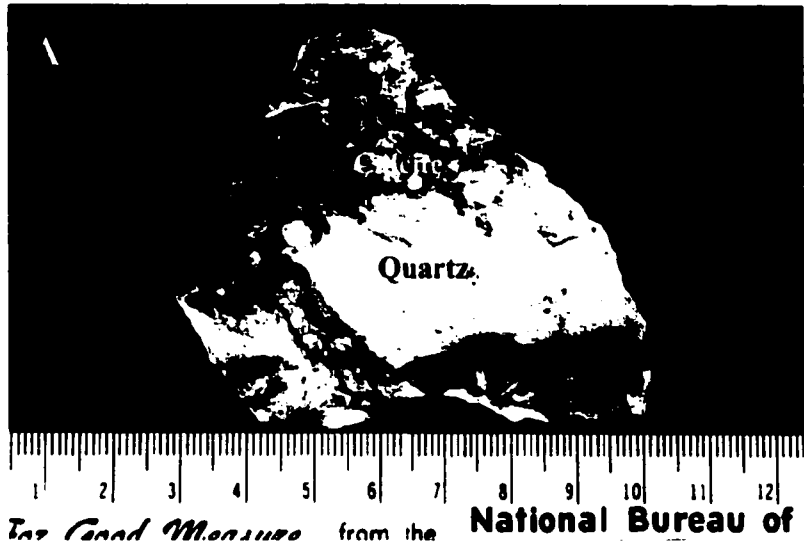
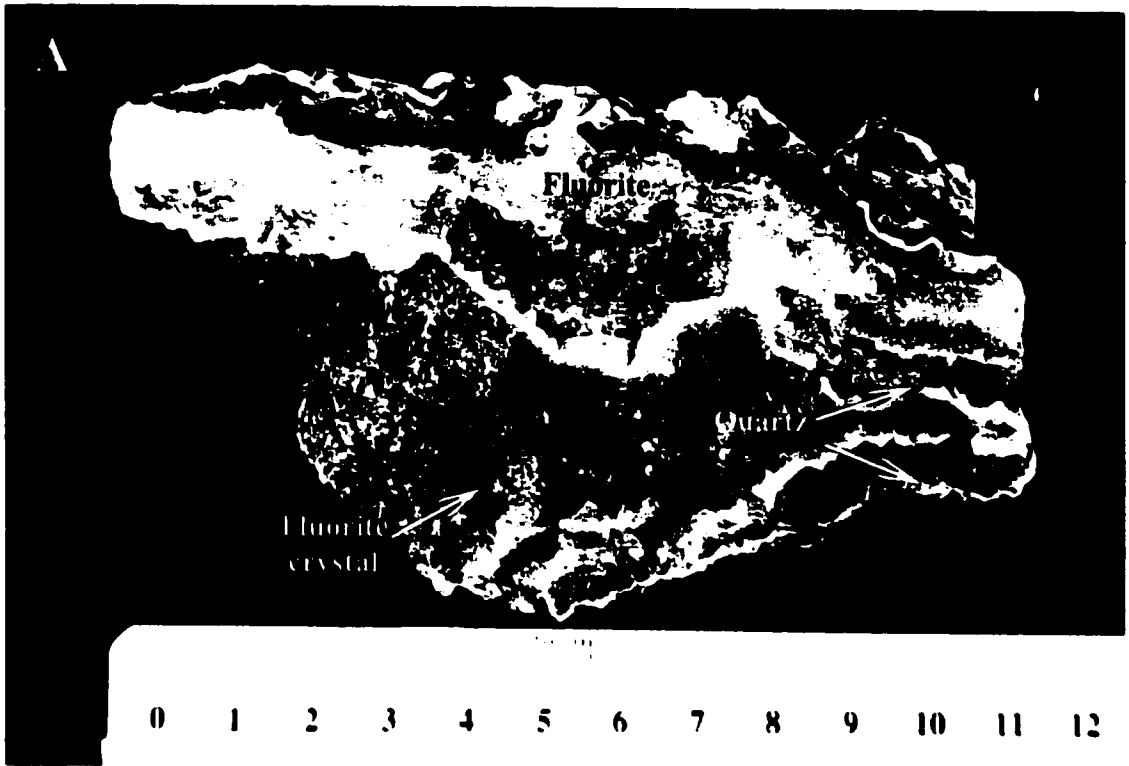


**Plate 4.4. Primary textures (Type A). Euhedral crystalline quartz bands intercalated with fluorite. (A) Crustiform bands of milky quartz intercalated with bands of white fluorite (reaching a thickness of up to 1 cm; Sample 20-K). Tiny transparent pinkish euhedral quartz crystals and one euhedral fluorite crystal line a vuggy cavity. (B) This sample has many repeated bands of crystalline comb quartz intercalated with multiple purple fluorite bands. Some fluorite bands have been fragmented and subsequently re-cemented by a later stage of silicification, forming cockade textures. Secondary potassium feldspar (adularia?) has precipitated in three lensoid shapes in the lower left quadrant of the picture (Sample 20-M).**





Hydrothermal breccias typically form because of a rapid drop in pressure and release of volatiles (Dong *et al.*, 1995). Mechanically, fracturing occurs as the pressure of ascending fluid exceeds the confining pressure and tensile strength of the surrounding host rock or overlying silica capping (Dong *et al.*, 1995). Sudden rupture of the host rock results in decompressional boiling of the ascending fluids and brecciation of the wall rocks. Such boiling would drop the fluid temperature, causing the fluid to become supersaturated with respect to silica, and therefore triggering rapid silica deposition (Dong *et al.*, 1995). Evidence of this process is displayed in the precipitation of cockade silica bands around host rock fragments, as well as the growth of randomly oriented milky quartz crystals between host rock fragments (Plate 4.5; Dong *et al.*, 1995). Although boiling is a viable mechanism of precious metal precipitation in epithermal systems, most hydrothermal breccias from the Mallery Lake area have low assay values.

## **Secondary Textures (Type B)**

### *Replacement Textures*

Replacement textures in the Mallery Lake epithermal system are represented by silicification of calcite and adularia. Textures that formed by the replacement of calcite by silica are an indication of the mechanisms of the hydrothermal system. To understand the replacement of calcite by silica, it is first important to understand how the calcite was initially deposited.

As the fluid in the system begins to cool, the solubility of calcite increases while silica solubility decreases. If the vapour pressure of the rising fluid exceeds the

**Plate 4.5. Primary textures (Type A). Brecciated wall rock followed by silica flooding. (A) Brecciated fragments of the Christopher Island Formation that is cemented by quartz, and followed by a later stage of calcite precipitation (T-Rex Zone). (B) Cockade quartz growth around brecciation fragments (Sample 14257). (C) Angular breccia fragments cemented by vuggy quartz (ST 6-1).**

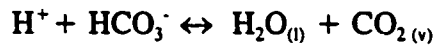


8 9 10 11 12 13 14 15 16 17 18 19

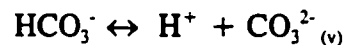


5 6 7 8 9 10 11 12 13 14 15 16 17 18 19 20 21 22

confining pressure, the system will boil, causing CO<sub>2</sub> to devolatilize from the ascending fluid by the following reaction (Fournier, 1985):



The loss of CO<sub>2</sub> to the vapour phase during boiling would cause an increase in the pH of the fluid, increasing the carbonate activity according to the following reaction (Fournier, 1985):



Calcite precipitated in response to this process typically has a bladed texture (Plate 4.6A, Plate 4.7; Dong *et al.*, 1995).

If fluid undergoes a boiling event that drives the temperature and CO<sub>2</sub> content lower, it is possible that the fluid would become supersaturated with respect to calcite and quartz, thus forming ghost-bladed or pseudoacicular textures as the calcite is replaced by silica (Dong *et al.*, 1995).

The replacement of adularia by silica and sericite indicates a fluctuation in the pH and/or temperature conditions of the hydrothermal fluid during vein formation. Increasing acidity will cause the breakdown of adularia by the following reaction (Henley and Brown, 1985):



This filling of a relic adularia cast by quartz, after the total removal of sericite, is seen in Plate 4.6B.

**Plate 4.6.** Secondary (replacement) textures (Type B). Replacement of calcite and adularia by quartz. (A) Complete silicification of calcite (cc) lattice blades by silica (Sample 712557). (B) The relic shape of an adularia crystal, hosted in the Pitz Formation host rock, has been altered (most likely to sericite) and subsequently filled with quartz (Sample 703518; crossed-polars).



*Food Measure*

from the

**National Bureau**  
Washington D. C.

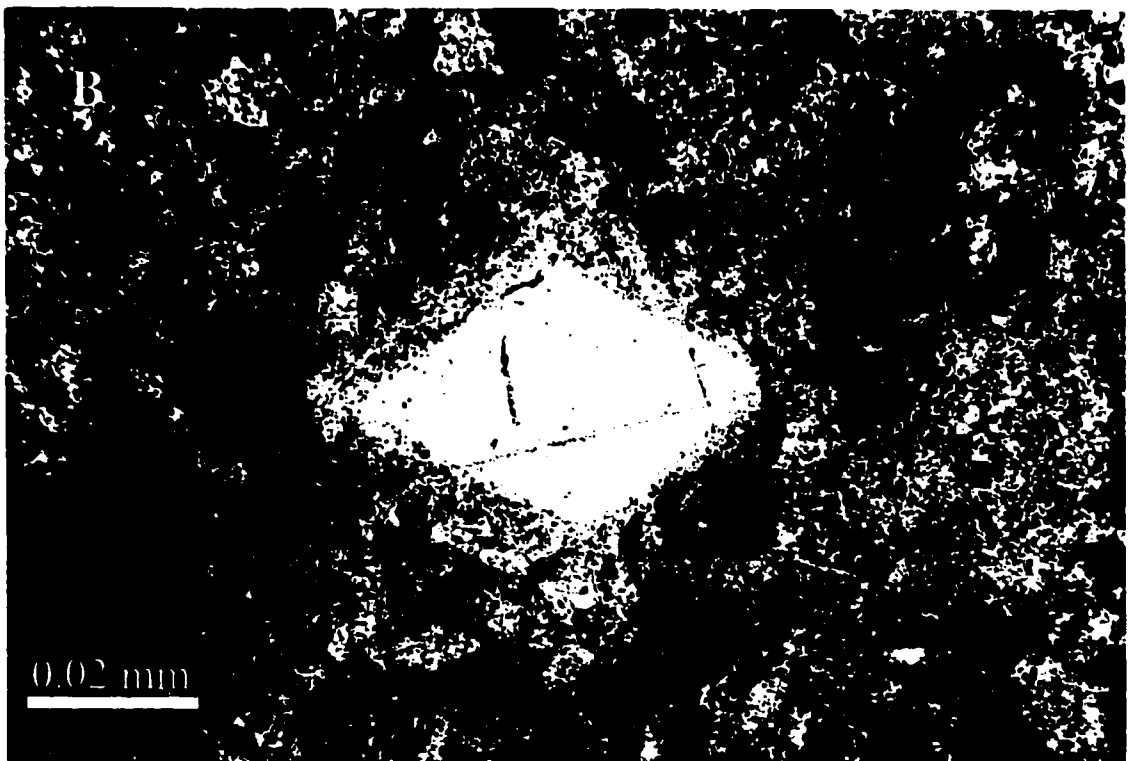


**Plate 4.7.** Secondary (replacement) textures (Type B). Microphotographs (A: plane light; B: crossed-polars) of Chal 1214 display a ghost-bladed texture. Quartz has superimposed the original bladed calcite. Bands of impurities, as well as a finer grain size denote outlines of the previous calcite blades.



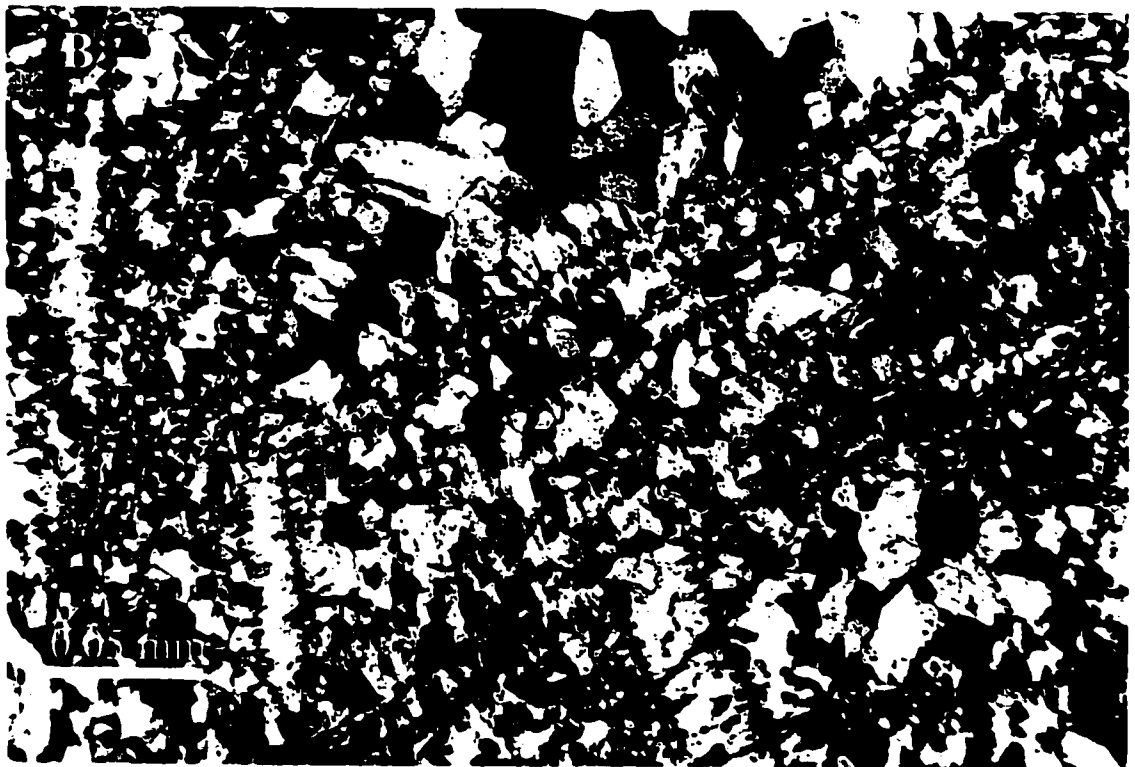
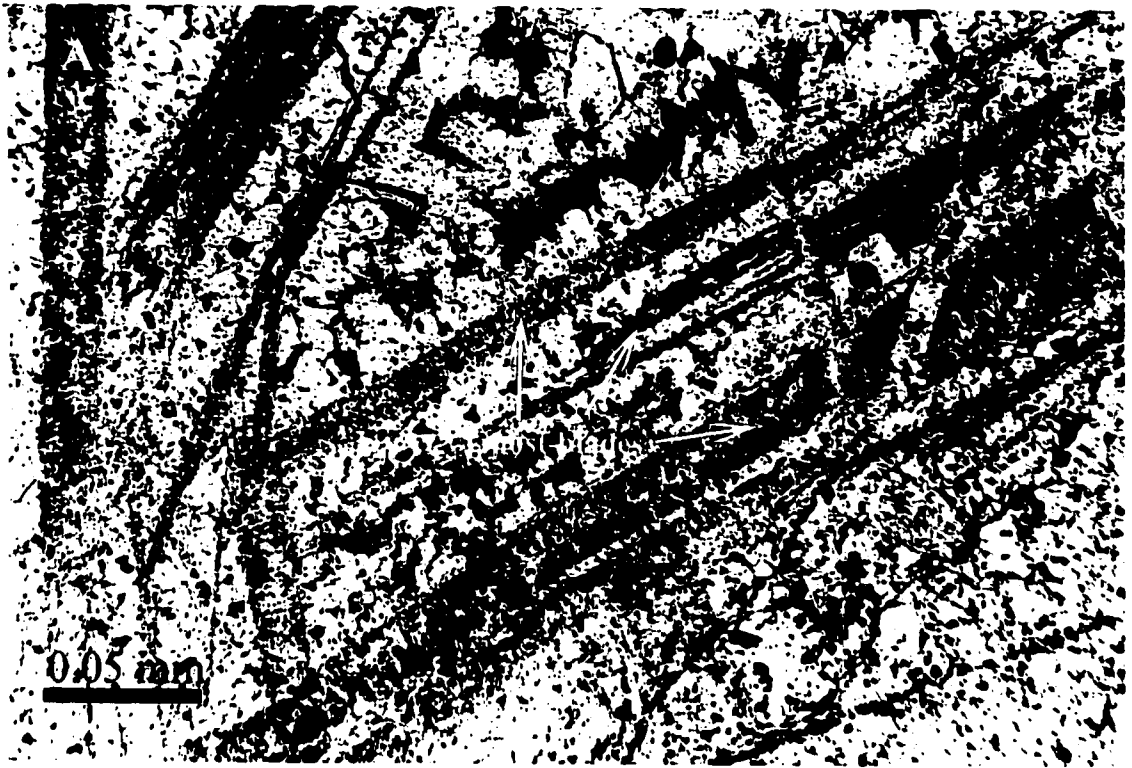


**Plate 4.8.** Secondary (recrystallization) textures (Type B). (A) This sample displays multi-colored, repetitive colloform banding cut by late stage quartz-hematite veins (Sample 703527). (B) This sample has undergone extensive reworking of the initial quartz veins, as indicated by the extent of the cross-cutting, quartz-hematite, precious metal veins. The yellowish patches of alteration were identified as kaolinite, indicating the fluids were acidic at some point during the life of the system (Sample 703530). (C) Multi-colored colloform banding (agate), alternating between iron oxidized bands (red) and white silica bands, hosted by Pitz Formation rhyolite (Sample 703518).

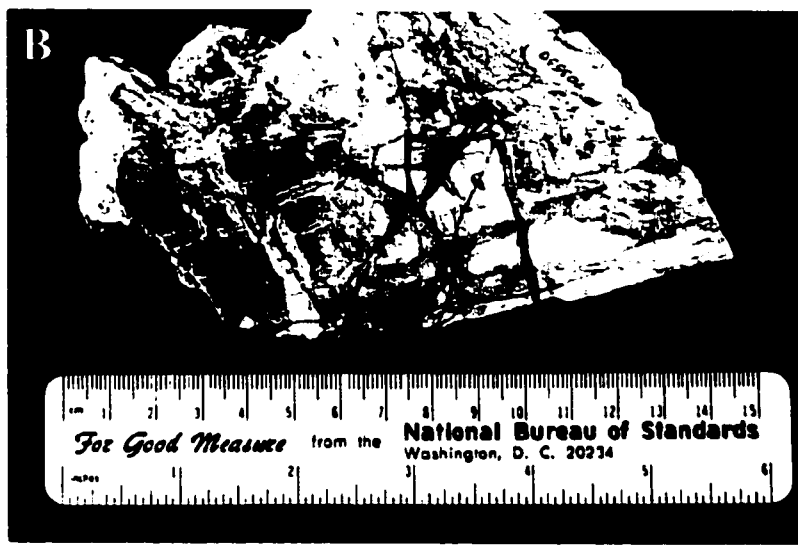
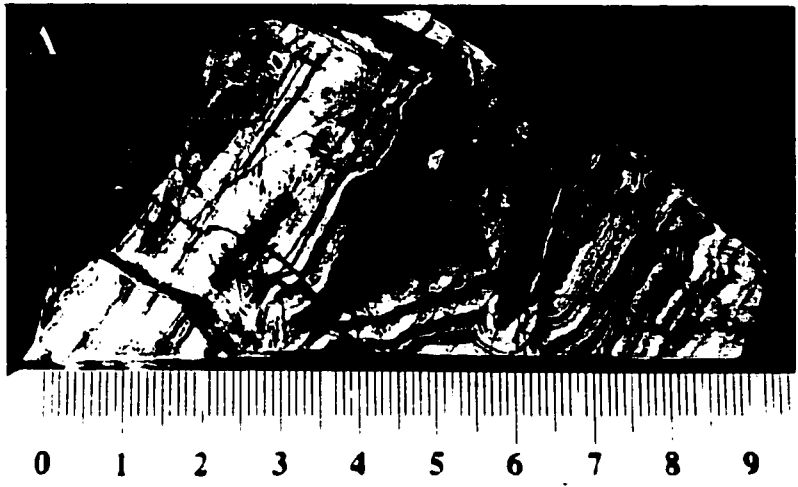


**Plate 4.9.** Secondary (recrystallization) textures (Type B) of Sample 703518. **(A)** Picture shows initial colloform chalcedony coating on a black impurity layer (bottom of picture, plane-polarized light). **(B)** Chalcedonic banding displays flamboyant texture; evidence of a late stage of recrystallization event (crossed-polars).

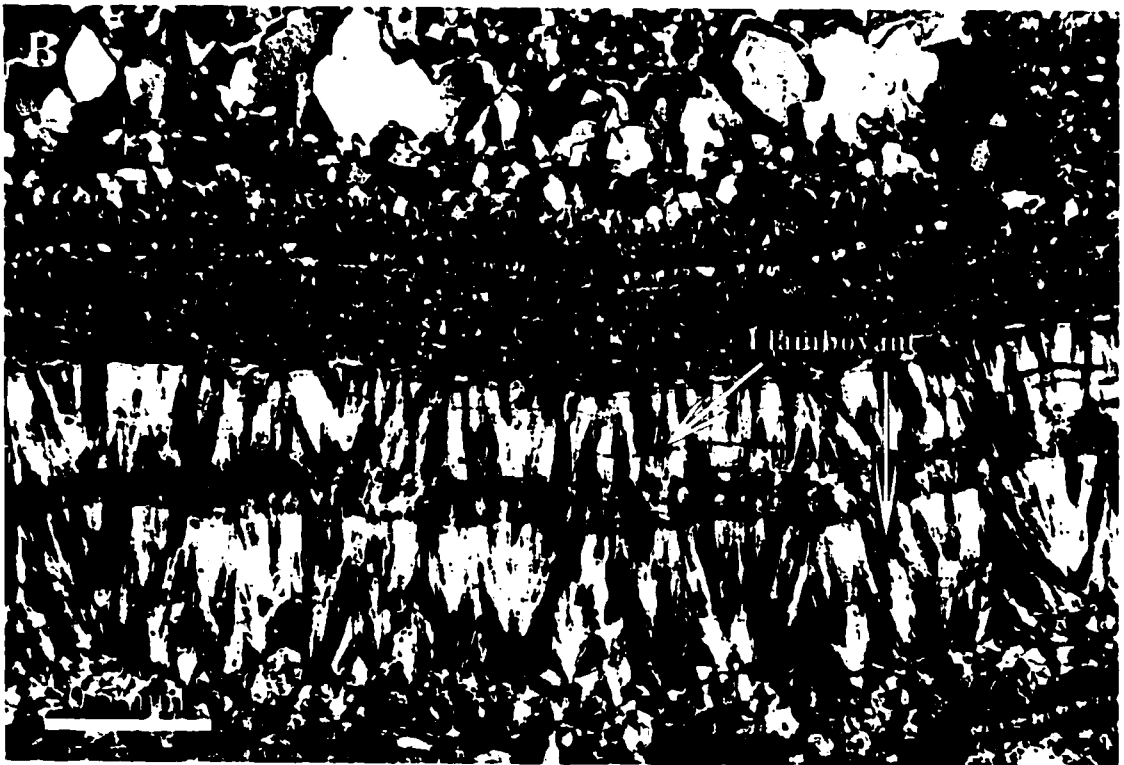
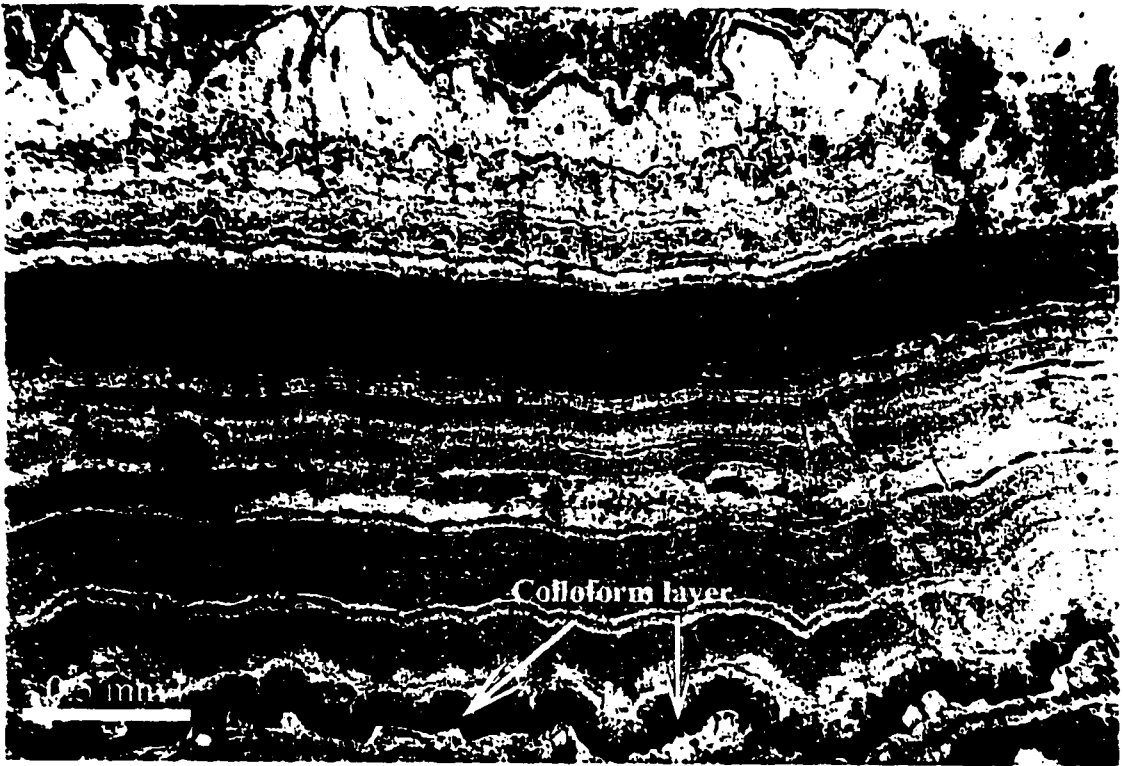


**Plate 4.10.** Secondary (recrystallization) textures (Type B) in Sample 703524. (A) Colloform and crustiform chalcedonic band growth around Pitz Formation rhyolite host rock. (B) One colloform band, pinkish in color is composed of adularia, as indicated by hydrofluoric etching and sodium cobaltinitrite staining.



8 9 10 11 12 13 14 15 16 17 18 19 20 :

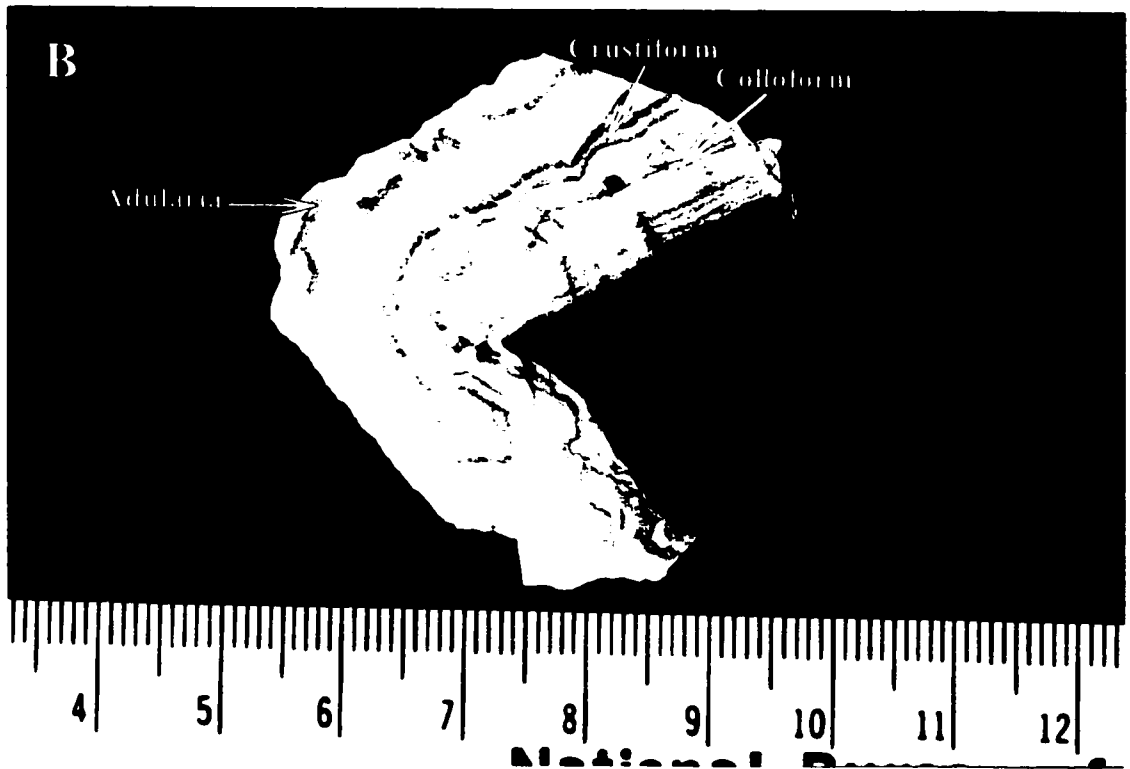


**Plate 4.11.** Secondary (recrystallization) textures (Type B) of Sample 703524. These pictures (**A**: plane light; **B**: crossed-polars) show primary colloform, cockade, and crustiform chalcedonic banding, followed by later coarse crystalline quartz growth. The chalcedony has undergone recrystallization, forming a microcrystalline mosaic texture that conforms to the relic colloform and cockade band outlines. Late stage growth of the coarse crystalline quartz replaced the last stage of colloform chalcedonic banding. This replacement is evident in the retention of trapped bands of impurities, which outline the original colloform bands, in the coarse quartz crystals.



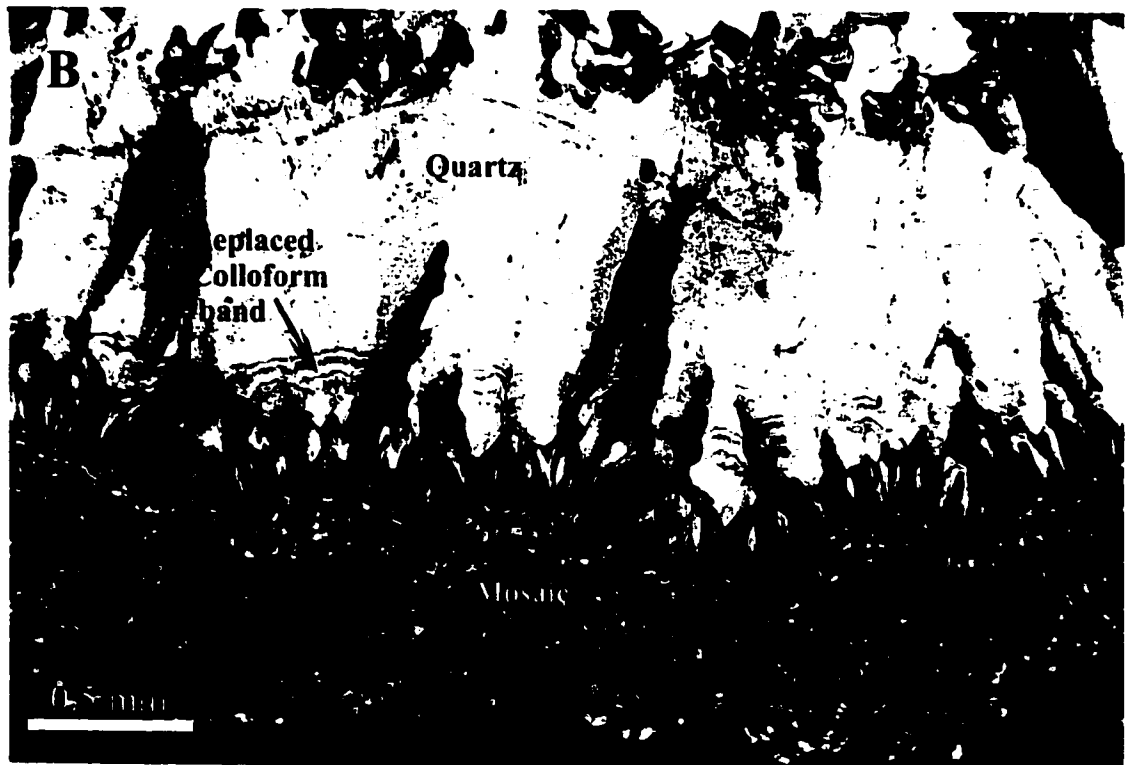
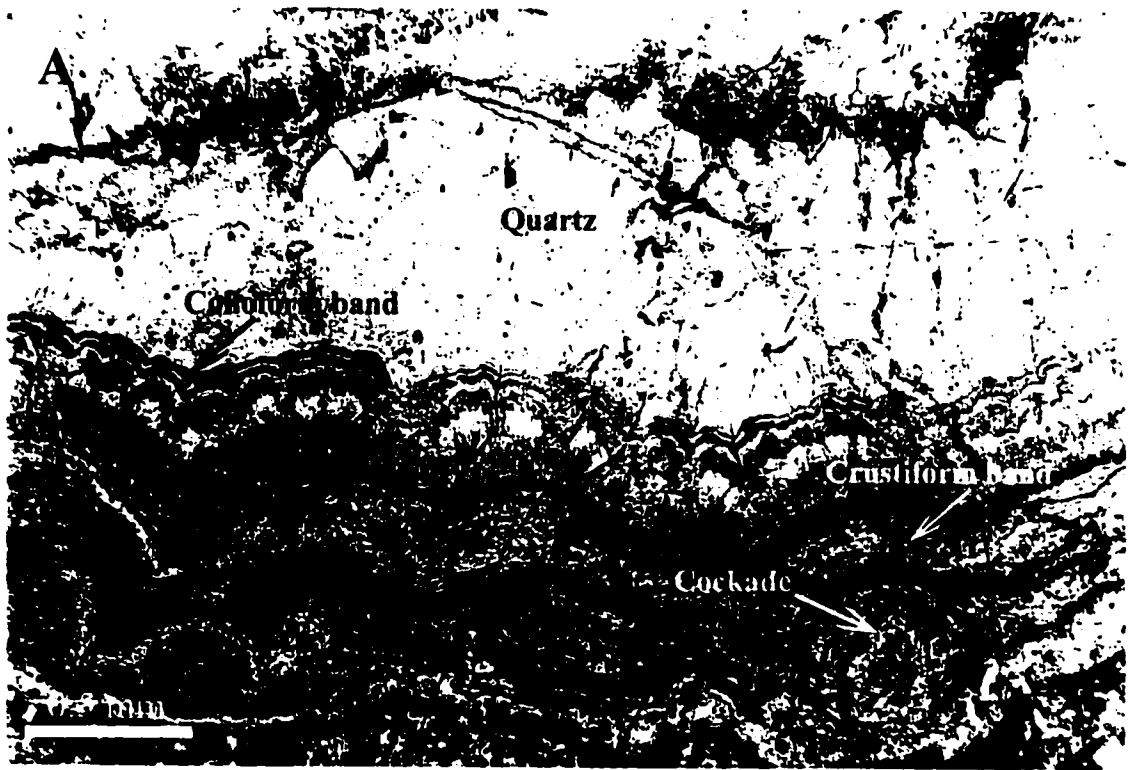


**Plate 4.12.** Secondary (recrystallization) textures (Type B) of Sample 703524 (A: plane light; B: crossed-polars). A zoned quartz crystal displays a feathery (splintery) recrystallization texture (B). This feathery texture is well developed on the margins of grains with clear euhedral cores in this picture.

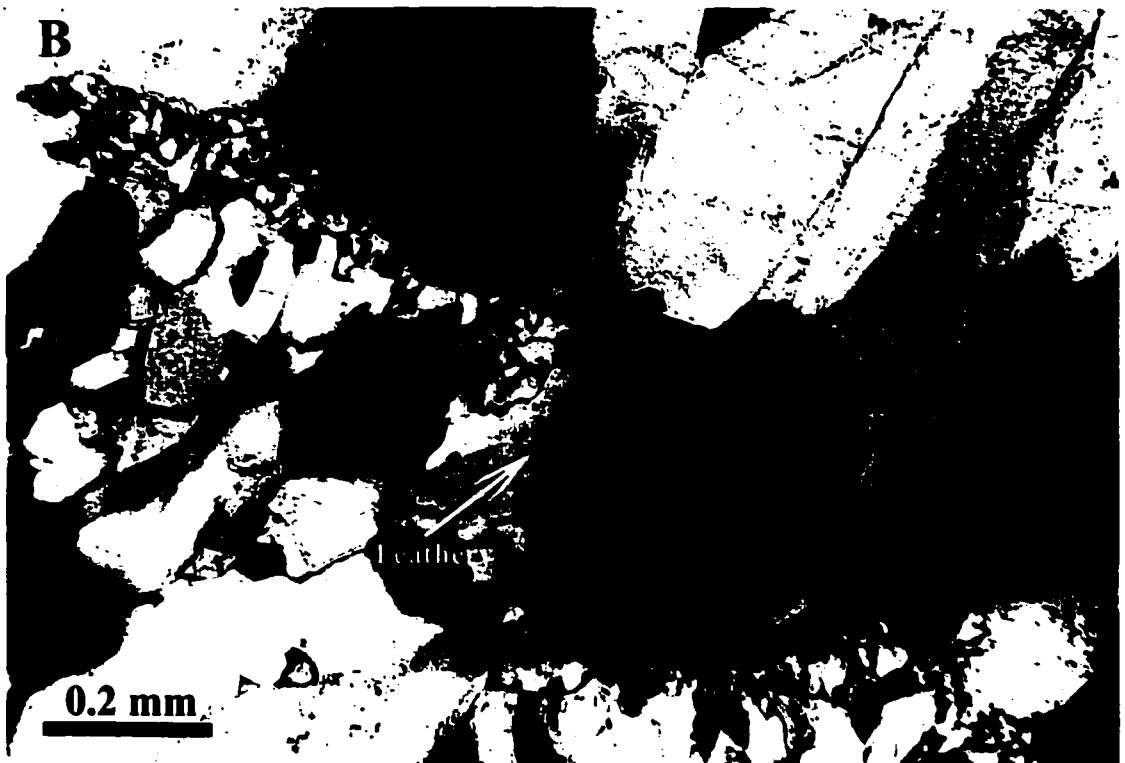
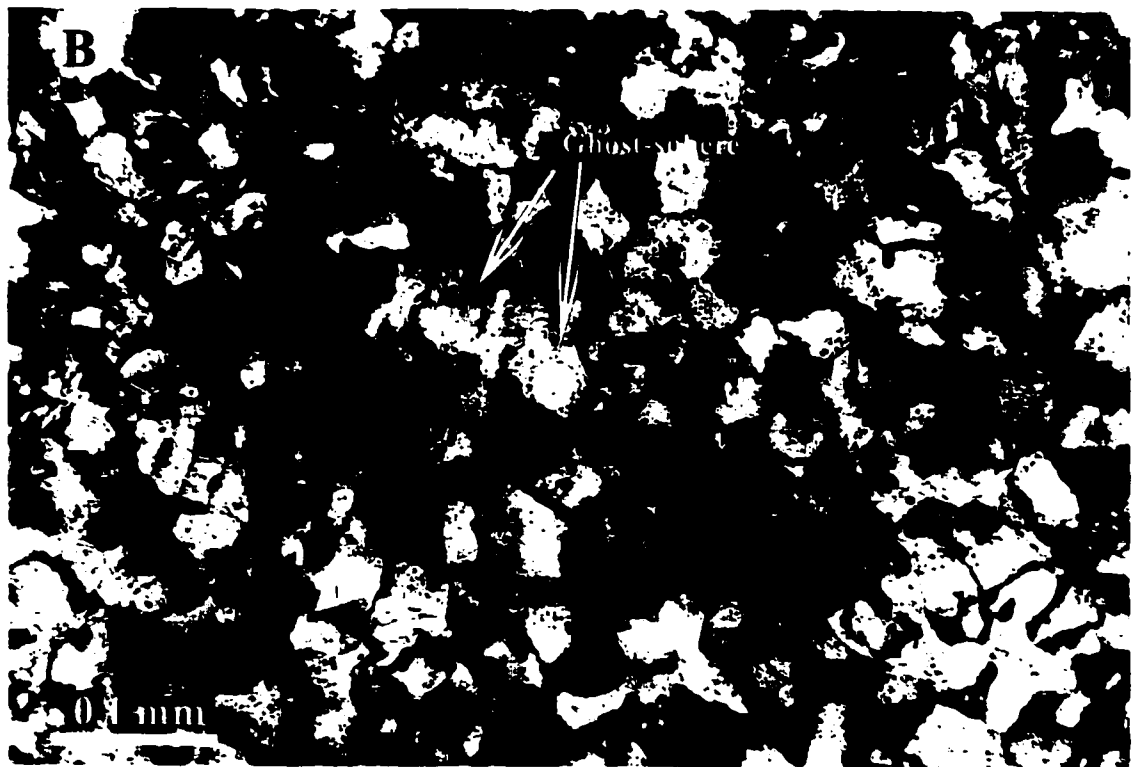
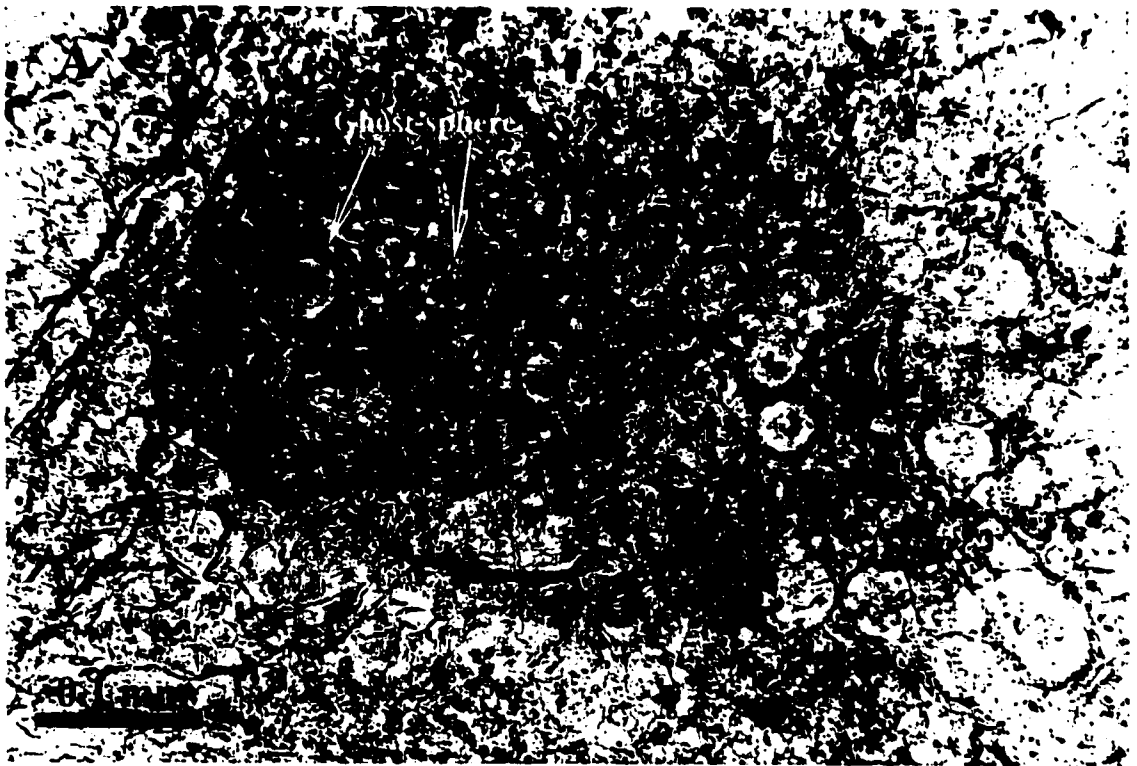


**Plate 4.13.** Secondary (recrystallization) textures (Type B) of Sample 703524. Pictures **A** (plane light) and **B** (crossed-polars) show the outline of cloudy spheres highlighted by black impurities, in a quartz vein. Bobis (1994) attributes the rounded forms of the ghost-sphere texture to represent recrystallization of silica gel, which preserved the original structure and impurities of the silicate (i.e. silica, chalcedony, or quartz) phase.



### *Recrystallization Textures*

Recrystallization textures such as colloform, mosaic, feathery, ghost-sphere, and flamboyant indicate a silica gel precursor prior to recrystallization as silica (Plates 4.8, 4.9, 4.10, 4.11, 4.12, and 4.13; Dong *et al.*, 1995). Fournier (1985) proposed the following mode of formation for silica gel: fluids supersaturated with respect to amorphous silica will undergo rapid nucleation of silica into colloidal particles, followed by polymerization and coagulation into a gelatinous material. Conditions that lead to silica supersaturation in the fluid, and the subsequent deposition of amorphous silica, may involve rapid cooling or boiling (Dong *et al.*, 1995).

Examination of the precious metal-bearing veins in the Mallery Lake area indicates that silica was initially precipitated as amorphous silica, typically as chalcedony. It is plausible that the precious metal deposition in the Mallery Lake veins may have undergone a combination of mechanisms such as: (1) precious metal transport by colloidal silica particles (Fournier, 1985; Saunders, 1990); and/or (2) the severity of the boiling (i.e. violent vs. simmering) within the system. Both mechanisms are viable methods of depositing precious metals from the fluid, if this fluid was responsible for the transport of precious metals.

## **CHAPTER 5**

### **FLUID INCLUSION STUDY OF THE HYDROTHERMAL VEINS AT MALLERY LAKE**

#### **Introduction**

Microthermometric analyses were conducted on fluid inclusions from selected quartz veins in the Mallery Lake area in order to obtain information about the composition of the fluids, and the pressure and temperature at which the fluids were trapped. The objective of the fluid inclusion study is to tie one of the fluid types to the deposition of precious and base metals.

#### **Methodology**

The majority of the microthermometric analyses were conducted on a USGS gas-flow heating-freezing stage (Were *et al.*, 1979), and a THMSG600 Linkam stage. Calibration was achieved using synthetic fluid inclusion standards manufactured by Syn Fline. Standard microthermometric measurement errors are  $\pm 0.2^\circ\text{C}$  for freezing and  $\pm 2^\circ\text{C}$  for heating to  $300^\circ\text{C}$ . Salinities of the dilute fluids were calculated from final ice-melting temperatures using the equation of Bodnar and Vityk (1995) for the  $\text{H}_2\text{O}$ - $\text{NaCl}$  system, whereas the compositions of saline, multi-component fluids were determined graphically. The graphical approach yielded total weight percent salinity, as well as the relative abundance of  $\text{CaCl}_2$  to  $\text{NaCl}$ , based on the  $\text{NaCl}$ - $\text{CaCl}_2$ - $\text{H}_2\text{O}$  ternary phase diagrams of Oakes *et al.* (1990, 1992).

Depressed eutectic melt temperatures are caused by the presence of Ca or Mg chlorides in the fluid, therefore thermal decrepitation of fluid inclusions, and the

subsequent examination of the decrepitation solutes was used to constrain fluid compositions. Fluid inclusion chips were heated up to temperatures ~ 360°C until decrepitation of the fluid inclusions occurred. The sample was then coated with a thin layer of chromium in preparation for microprobe analysis. Microprobe EDS (Energy-Dispersive Spectroscopy) analysis was used to analyze the dehydrated salt piles that formed on the surface of the fluid inclusion chip during the thermal decrepitation process.

### **Criteria for Selection of Fluid Inclusions**

The focus of the microthermometric study was to constrain the hydrothermal fluids of the system by analyses of unnecked primary fluid inclusions in or between growth bands in quartz. Necking is the result of a thermodynamic drive in a fluid inclusion to minimize its surface free energy by changing shape (Roedder, 1984). The drive of fluid inclusions to change to shapes with lower surface energies (i.e. a spherical or negative crystal shape) may result in the trapping of all-liquid inclusions, or inclusions with variable liquid to vapor volumetric phase ratios (Bodnar *et al.*, 1985). It is therefore critical that the fluid inclusions selected for microthermometric analysis are either volumetrically equal in liquid-to-vapor proportions, or isolated and show no signs of secondary origin or necking (Bodnar *et al.*, 1985). These rigid criteria for fluid inclusion selection restrict the majority of the fluid inclusions to quartz. Furthermore, chalcedony and amorphous silica are omitted from the study because they typically contain small inclusions that have been recrystallized, and thus are suspect (Goldstein and Reynolds, 1994). The obvious drawback is that the



restricted criteria limits the results to only those fluids trapped during lower flow rates and reduced silica saturation conditions. Nevertheless, the advantage to following these rigid criteria is that it does eliminate the majority of the problems associated with interpreting data that include secondary inclusions.

### **Fluid Inclusion Type Classification**

Classification of fluid inclusion types in the veins at Mallery Lake is based on the phase changes observed during heating and freezing. Two end-member fluid types were observed: Type 1 dilute fluids trapped at moderate temperatures; and Type 2 saline, lower temperature fluids. Both fluid inclusion populations were frequently present in separate growth bands within the same sample, on the scale of tens to hundreds of micrometers (Plate 5.1). Sample locations of the veins selected for microthermometric analysis are shown in Figures 3.1, 3.2, and 3.3.

#### ***Type 1 Dilute Fluid Inclusions***

Type 1 fluids are characterized by three-phase (liquid + vapor + solid = L:V:S), two-phase (liquid + vapor = L:V), and vapor-rich inclusions. Three Type 1 fluid subcategories exist: low salinity to pure water fluids that occasionally contain pseudodaughter minerals (Type 1A); similarly dilute fluids that contain pseudodaughter minerals and minor to trace CO<sub>2</sub> gas (Type 1B); and vapor-rich fluid inclusions (Type 1C).

**Plate 5.1.** Fluid inclusion growth bands in a euhedral quartz crystal (Sample 14257). Microthermometric analysis indicated that Type 1 and Type 2 fluid inclusions are isolated to different growth bands, thus evidence against fluid mixing.



Type 2

Type 1

0.2 mm

## **Results**

### ***Type 1A fluid inclusions***

Type 1A fluids are spatially widespread at Mallery Lake and frequently occur as primary inclusions that are trapped along or between growth bands. Inclusions are up to 40  $\mu\text{m}$  in length, and have liquid-to-vapor volumetric phase ratios of typically 90% (Table 5.1; Plate 5.2). The solid phase in the three-phase (L:V:S) inclusions was identified optically and semi-quantitatively by SEM analysis as muscovite (Plate 5.3). These trapped pseudodaughter minerals of muscovite are rare, occurring in less than <5% of the Type 1A fluid inclusions, and therefore are interpreted to have been trapped heterogeneously.

Final melting temperatures of ice typically occur between  $-0.2^{\circ}\text{C}$  and  $0.0^{\circ}\text{C}$ , but a few inclusions have  $T_{m_{\text{ice}}}$  values as low as  $-2^{\circ}\text{C}$ , reflecting low to negligible salt in these fluids (Plate 5.4). Maximum salinities are calculated to be 3.4 wt. % NaCl equivalent (for inclusions with final ice melting at  $\sim -2^{\circ}\text{C}$ ). Because of these low salinities it was generally impossible to observe eutectic melting, which would have helped identify the nature of the salts present. Homogenization temperatures from the Type 1A fluids typically range from  $150^{\circ}\text{C}$  to  $180^{\circ}\text{C}$  (Table 5.1; Figure 5.1).

### ***Type 1B fluid inclusions***

The Type 1B fluid inclusions were observed at only one locality (ST-12-6). Fluid inclusions of this type are typically large, commonly having lengths between 60  $\mu\text{m}$  and 80  $\mu\text{m}$ . The solid phases in the three-phase inclusions include muscovite, as well as dawsonite ( $\text{NaAl}(\text{CO}_3)(\text{OH})_2$ ) from its orthorhombic crystal structure, as well a

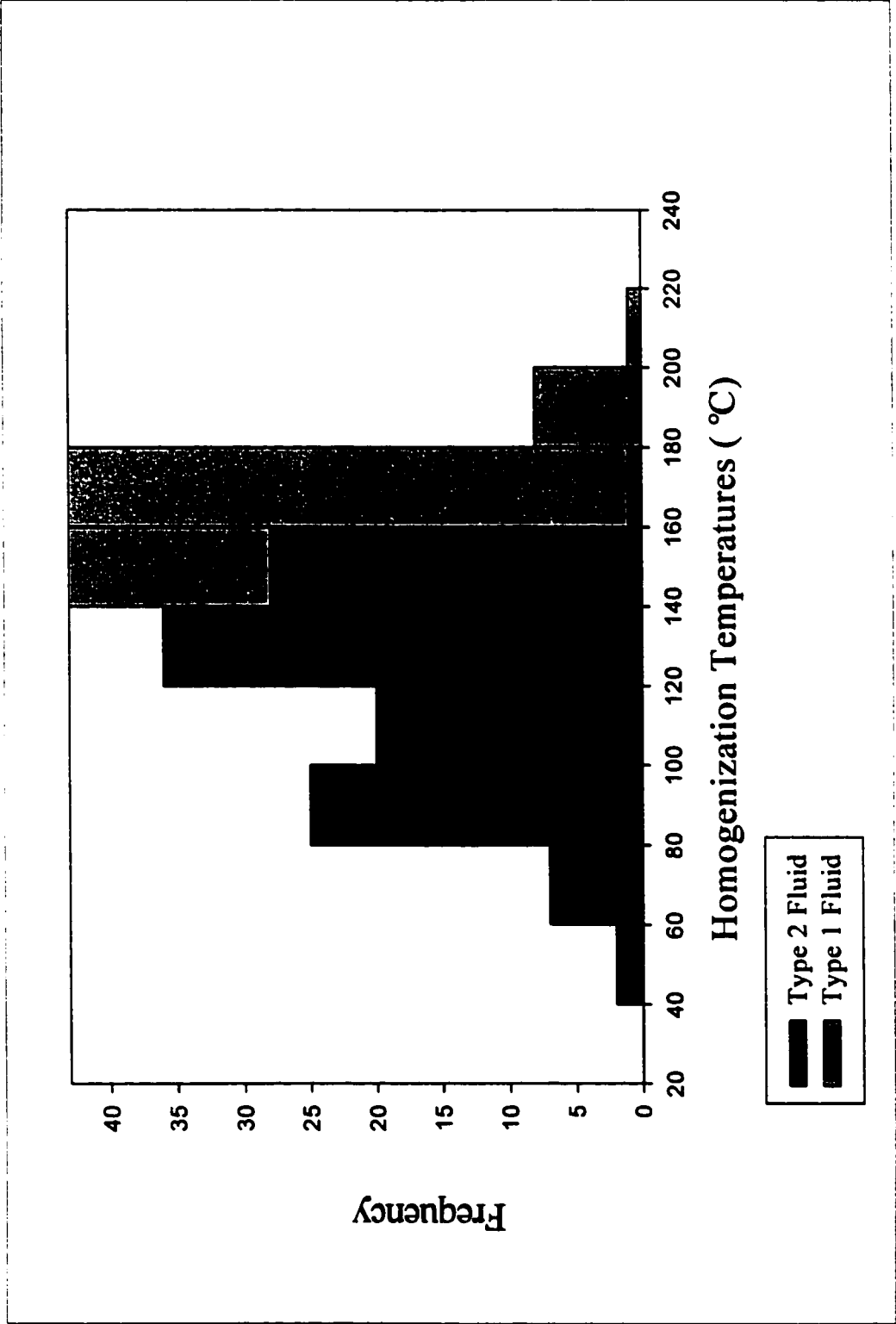


**Figure 5.1. Frequency of the Homogenization Temperatures for Fluid Types 1 and 2**

**Table 5.1. Microthermometric measurements of the veins in the Mallery Lake area**

Sample #	Inclusion	Origin	Area (um)	Phase	% Liquid	T <sub>e</sub> (mstbl)	T <sub>e</sub> (tbl)	T <sub>m</sub> (ice)	wt.-% NaCl equivalent	T <sub>m</sub> (H)	T <sub>H</sub> (L) °C	Comments
14257	1	S	39*17	L/V	95	(-80 to -70)		-29	29		63	
	2	Ps	14*10	L/V	85	(-80 to -70)		-38	35		98	
	3	S	10*8	L/V	95			-36	34		56	
	4	Ps	10*6	L/V	80			Nf				
	5	S	8*5	L/V	95			-32	30		96	
	6	S	15*6	L/V	95	(-80 to -70)		-30	29		93	
	7	S	12*5	L/V/S	95			-29	28		99	
Ave. Fluid Type #2							-28	28			84	
Std. Dev. Type #2							3	-7			18	
14257	1	S	10*3	L/V	95			-1	1		254.9*	
	2	S	14*12	L/V	85			-2	3		282.6*	
	3	S	35*12.5	L/V	85			-2	3		262.4*	
	4	Ps	6*5	L/V	75			-1	1		7	
	5	Ps	8*6	L/V	75			-1	2		268*	
	6	Ps	10*8	L/V	70			-1	1		7	
	7	Ps	12*7	L/V	75			-1	2		215*	
	8	Ps	12*6	L/V	80			-1	2		256.9*	
	9	Ps	32*14	L/V	80			-1	1		273.1*	
	10	Ps	10*10	L/V	70			-2	3		7	
Ave. Fluid Type #1							-1	2			7	
Std. Dev. Type #1							0	-1			7	
14257	1	P	14*5	L/V	90	N/A	0.0	0	0		176	
	2	P	20*11	L/V	90	N/A	7-12	0	0		215	
	3	P	7.5*5	L/V	90	N/A	7-0.2	0	0		182	
	4	P	12.5*5	L/V	95	N/A	7-0.2	0	0		182	
	5	P	10*5	L/V	93	N/A	7	0	0		165	
	6	P	5*5	L/V	95	N/A	7	0	0		163	
	7	P	8*3.5	L/V	95	N/A	0.0	0	0		155	
	8	P	12.5*12.5	L/V	50	N/A	0.0	0	0		7	
	9	P	7*6	L/V	40	N/A	0.0	0	0		264	
Ave. Fluid Type #1							0	0			176.6	
Std. Dev. Type #1							0	0			18.2	
Type 2 (Plate 5.1)	1	P	37.5*12.5	L/V	95	-84.5	-55.0	-34	32		99	
	2	P	25*7.5	L/V/S	95	-79	7	-37	34	-5.1	112	salt melt by 115 °C
	3	P	15*5	L/V	95	-79	-55.0	-43	39		121	
	4	P	7.5*4	L/V	95	-77	7	-37	34		126	
	5	P	15*5	L/V	95	-77	7	-37	34		130	
	6	P	30*7	L/V	95	-77	7	-37	34		94	
	7	P	10*5	L/V	95	-77	0.0	-37	34		94	
	8	P	12.5*3.5	L/V	95	-77	0.0	-37	34	-3.7	93	
Ave. Fluid Type #2							-37	34			108.7	
Std. Dev. Type #2							2	-4			14.5	



703527 (b)

1	P	L.V	N/A	-(-2.10.0)	0	0	278°
2	P	L.V	N/A	-(-2.10.0)	0	0	263°
3	P	L.V	N/A	-(-2.10.0)	0	0	196°
4	P	L.V	N/A	-(-2.10.0)	0	0	299°
5	P	L.V	N/A	-(-2.10.0)	0	0	230°
6	P	L.V	N/A	-(-2.10.0)	0	0	196°
7	P	L.V	N/A	-(-2.10.0)	0	0	210°
8	P	L.V	N/A	-(-2.10.0)	0	0	300°
9	P	L.V	N/A	-(-2.10.0)	0	0	215°
10	P	L.V	N/A	-(-2.10.0)	0	0	275°
11	P	L.V	N/A	-(-2.10.0)	0	0	301°
12	P	L.V	N/A	-(-2.10.0)	0	0	270°
13	P	L.V	N/A	-(-2.10.0)	0	0	328°
14	P	L.V	N/A	-(-2.10.0)	0	0	335°
15	P	L.V	N/A	-(-2.10.0)	0	0	279°
16	P	L.V	N/A	-(-2.10.0)	0	0	283°
17	P	L.V	N/A	-(-2.10.0)	0	0	215°
18	P	L.V	N/A	-(-2.10.0)	0	0	320°
19	P	L.V	N/A	-(-2.10.0)	0	0	258°
20	P	L.V	N/A	-(-2.10.0)	0	0	265°
21	P	L.V	N/A	-(-2.10.0)	0	0	302°
22	P	L.V	N/A	-(-2.10.0)	0	0	250°
23	P	L.V	N/A	-(-2.10.0)	0	0	258°
24	P	L.V	N/A	-(-2.10.0)	0	0	320°
25	P	L.V	N/A	-(-2.10.0)	0	0	302°
Ave Fluid Type #1							7
Std. Dev. Type #1							7

703534 (E)

1	P	L.V	90	-75	7	-35	33	91
2	P	L.V	90	-75	7	-33	31	96
3	P	L.V	90	-75	7	-45	42	88
4	P	L.V	95	-77	7	-42	39	93
5	P	L.V	90	-77	7	-34	32	87
6	P	L.V	90	-77	7	-34	32	134
7	P	L.V	90	-77	7	-40	36	137
8	P	L.V	90	-74	7	-38	35	127
9	P	L.V	95	-74	7	-35	32	124
10	P	L.V	85	-74	7	-38	35	131
Ave Fluid Type #2							111	
Std. Dev. Type #2							20	

salt melt temp not recorded  
salt melt temp not recorded

703534

1	P	L.V	95	-74	7	-33	31	132
2	P	L.V	95	-74	7	-41	38	123
3	P	L.V	95	-77	7	-31	30	90
4	P	L.V	95	-77	7	-20	23	155
5	P	L.V	95	-77	7	-33	31	132
6	P	L.V	90	-77	7	-22	24	163
7	P	L.V	95	-77	7	-32	31	97
8	P	L.V	95	-76	7	-37	35	124
9	P	L.V	95	-75	7	-39	36	123
10	P	L.V	95	-75	7	-32	30	141
Ave Fluid Type #2							31	
Std. Dev. Type #2							128	



703534	1	P	9*5	L.V	95	-76	?	-27	27	136
	2	P	7*4	L.V	95	-73	?	-26	27	145
	3	P	13*3	L.V	95	-73	?	-26	27	140
	4	P	7.5*5	L.V	95	-74	?	-26	27	142
	5	P	20*13	L.V	95	-73	?	-26	27	151
	6	P	12*12	L.V	95	-73	?	-26	27	132
	7	P	12.5*6	L.V	95	-73	?	-26	27	148
	8	P	4*2	L.V	95	-73	?	-26	27	144
	9	P	10*5	L.V	95	-73	?	-26	26	133
	Ave. Fluid Type 2							-26	27	141
	Std. Dev. Type 2							0	-1	6
703534	1	P	40*17	L.V	90	-70	?	-50	49	145
	2	P	15*12	L.V	95	-70	?	-52	51	146
	3	P	12*8	L.V	95	-70	?	-42	39	137
	4	P	15*10	L.V	95	-70	?	-41	37	134
	5	P	16*16	L.V	90	-70	?	-34	32	159
	6	P	14*14	L.V	90	-70	?	-35	32	158
	7	P	35*25	L.V.S	90	-70	?	-35	32	152
	8	P	30*30	L.V	95	-70	?	-35	32	143
	9	P	15*12	L.V.S	95	-70	?	-40	37	64
	10	P	12*7	L.V.S	95	-70	?	-46	43	136
	Ave. Fluid Type 2							-42	38	137
	Std. Dev. Type 2							6	-13	26
14280 (A)	1	P	23*10	L.V	95	(-90 to -80)	?	-44	41	145
	2	P	20*10	L.V	95	(-90 to -80)	?	-46	42	136
	3	P	32*17	L.V	95	(-90 to -80)	?	-44	40	196
	4	P	17*7	L.V	95	(-90 to -80)	?	-45	0	143
	5	P	10*12	L.V	95	(-90 to -80)	?	-45	42	?
	6	P	60*37	L.V	95	(-90 to -80)	?	-44	41	163
	7	P	16*8	L.V	95	(-90 to -80)	?	-45	42	139
	8	P	37.5*12.5	L.V	95	(-90 to -80)	?	NF	0	246*
	9	P	12.5*5	L.V	95	(-90 to -80)	?	-48	46	111
	10	P	15*6	L.V	95	(-90 to -80)	?	NF	0	258*
	11	P	15*5	L.V	95	(-90 to -80)	?	-45	42	154
	12	P	30*12.5	L.V	95	(-90 to -80)	?	-44	41	86*
	13	P	10*7.5	L.V	95	(-90 to -80)	?	-49	46	145
	14	P	25*15	L.V	95	(-90 to -80)	?	-46	44	145
	15	P	9*5	L.V.S	95	(-90 to -80)	?	-49	47	143
	16	P	45*30	L.V	90	(-90 to -80)	?	-43	40	312*
	Ave. Fluid Type 2							-46	43	130
	Std. Dev. Type 2							2	-3	12
St-28-2	1									158
	2									117
	3									114
	4									125
	5									140
	6									145
	7									133
	Ave. Fluid Type 2									133
	Std. Dev. Type 2									15

salt melt temp. not recorded  
 salt melt by 122 °C  
 salt melt temp. not recorded

salt melt > 350 °C

No freezing data recorded as reconnaissance freezing run characterized inclusions as high salinity

17" Vein	1	P	15'5	L.V	98	(-85 to -75)	?	-37	34	111
	2	P	13'12	L.V	98	(-85 to -75)	?	-33	31	98
	3	P	17'5'8	L.V	98	(-85 to -75)	?	-43	40	103
	4	P	25'13	L.V	95	(-85 to -75)	?	-39	36	137
	5	P	20'20	L.V	95	(-85 to -75)	?	-32	31	118
	6	P	20'7.5	L.7	99	(-85 to -75)	?	-31	30	?
Ave. Fluid Type #1							0	0	0	?
Std. Dev. Type #1							0	0	0	?

17" Vein	1	P	12'8	L.V	90		4	0	0	330°
	2	P	15'7	L.V	98		?	?	?	301°
	3	P	15'8	L.V	90		-2	0	0	192°
	4	P	17'15	L.V	95		0	0	0	206°
	5	P	35'25	L.V	92		?	0	0	
	6	P	25'13	L			-1	0	0	
	7	P	17'5'13	L			-1	0	0	
	8	P	13'8	L.V	90		-0.4	0	0	293°
	9	P	15'8	L.V	91		-0.4	0	0	225°
	10	P	7'7	L.V	85		-0.4	0	0	319°
Ave. Fluid Type #2							-36	33	113	
Std. Dev. Type #2							4	-9	14	

T-REX Zone Oct 4/97	1	P	35'18	L.V	98	(-85 to -75)	?	-48	46	90
	2	P	15'13	L.V	96		?	?	?	78
	3	P	12'12	L.V	98		?	?	?	81
	4	P	20'12	L.V	98	(-85 to -75)	?	-48	46	76
	5	P	20'12	L.V	98		?	?	?	69
	6	P	17'10	L.V	98		?	?	?	91
	7	P	25'17	L.V	98	(-85 to -75)	?	-48	46	77
	8	P	10'5	L.V	98	(-85 to -75)	?	-48	46	92
	9	P	30'18	L.V	98	(-85 to -75)	?	-50	49	?
	10	P	18'10	L.V	98	(-85 to -75)	?	-48	46	92
	11	P	11'10	L.V	98	(-85 to -75)	?	-48	46	?
	12	P	70'25	L.V	98	(-85 to -75)	?	-55	57	89
	13	P	80'10	L.V	97	(-85 to -75)	?	-48	46	87
Ave. Fluid Type #2							-49	47	84	
Std. Dev. Type #2							2	-4	8	

Fluorite Zone Jan 9/99	1	P(gb)	4'7	L.V	95	N/A	0	0	0	166
	2	P(gb)	5'8	L.V	95	N/A	0	0	0	163
	3	P(gb)	5'7	L.V	95	N/A	0	0	0	?
	4	P(gb)	5'7	L.V	95	N/A	0	0	0	168
	5	P(gb)	4'7	L.V	95	N/A	0	0	0	195
Ave. Fluid Type #1							0	0	0	173
Std. Dev. Type #1							0	0	0	13

Fluorite Zone Jan 9/99	6	P(gb)		L	N/A		-52	-37	34	N/A
	7	P(gb)		L	N/A		-52	-35	33	N/A
	8	P(gb)		L.V	95		-52	-40	37	?
	9	P(gb)		L.V	95		-52	-39	36	?
Ave. Fluid Type #2							-38	35		
Std. Dev. Type #2							2	-4		





**Plate 5.2.** Type 1A fluid inclusions in sample ST-12-6. Type 1A fluid inclusions in a ~ 300  $\mu\text{m}$ -wide growth band (A). Below, close up of one of the two-phase (L:V) Type 1A inclusion from this growth band (B).

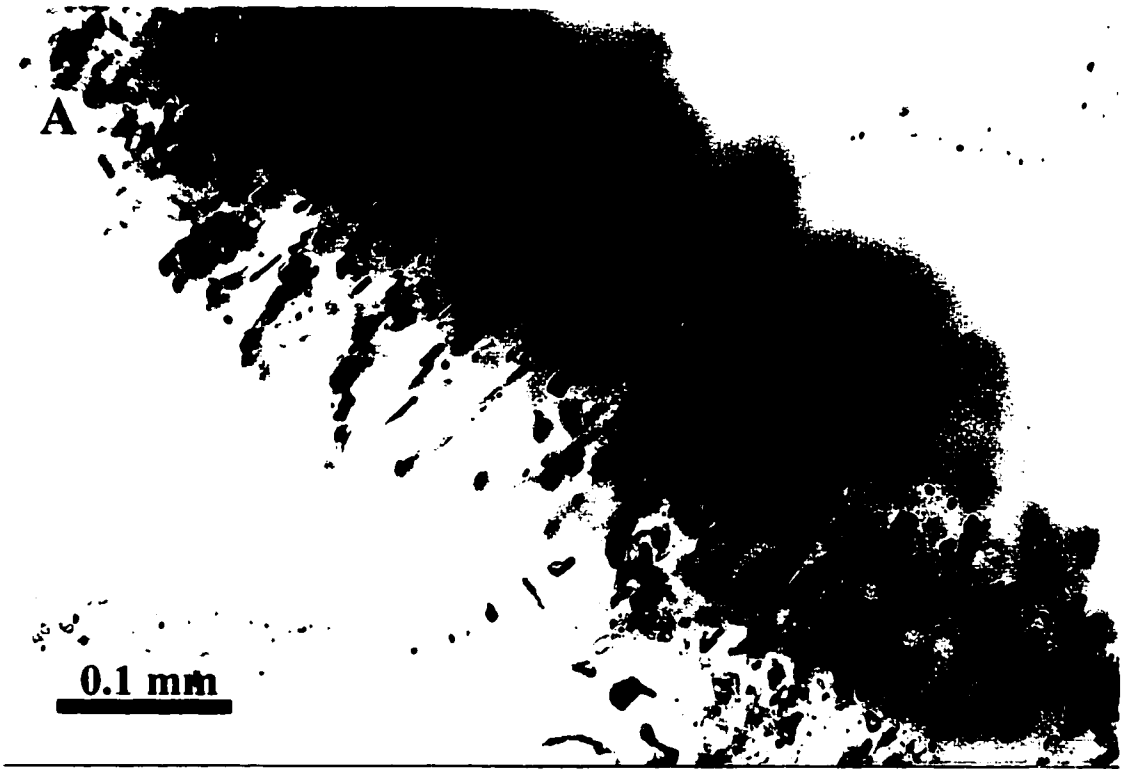


**Plate 5.3.** Muscovite pseudodaughters in Type 1A fluid inclusion (Fluorite zone). Above, a scanning electron microscope picture of a decrepitated Type 1A fluid inclusion with pseudodaughter muscovite books (A). Below, a three-phase (L:V:S) Type 1a fluid inclusion with muscovite (sericite) pseudodaughter minerals (B).

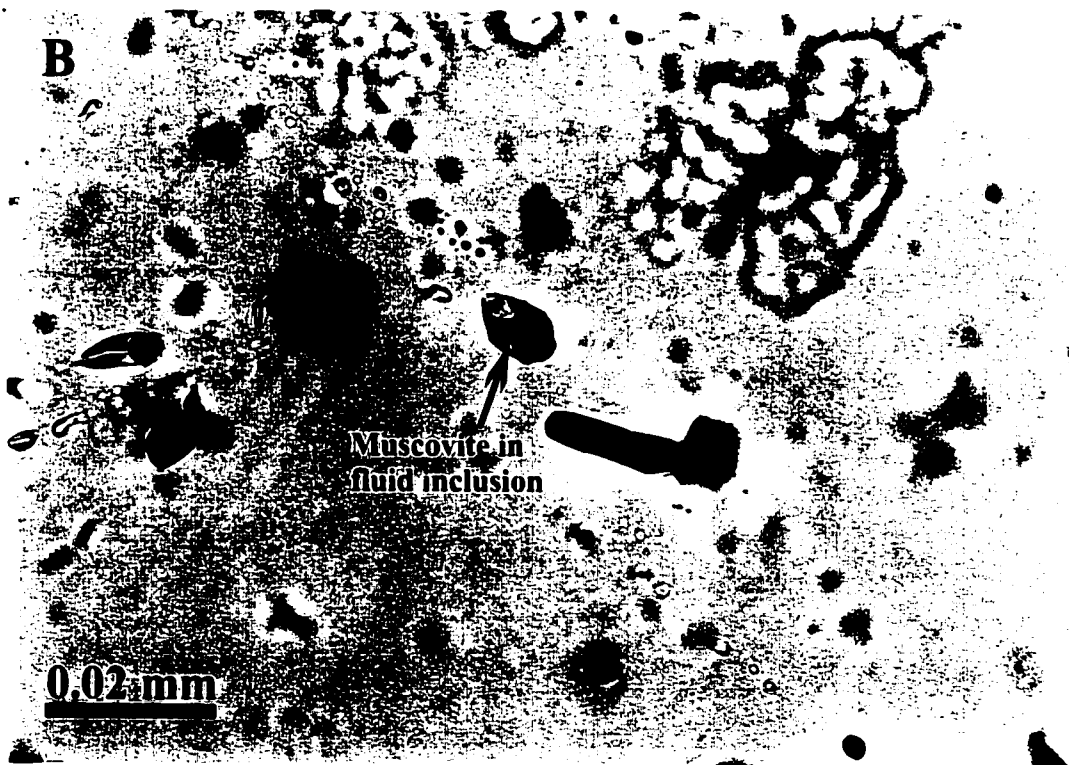
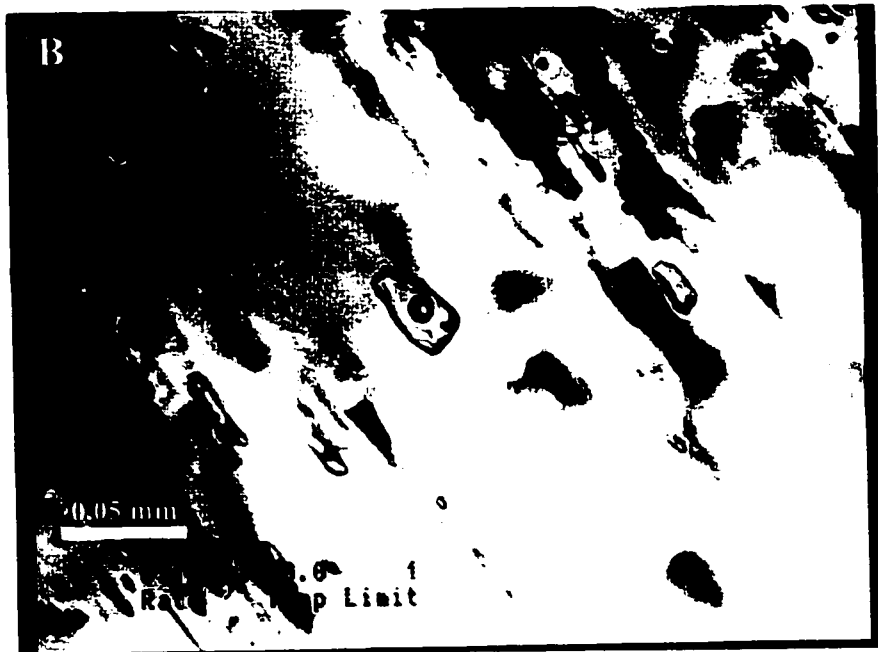




**Plate 5.4.** Ice melt in Type 1A fluid inclusions. Pictures **A** and **B** constrain the temperature of final ice melting for fluid inclusions trapped within a growth band to between  $-0.2$  and  $0.0^{\circ}\text{C}$ , indicating that the Type 1A fluids have trace to no salinity. The ice crystal has a negative relief relative to the inclusion's liquid phase.



semi-quantitatively by SEM analysis (Plate 5.5). The muscovite and dawsonite crystals are interpreted to have been heterogeneously trapped (i.e. pseudodaughters), as the dawsonite is present in about 20% of the Type 1B fluid inclusions, while muscovite pseudodaughters were identified in <10%.

Microthermometric measurements indicated that the Type 1B fluids undergo final ice melting from -0.2°C to 0.0°C. In some fluid inclusions a clathrate phase was observed to melt at approximately +9.5 °C, indicating the presence of small amounts of CO<sub>2</sub> in the fluid (consistent with the presence of dawsonite in some fluid inclusions). The Type B fluid inclusions homogenize to the liquid phase typically between 150 and 220°C (Table 5.1; Figure 5.1).

### ***Type 1C fluid inclusions***

Type 1C fluid inclusions are found in intimate association with some of the Type 1A fluid inclusions. These inclusions were recorded to have lengths up to 40 μm, and are vapor-rich (Plate 5.6).

### ***Discussion***

Type 1A fluid inclusions from the Fluorite Zone sample homogenize between temperatures of 155°C and 176°C and are in association with Type 1C fluid inclusions, and therefore are interpreted to have undergone boiling (Bodnar *et al.*, 1985).

The differences between Types 1A and 1B fluid inclusions is observed in the composition of the pseudodaughter minerals trapped in each fluid subtype, the

**Plate 5.5.** Pseudodaughter minerals (dawsonite and muscovite) in association with the Type 1B fluid inclusions (sample ST-12-6). The pseudodaughter minerals muscovite and dawsonite were identified in a thermally decrepitated Type 1B fluid inclusion as indicated by a scanning electron microscope pictures **A** and **B**. **(C)** An orthorhombic dawsonite ( $\text{NaAl}(\text{CO}_3)(\text{OH})_2$ ) pseudodaughter mineral is present in a three-phase (L:V:S) Type 1B fluid inclusion of dimensions 57.5  $\mu\text{m}$  by 37.5  $\mu\text{m}$ . Final ice melt was observed within error of 0.0°C, and the inclusion homogenized at 227°C. Some neighboring fluid inclusions underwent final phase melting as high as +9.5°C. This final phase change above zero may be explained by the melting of a clathrate phase, a compound consisting of a lattice of water molecules bound to gas molecules such as  $\text{CO}_2$ .

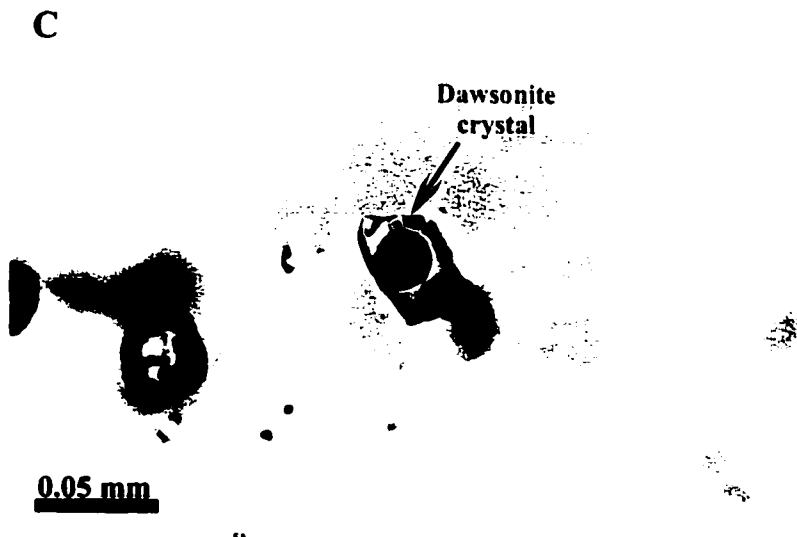
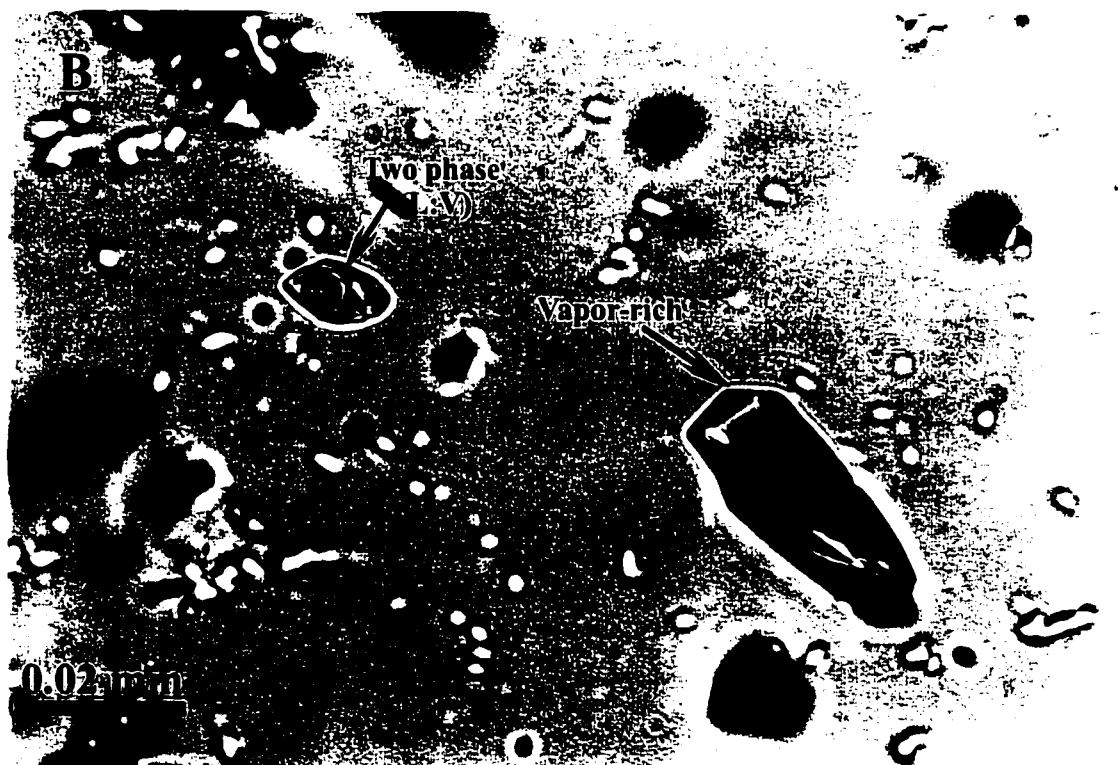
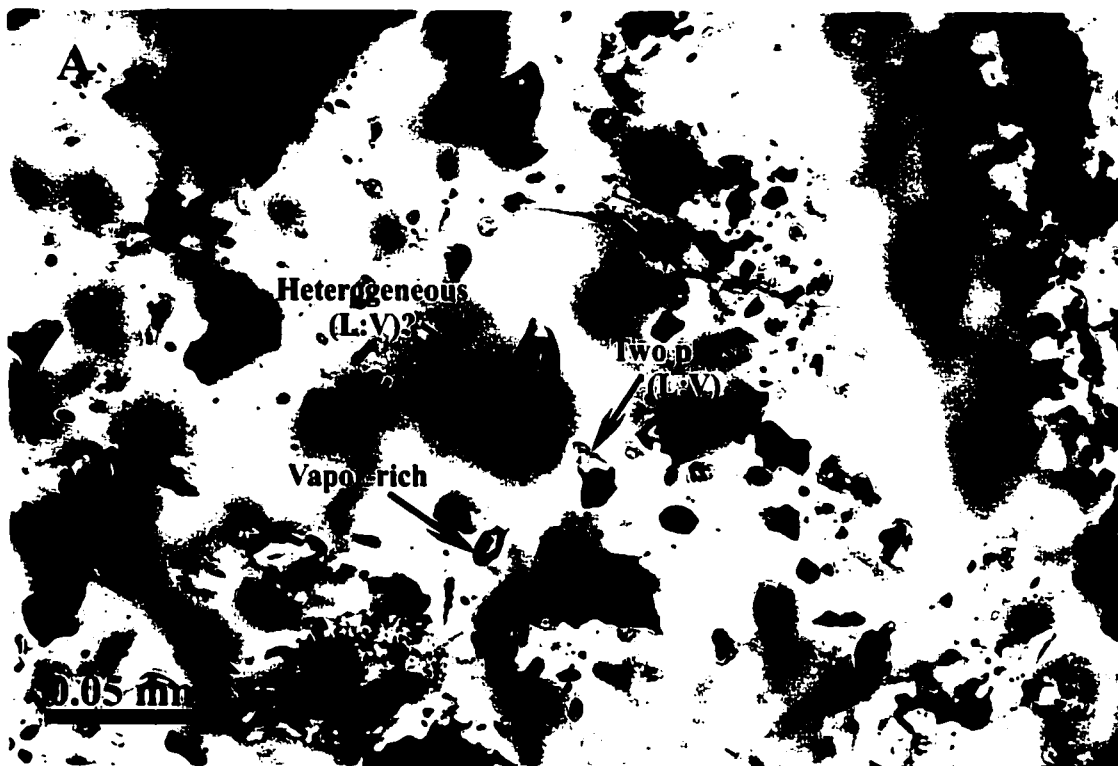


**Plate 5.6.** Type 1C fluid inclusions in association with Type 1A fluid inclusions (Fluorite zone). Picture A shows vapor-rich (Type 1C) and two-phase (V:L) fluid inclusions, in association with a heterogeneously trapped (or necked?) fluid inclusion. Picture B also shows the association between Type 1A and Type 1C fluid inclusions; a textural indication of boiling in the system.



presence of minor amounts of CO<sub>2</sub> in the Type 1B fluid inclusions, and the association to Type 1C fluid inclusions. Type 1B fluids may not have undergone an event of fluid boiling (devolatilization of CO<sub>2</sub> from the fluid has not occurred), whereas Type 1A fluids may have had their volatile content depleted by boiling. In summary, Type 1A and 1B may represent a fluid trapping continuum rather than two distinctly different fluid subtypes. Furthermore, as some of the Type 1A fluids are preserved in growth bands that show boiling, the measured homogenization temperatures of the fluid represents the temperature at which the fluid was trapped, and therefore no pressure correction is necessary. Some of the inclusions that yield homogenization temperatures >200°C may represent fluid inclusions that were necked (Table 5.1; Bodnar *et al.*, 1985).

### ***Type 2 Saline Fluid Inclusions***

The saline Type 2 fluid population was studied by non-destructive and destructive methods. Non-destructive microthermometric analysis of the Type 2 fluid inclusions provided information on salinity and composition from the melting behavior of the mixed salt-hydrate systems, and the minimum temperatures of fluid trapping. The melting behavior of the inclusions enabled general classification of the fluid inclusion compositions based on eutectic phase reaction temperatures, estimation of the total salinity of the fluids, as well as the relative composition of NaCl to CaCl<sub>2</sub>. Analysis of fluid inclusion decrepitation residues by electron microprobe provided qualitative identification of the major solutes.

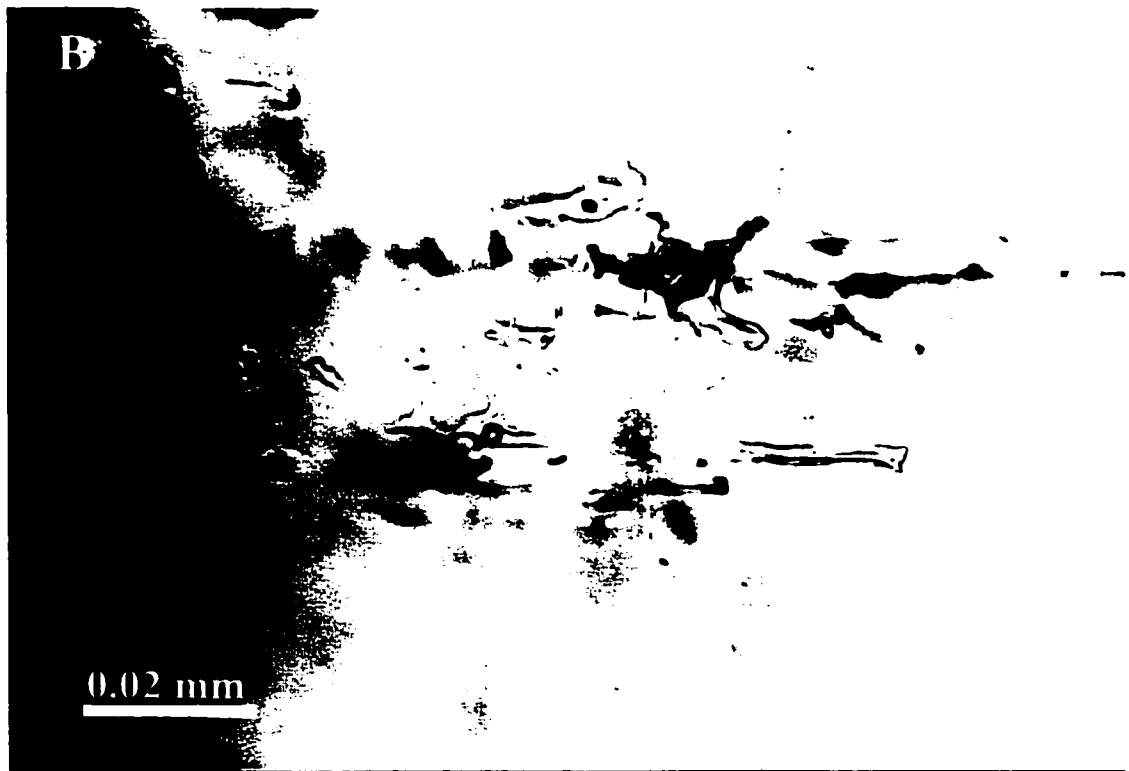
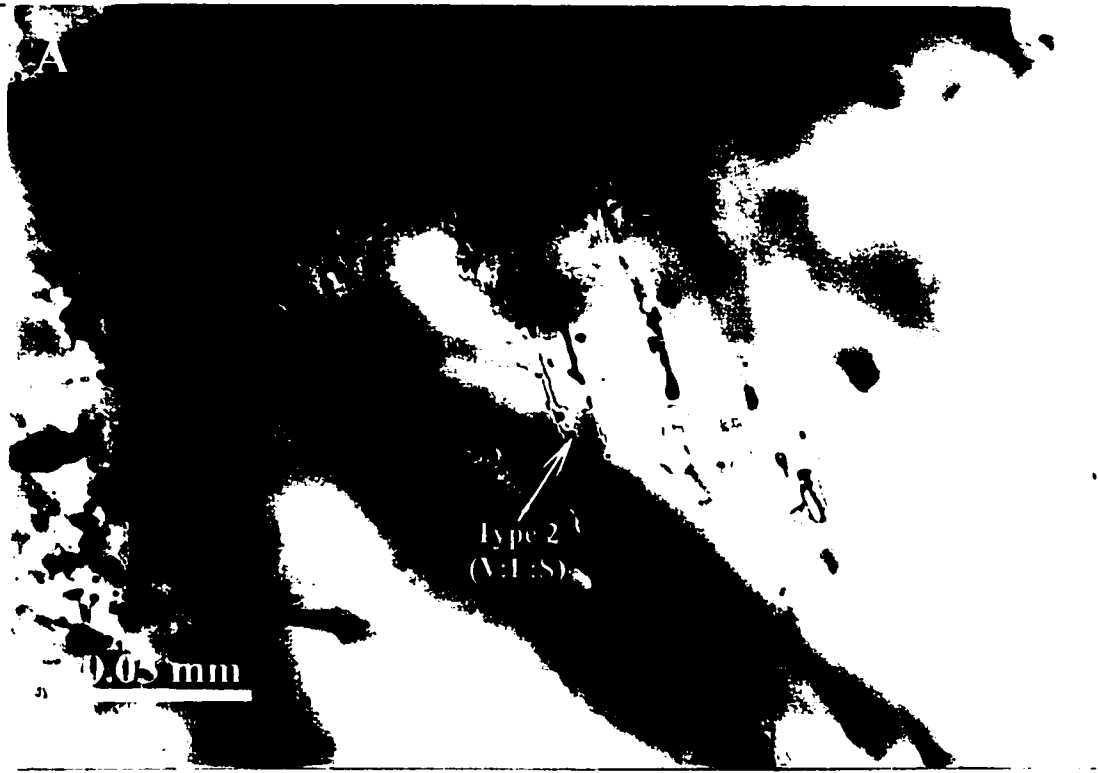


The Type 2 fluid population is spatially widespread and abundant, frequently trapped as irregular-shaped primary fluid inclusions along growth bands (Plate 5.7). This fluid type is characterized by three-phase (V:L:S) and two-phase (V:L) inclusions that are up to 80  $\mu\text{m}$  in length. Typically, the Type 2 fluid inclusions have a volumetric proportion of liquid to vapor around 95% (Table 5.1). The solid phase in the three-phase (V:L:S) inclusions was determined optically to be NaCl salt (Plate 5.7A).

***Non-destructive analysis: Melting behavior in mixed salt systems***

Both stable and metastable  $\text{CaCl}_2$ -hydrates can have a dramatic effect on the melting behavior of fluids. Under stable conditions the NaCl- $\text{CaCl}_2$ - $\text{H}_2\text{O}$  system can be distinguished from the NaCl- $\text{MgCl}_2$ - $\text{H}_2\text{O}$  system on the basis of eutectic temperature:  $-52^\circ\text{C}$  for mixed salt systems containing  $\text{CaCl}_2$ -hydrates, and  $-35^\circ\text{C}$  for systems containing  $\text{MgCl}_2$ -hydrates (Davis *et al.*, 1990; Oakes *et al.*, 1992). Davis *et al.* (1990) conducted melting experiments on synthetically grown fluid inclusions in the NaCl- $\text{MgCl}_2$ - $\text{H}_2\text{O}$  and NaCl- $\text{CaCl}_2$ - $\text{H}_2\text{O}$  ternary systems to observe the melting behavior of fluids containing metastable salt-hydrates such as  $\text{MgCl}_2 \cdot 6\text{H}_2\text{O}$ ,  $\text{MgCl}_2 \cdot 8\text{H}_2\text{O}$ , and  $\text{CaCl}_2 \cdot 4\text{H}_2\text{O}$ . This study concluded that eutectic temperatures occur as low as  $-80^\circ\text{C}$ . Davis *et al.* (1990), Spencer and Lowenstein (1992), and Brown (1998) mention that serious problems exist in distinguishing the NaCl- $\text{CaCl}_2$ - $\text{H}_2\text{O}$  and NaCl- $\text{MgCl}_2$ - $\text{H}_2\text{O}$  systems under metastable fluid conditions. Destructive analytical techniques are a useful tool in constraining the composition of fluid that is trapped under metastable conditions. In the case of the saline vein fluids in the Mallery Lake

**Plate 5.7.** Type 2 fluid inclusions (Sample 14257). Three-phase (L:V:S) and two-phase (L:V) Type 2 fluid inclusions form dendritic trails extending from a primary growth band (pictures **A** and **B**). Monophase liquid fluid inclusions do exist (see picture **B**), indicating that fluid inclusion necking occurred. The irregular shape of the Type 2 fluid inclusion in pictures **A** and **B** indicate that they were formed under low temperature conditions.



area, destructive analysis of the fluid inclusions proved that the NaCl-CaCl<sub>2</sub>-H<sub>2</sub>O ternary system is dominant. In the light of this information, the rest of the discussion will focus on the melting behavior of the NaCl-CaCl<sub>2</sub>-H<sub>2</sub>O ternary system.

***A) Stable CaCl<sub>2</sub>-hydrate melting behavior***

The following discussion of the stable CaCl<sub>2</sub>-hydrate melting behavior in the NaCl-CaCl<sub>2</sub>-H<sub>2</sub>O system is adapted from work conducted by Davis *et al.* (1990) on synthetic fluid inclusions. It was recorded that stable CaCl<sub>2</sub>-hydrate melting behavior occurs in systems that contain low concentrations of CaCl<sub>2</sub>. The first observed phase change occurred between -53°C and -47°C, recording the stable eutectic reaction of halite, ice, and antarcticite (CaCl<sub>2</sub>•6H<sub>2</sub>O). At -45°C, the fluid inclusions adopted a coarse and granular appearance as hydrohalite recrystallized. Ice melting of the crystals occurred between -35°C and -23°C. The low temperature disappearance of ice may result from a fluid compositional shift that occurred as a result of the recrystallization of hydrohalite on the fluid inclusion walls. Final hydrohalite melting occurred between -5°C and -0.0°C.

***B) Metastable CaCl<sub>2</sub>-hydrate melting behavior***

As well as recording the features of the stable CaCl<sub>2</sub>-hydrate melting behavior, Davis *et al.* (1990) also recorded the behavior of those inclusions that contain metastable CaCl<sub>2</sub>-hydrates. Fluid inclusions that contain metastable CaCl<sub>2</sub>-hydrates have depressed eutectic temperatures relative to inclusions that undergo stable CaCl<sub>2</sub>-hydrate melting. The depressed temperatures may be due to the system containing ice,

halite, and  $\text{CaCl}_2 \cdot n\text{H}_2\text{O}$  (typically as a  $\text{CaCl}_2 \cdot 4\text{H}_2\text{O}$  complex). Goldstein and Reynolds (1994) described a fluid inclusion that passes through the depressed eutectic temperature, resulting in the breakdown of the  $\text{CaCl}_2$ -hydrate, as developing an “orange peel” texture. Typically, this transition through the metastable eutectic point occurs over a temperature range of  $-90^\circ\text{C}$  to  $-75^\circ\text{C}$ .

With a slight increase in the temperature (between  $-70^\circ\text{C}$  to  $-50^\circ\text{C}$ ), the inclusion develops a granular appearance to the fluid inclusion as the  $\text{CaCl}_2 \cdot n\text{H}_2\text{O}$  complex is destroyed, and the subsequent recrystallization of ice occurs. Although not observed, Davis *et al.* (1990) predicted that halite dissolution should also occur over this temperature range.

Davis *et al.* (1990) noted that inclusions that contain moderate concentrations of  $\text{CaCl}_2$  go through a stable  $\text{CaCl}_2$ -hydrate eutectic reaction between  $-56^\circ\text{C}$  and  $-50^\circ\text{C}$  (breakdown of antarcticite). Darkening of hydrohalite rims and the development of ice crystals characterized this transition. A final ice-melting event typically occurs between  $-50^\circ\text{C}$  and  $-35^\circ\text{C}$  (light purple arrows; Figure 5.2). If the inclusions contain greater than 2.9 m  $\text{CaCl}_2$  this ice-melting event is the last phase observed. For inclusions that contain less than 2.9m  $\text{CaCl}_2$ , the aqueous fluid reacts with  $\text{NaCl}$  to form hydrohalite crystals. In this case, the fluids may continue travelling along the hydrohalite-ice cotectic (yellow arrow; Figure 5.2), with final hydrohalite melting as high as  $-1^\circ\text{C}$  (dependant on the wt. fraction of  $\text{NaCl}/\text{NaCl}+\text{CaCl}_2$ ; light green area; Figure 5.2). There are cases though where the presence of hydrohalite persists as high as  $+25^\circ\text{C}$ , even under heating rates as low as  $0.1^\circ\text{C}/\text{min}$  (Oakes *et al.*, 1992).

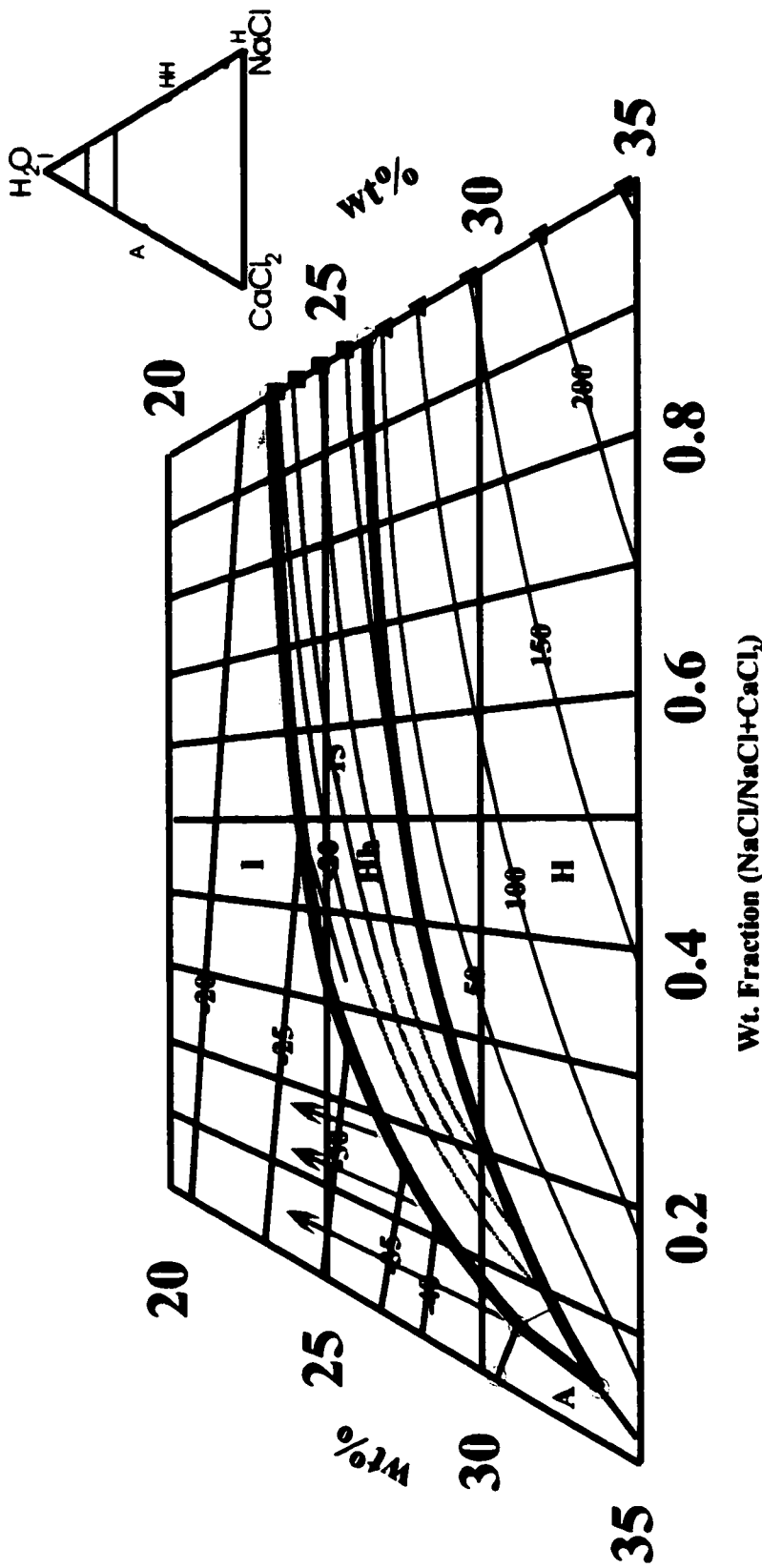


**Figure 5.2. Melt behavior of the stable NaCl - CaCl<sub>2</sub> - H<sub>2</sub>O ternary fluid system.** Figure 5.2 is modified from Oakes et al., 1992, and Yanatieva, 1946. Fields are defined as Antarcticite (A), ice (I), hydrohalite (Hh), and halite (H) fields. Dashed lines indicate extrapolation of isotherms in the hydrohalite (Hh) stability field. Light purple arrows indicate that system has moved from the ice-hydrohalite cotectic into the ice field (typically for fluids that have high concentrations of CaCl<sub>2</sub> relative to NaCl). For fluids with lower relative concentrations of CaCl<sub>2</sub> relative to NaCl the fluid reacts with the NaCl to form hydrohalite and subsequently moves along the ice-hydrohalite cotectic as indicated by the yellow arrow. After final ice melting occurs, the stability of the system shifts from the ice-hydrohalite cotectic into the hydrohalite field (light green box).

### ***Behavior of the mixed salt-hydrates of the Type 2 fluids***

Type 2 fluid inclusions display eutectic melting events over a range from -50°C to -90°C. These eutectic temperatures suggest the presence of CaCl<sub>2</sub> plus other salts. The temperature range from -50°C to -90°C indicates that the Type 2 fluid underwent both stable and metastable salt-hydrate reactions in the NaCl-CaCl<sub>2</sub>-H<sub>2</sub>O fluid ternary system. Thermal decrepitation of the Type 2 fluid inclusions, and the subsequent qualitative analysis of the salt piles by the EDS electron microprobe indicated high concentrations of calcium and sodium in the decrepitation residues, with no detection of magnesium or potassium. The Type 2 fluids are therefore confirming both non-destructively and destructively to conform to the NaCl-CaCl<sub>2</sub>-H<sub>2</sub>O ternary system.

### **Results**

It was critical during microthermometric analysis of the Type 2 fluids to not only record accurate temperatures for each phase melt, but also to determine the composition of the final melt phase (hydrohalite (Hh) from ice). After determination of the final melt phase, the data were plotted on the NaCl-CaCl<sub>2</sub>-H<sub>2</sub>O ternary fluid diagram. Two different melting behaviors were recognized for the Type 2 fluids: (1) inclusions that underwent final melting between -52°C and -26°C (Group 1; Figure 5.3); and (2) inclusions that underwent final melting as low as -3.4°C (Group 2; Figure 5.3). No distinction between the two fluid groups can be made based on the temperature of fluid homogenization, as the homogenization temperatures typically range between 90°C and 150°C (Table 5.1; Figure 5.1).

Textural and microthermometric studies of the Type 1 fluids (sample Fluorite Zone) indicate that boiling occurred between 155°C and 176°C, and therefore the fluids were trapped at pressures ~ 10 bars by using a conventional pressure-temperature diagram for water. As Type 2 fluid inclusions homogenized between 90°C and 150°C (Table 5.1) a maximum pressure correction of only 10 bars needs to be applied corresponding to a maximum correction of about 5°C for the homogenization temperature to be equivalent to the temperature of actual fluid trapping.

### ***Discussion***

Petrographically, the composition of the final melt phase for the Group 1 inclusions was revealed as ice. The composition of the final melt phase for Group 1 fluid inclusions was determined by comparing the relief of the melt phase relative to the hosting solution by use of the Becki line test (Vanko *et al.*, 1988). This test confirmed that the final melt phase was ice. Low temperature melting of hydrohalite was not observed however, making it difficult to constrain the melting behavior in the NaCl-CaCl<sub>2</sub>-H<sub>2</sub>O ternary system. Two models are proposed to explain the observed phase recrystallization and melting behaviors: (1) direct melting of ice in the ice stability field from the -52°C stable eutectic point (red line; Figure 5.3), and/or (2) progressive melting of hydrohalite along the Hh-ice cotectic, unobserved departure from the cotectic as Hh melts, and final ice melting at temperatures between -49°C and -26°C either on the ice-Hh cotectic or some undetermined point in the ice field (green arrows; Figure 5.3).



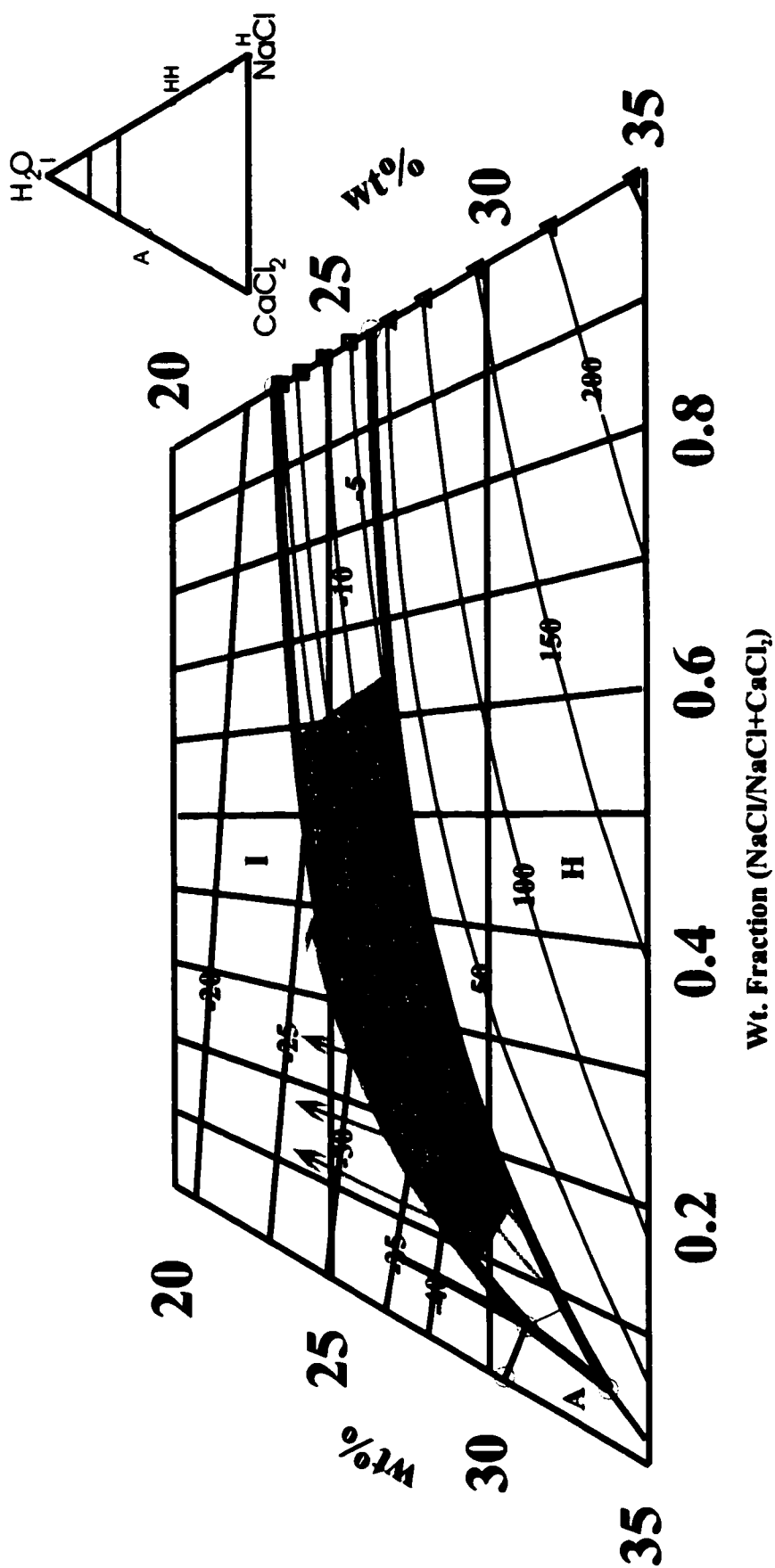
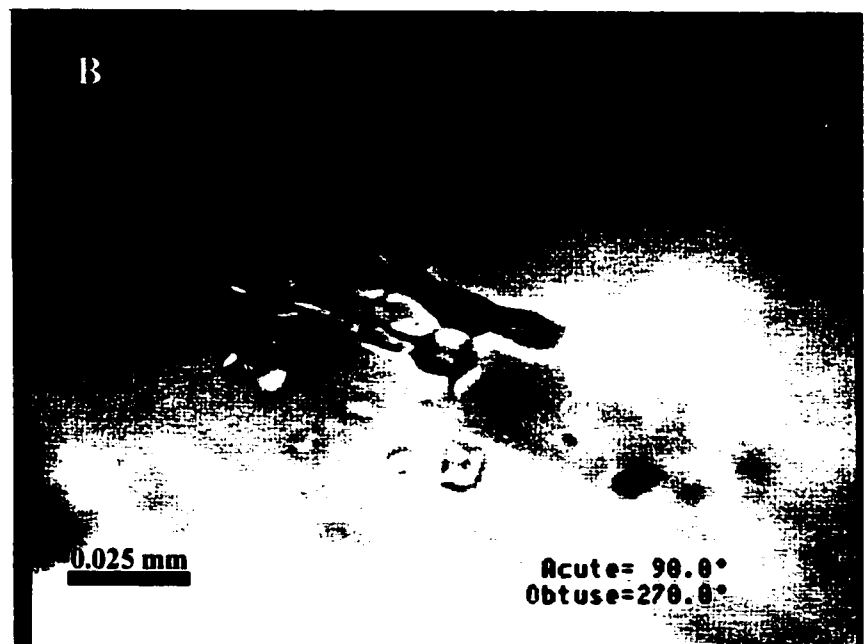


**Figure 5.3. Hydrohalite stability field for Type 2 fluids.** Antarcticite (A), ice (I), hydrohalite (Hh), and halite (H) fields in the stable NaCl - CaCl<sub>2</sub> - H<sub>2</sub>O ternary fluid system. Figure 5.1 is modified from Oakes et al., 1992, and Yanatieva, 1946. Dashed lines indicate extrapolation of isotherms in the hydrohalite (Hh) stability field. Red line and green arrow represent the observed phase recrystallization and melting behaviors of the Group 1 fluids. Melting behavior of the Group 2 fluids is constrained by the blue box.

Group 2 inclusions are characterized by going through an ice melting and recrystallization event that started at  $-40^{\circ}\text{C}$ , and final Hh melt phase that ended at  $-3.4^{\circ}\text{C}$  (Table 5.1; Figure 5.3). The composition of the final melt phase was determined by the crystal shape, as well as the relief of the crystal relative to the aqueous liquid (Touret, 1995). Using these tests, the composition of the final melt phase was determined to be hydrohalite (Plate 5.8). This conclusion allows for the total weight percent, and relative composition of the salt to be determined. The cluster of compositions of the final melt phase of hydrohalite indicates a greater relative abundance of NaCl in the system relative to  $\text{CaCl}_2$  (blue box; Figure 5.3). Interpretation of this inclusion type is further complicated by the phenomenon of hydrohalite metastability. If hydrohalite responds in a stable manner, the final temperature of the hydrohalite melt can be used to determine the salt weight percentage and relative composition. However, if hydrohalite responds metastably (i.e. melting at temperatures above zero), it is not possible to determine the fluid composition due to a current lack of knowledge about the systematics of the metastable hydrohalite field.

Figure 5.3 indicates that the Type 2 fluids range in total salinities from 23 wt. % to 31 wt. %, and vary in  $(\text{NaCl}/\text{CaCl}_2 + \text{NaCl})$  wt. fractions from 0.05 to 0.55. Although there is evidence of some of the inclusions having higher NaCl relative to  $\text{CaCl}_2$  this is the exception, as the majority of the fluids do contain an elevated weight fraction of  $\text{CaCl}_2$  salt relative to NaCl salt.

**Plate 5.8.** Hydrohalite in the Type 2 fluid inclusions (Sample 14257). Rapid cooling just before final hydrohalite melt formed the idiomorphic hydrohalite crystal (**A**). The Becki Line method of identification was used to further identify the crystal as hydrohalite (Hh). This method states that as the stage is lowered, the Becki Line will move into the substance with the highest index of refraction. In this case, the hydrohalite crystal has a higher refractive index than the enclosing solution, and therefore the Becki Line moves into the hydrohalite crystal (**B**). The opposite result is seen in the movement of the Becki Line between the inclusions' solution at the inclusion wall and the enclosing quartz. In this case the Becki Line moves into the quartz, indicating that the solution has a lower refractive index than the quartz (< 1.54 refractive index).



## **Association of fluid inclusion types with precious metal deposition**

Microthermometric analysis was conducted on three precious metal-bearing vein samples (703527, 703534, and 703530) in an attempt to tie precious metals to a fluid source. Two methods were used to relate metal deposition to the source fluids: (1) microthermometric analysis of fluid inclusions that are in intimate association with precipitated metals; and (2) semi-quantitative EDS microprobe analysis of fluid inclusion decrepitation residues. As discussed in Chapter 3, precious metals were linked to two different events: (1) an early stage of precious metal deposition that occurred during the deposition of primary silica; and (2) a later event of precious metal deposition that is associated with cross-cutting, quartz-hematite veins.

Primary silica was determined to be associated with the deposition of precious metals in Samples 703527 and 703534. Microthermometric analysis of Sample 703527 indicated the presence of both Type 1 and Type 2 fluids (Table 5.1). EDS semi-quantitative microprobe analysis of a decrepitation residue, from a Type 2 fluid inclusion from Sample 703527, indicated an intimate association between silver and trace amounts of Ca, Cl, S, Al, Te, and Fe.

Further association between the transport of precious metals and the Type 2 fluids was determined for Sample 703534 by microthermometric and semi-quantitative EDS microprobe analysis. Microthermometric analysis indicated that the Type 2 fluids have a wide range in salinities from 23 to 31 wt. %  $\text{CaCl}_2\text{-NaCl}$ , and homogenize between 90°C and 150°C (Table 5.1). EDS microprobe analysis indicated an association between iron oxides and Ag-, Au-, Cu-salts in decrepitation

residues of this sample, suggesting that the type 2 fluids transported precious metals (Figure 5.4).

The later stage of precious metal-bearing quartz-hematite veins in Sample 703530 was analysed by fluid inclusion microthermometry and semi-quantitative EDS microprobe analysis of electrum grains associated with hematite. The primary fluid inclusions analysed from these later quartz-hematite veins range in salinity from 28 to 31 wt. %  $\text{CaCl}_2\text{-NaCl}$  and undergo homogenization between  $70^\circ\text{C}$  and  $125^\circ\text{C}$  (Table 5.1), and thus are characterized as Type 2 fluids. No Type 1 fluid inclusions were encountered during this later vein stage, suggesting that Type 2 fluids were responsible for the deposition of electrum and argentite during this later event.

Figure 5.4. Precious metal association in sample Chal 703534

Element Weight Percent

	Na	Mg	Si	Cl	K	Ca	S	Co	Ag	Au	M	Pt
1	0.0	0.0	24.5	2.6	0.3	6.1	0.1	4.8	7.1	0.0	54.0	0.5
2	0.0	0.0	15.1	1.1	0.0	2.3	0.0	12.6	5.8	13.7	49.2	0.2
3	0.0	0.0	5.8	0.0	0.1	0.5	0.0	0.8	2.6	0.0	81.0	0.1
4	0.1	0.4	50.0	10.9	0.0	19.8	0.8	0.5	10.8	0.0	6.7	0.0
5	0.0	0.1	12.8	0.6	0.0	2.0	0.0	19.0	4.4	6.3	54.7	0.0
6	0.0	0.0	21.9	1.3	0.0	3.2	0.0	0.7	24.4	49.5	0.0	0.0
7	0.2	0.0	13.1	1.4	0.0	2.9	0.1	5.4	9.9	1.2	65.4	0.3
8	0.2	0.3	38.9	10.1	0.0	22.2	0.1	0.0	24.5	0.0	3.2	0.7
9	0.5	0.2	14.9	2.5	0.0	3.9	0.1	0.3	75.3	0.0	3.2	0.3
10	0.3	0.1	15.7	3.8	0.0	7.5	0.5	0.0	69.8	0.0	1.9	0.1
11	0.5	0.3	30.9	7.5	0.3	13.6	0.5	0.0	40.3	1.4	4.3	0.6
12	0.2	0.3	8.2	2.7	0.0	3.5	0.0	0.0	83.2	0.3	2.4	0.1
13	0.2	0.0	45.6	11.0	0.0	15.4	1.4	0.0	22.4	0.0	2.6	1.1
14	1.2	0.3	54.6	8.7	0.0	16.1	0.1	0.0	16.0	1.4	0.8	0.5
15	0.5	0.7	10.7	3.5	0.0	5.0	0.0	0.1	77.1	0.3	2.0	0.0
16	1.9	1.3	3.1	12.6	0.0	10.0	0.3	0.0	64.6	0.0	5.2	0.0

Results attained via semi-quantitative back-scatter electron EDS microprobe analysis. All samples normalized to 100.0.



## CHAPTER 6

### STABLE ISOTOPE ANALYSIS OF HYDROTHERMAL VEINS IN THE MALLERY LAKE AREA

#### Introduction

Minerals and trapped fluids were extracted from veins in the Mallery Lake epithermal system and analysed isotopically with the following objectives: (1) to obtain oxygen isotopic ( $\delta^{18}\text{O}$ ) signatures of precious metal-bearing and barren silica veins, and to address any isotopic differences between the various veins at a regional scale; (2) to estimate the  $\delta^{18}\text{O}$  and  $\delta\text{D}$  signatures of the primary trapped fluids; and (3) to use these values to constrain the primary fluid involved in vein deposition.

#### Stable Isotope Systematics and Errors

##### *Expression of Isotope Ratios*

Analytical values for stable isotopes are reported as a delta ( $\delta$ ) value relative to a standard. Delta values are expressed in per mil units (‰). The delta notation is defined as:

$$\delta^{18}\text{O}(\text{‰}) = \left[ \frac{{}^{18}\text{O}/{}^{16}\text{O}_{(\text{sample})} - {}^{18}\text{O}/{}^{16}\text{O}_{(\text{standard})}}{{}^{18}\text{O}/{}^{16}\text{O}_{(\text{standard})}} \right] \times 10^3$$

Standards for oxygen and hydrogen isotope analyses are expressed relative to VSMOW (Vienna Standard Mean Ocean Water). VSMOW, a standard that replicates the original SMOW value, is a water sample with an isotopic composition similar to that of mid- Atlantic Ocean water. The VSMOW standard  $\delta^{18}\text{O}$  and  $\delta\text{D}$  values are 0.00‰ by definition (Coplen *et al.*, 1983). In practice,



VSMOW is not actually used in the lab. Lab samples are calibrated using the NBS-28 (quartz sand)  $\delta^{18}\text{O}$  standard, which has a value of 9.60‰ relative to VSMOW. Analytical precision for oxygen isotopes is typically  $\pm 0.2\text{‰}$  ( $2\sigma$ ; pers. comm. K. Muehlenbachs, 1999). Hydrogen isotope results are also calibrated against the standard VSMOW (0.0‰). Analytical uncertainty for hydrogen isotope measurements is typically  $\pm 3\text{‰}$  ( $2\sigma$ ; pers. comm. K. Muehlenbachs, 1999).

### ***Isotope Fractionation***

Isotopes of an element are defined as atomic nuclei that have the same number of protons but differ in the number of neutrons, and therefore have different atomic masses. Isotope fractionation occurs as a result of variation in the chemical bond strength due to slight differences in the masses of the isotopes. Heavier isotopes form stronger bonds, and have a higher threshold to withstand disruptive vibrational motion than lighter isotopes, and thus undergo less fractionation (Brownlow, 1996).

At low temperatures, the fractionation of isotopes between minerals and fluid is large. With increasing temperature, however, the relative energy differences between each isotope decreases, resulting in the fractionation of heavy and light isotopes to be smaller according to the following general equation:

$$\delta^{18}\text{O}_x - \delta^{18}\text{O}_y \approx 10^3 \ln \alpha_{xy} = A_{xy} (10^6/T^2) + B_{xy}$$

where  $\alpha$  is defined as the isotopic fractionation factor, T is the absolute temperature in Kelvin, and  $A_{xy}$  and  $B_{xy}$  are constants unique to the x and y phase pair (O'Neil, 1986).

For example, Clayton *et al.* (1972) established the following relationship for the fractionation of oxygen between quartz and water in the temperature range of 200 - 500 °C:

$$\delta^{18}\text{O}_{\text{qtz}} - \delta^{18}\text{O}_{\text{water}} \approx 10^3 \ln \alpha_{\text{qtz} \cdot \text{water}} = 3.38(10^6/T^2) - 3.4$$

In addition to isotopic variations caused by temperature fluctuations, the solute composition of a fluid can also affect isotopic fractionation. The influence of dissolved salt ions on the structure of water molecules alters their vibrational properties, thus causing variations in oxygen and hydrogen fractionation (Kyser, 1987). This effect is of much smaller magnitude than the effects of temperature on fractionation, however.

### **Sample Selection**

Samples were selected from all vein types in the Mallery Lake area, ranging from euhedral quartz crystals to massive-milky silica (Table 6.1). During preparation of the vein samples, attempts were made to constrain the silica to a specific paragenesis. Nevertheless, fluid inclusion studies indicate that two fluid populations were involved in the formation of most of the veins in the Mallery Lake area (Chapter 5). These studies show that the two fluid populations can occur in separate growth bands within the same sample, on the scale of tens of micrometers. This close spatial association between the two fluid populations makes physical separation of quartz deposited by the different fluids very

**Table 6.1. Oxygen (silica) and Deuterium (fluid inclusion) stable isotope data**

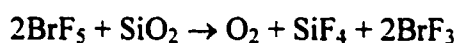
Sample Number	Vein Type	Grade Constraints	$\delta^{18}\text{O}$ quartz (‰)	$\delta\text{D FI}$ (‰)	Vein Description
AT 19-9	A	?	9.8		white silica in association with purple fluorite
14269	A	Barren	8.6	-65	fine milky comb quartz in association with late stage calcite
14267	A	Barren	10.2	-134	fine milky comb quartz
ML 21-5	A	?	8.3		milky brecciated silica associated with purple fluorite
ML 21-9	A	?	10.7		milky comb quartz grown around a purple fluorite fragment
Chal #8a	A	?	11		late stage, cross-cutting, euhedral quartz vein
Chal 1201	A	Barren	9.9		euhedral milky quartz crystals
Chal 1216	A	Barren	8.6		banded microcrystalline silica
703534p	A	?	9.9	-107	fine milky comb quartz
17 vein "112609"	A	?	10.1		milky euhedral comb quartz (late stage)
17 vein "Original"	A	?	10.4		milky-clear euhedral comb quartz (late stage)
17 vein "Black"	A	?	10.6		clear microcrystalline quartz
Dan #2 (Zone #3)	A	Barren	9.9		clear euhedral quartz
14290	A	Barren	10.1	-68	coarse milky comb quartz
AT 10-13	A	Barren	9.5		clear comb quartz terminations
ST-12-6	A	Barren	8.3		clear comb quartz terminations
ST-26-2	A	Barren	8.6		clear coarse comb quartz
AT 20-K	A	?	10.7		microcrystalline silica intercalated with white and purple fluorite
AT 20-J	A	?	11		euhedral white comb quartz with late stage purple fluorite
Fluorite Zn	A	Barren	11.4		milky-clear euhedral comb quartz (late stage)
Chal 1207	A	Barren	11.5		white silica flooding around brecciated fluorite fragments
AT 20-M	A	?	13.7		microcrystalline comb quartz intercalated with white and purple fluorite
14278	A	Barren	13.6	-56	medium comb quartz
14282	A	Barren	12.9		amorphous silica fining into microcrystalline comb quartz
ST-28-2	A	Barren	12.9	-100	medium comb quartz
AT 7-1	A	Barren	11.2		euhedral comb quartz
AT 6-1	A	Barren	14.5		euhedral milky comb quartz
AT 7-4	A	Barren	13.2		euhedral transparent comb quartz
AT 8-2	A	Barren	12.6		euhedral milky comb quartz
703534s	A	?	12.5	-134	milky silica
Chal #5	B	Auriferous	13.9		brecciated silica fragment
Chal #6	B	Auriferous	13.6		silica flooding between breccia
Chal #7	B	Auriferous	12.6		chalcedony vein
Chal #8a	B	Auriferous	12.3		milky microcrystalline silica
Chal #10	B	Auriferous	12.5		chalcedony vein
Chal 1104	B	Auriferous	13.5		chalcedonic silica associated with hematite stringers
703518	B	Auriferous	13.4		chalcedony vein
703524	B	Auriferous	12	-85	chalcedony vein
703527	B	Auriferous	13.8	-119	chalcedony vein
703530	B	Auriferous	13.7	-114	milky brecciated silica crosscut by quartz-hematite veins

difficult. It is therefore likely that the reported  $\delta^{18}\text{O}$  and  $\delta\text{D}$  values reflect mixtures of these two fluids. Furthermore, several of the silica samples analysed for stable isotope values contain very small fluid inclusions that are not suitable for microthermometric analysis. The temperature of deposition of these samples is therefore unknown, making it impossible to calculate  $\delta^{18}\text{O}$  water values.

### **Analytical Procedure**

Forty silica vein samples from the Mallery Lake area were selected for  $\delta^{18}\text{O}$  isotopic analysis. Samples were trimmed with a fine rock saw to isolate veins of a specific paragenesis, and then crushed and sieved to between 80 and 120 mesh-size. Sieved samples were treated with hydrochloric acid to remove impurities, and were then washed with distilled water to remove all salts that may have formed by residual precipitation. Liberation of the oxygen from the silica was achieved by reaction in vacuo with  $\text{BrF}_5$ :

600°C



The liberated oxygen was then reacted with graphite to form  $\text{CO}_2(\text{g})$ , which was analysed by an isotope ratio mass spectrometer.

Eleven siliceous vein samples for hydrogen isotope ( $\delta\text{D}$ ) analysis of fluid inclusions were crushed and sieved to between 20 and 80 mesh. Approximately 4g of sample were hand-picked to avoid impurities, washed with aqua regia, and subsequently dried for 24 hours at 150°C. Thermal decrepitation of the fluid inclusions was achieved under vacuum at 1100°C. The water released was

reduced by zinc metal to generate H<sub>2</sub>, which was subsequently analyzed by mass spectrometer.

## Results

Stable isotope results are reported in Table 6.1, and illustrated in Figure 6.1. The stockworks of the Mallery Lake epithermal system display primary (Type A) and secondary (Type B) silica textures according to the classification scheme of Dong *et al.* (1995). Primary silica textures are characterized by massive silica that precipitated on host rocks (either fragments or vein walls) and/or micro- to macro-euhedral quartz. Type A veins frequently contain other minerals such as fluorite, calcite, and adularia, but are barren of precious metals. The Type B veins (associated with precious metals) display recrystallized and replaced textures.

Isotopically, there is a general distinction between the barren Type A veins and precious metal-associated quartz veins of Type B (Figure 6.1). Type A group has a range in  $\delta^{18}\text{O}$  values from 8.3‰ to 14.5‰ and a mean of  $10.9 \pm 1.7\text{‰}$  ( $1\sigma$ ,  $n=30$ ), while Type B silica veins have a range of  $\delta^{18}\text{O}$  values from 12.0‰ to 13.8‰, with a mean of  $13.1 \pm 0.7\text{‰}$  ( $1\sigma$ ,  $n=10$ ).

The hydrogen isotope ratios of waters that were extracted from eleven quartz samples range from  $\delta\text{D} = -56\text{‰}$  to  $-134\text{‰}$  (Table 6.1), and show no particular correlation with vein type.

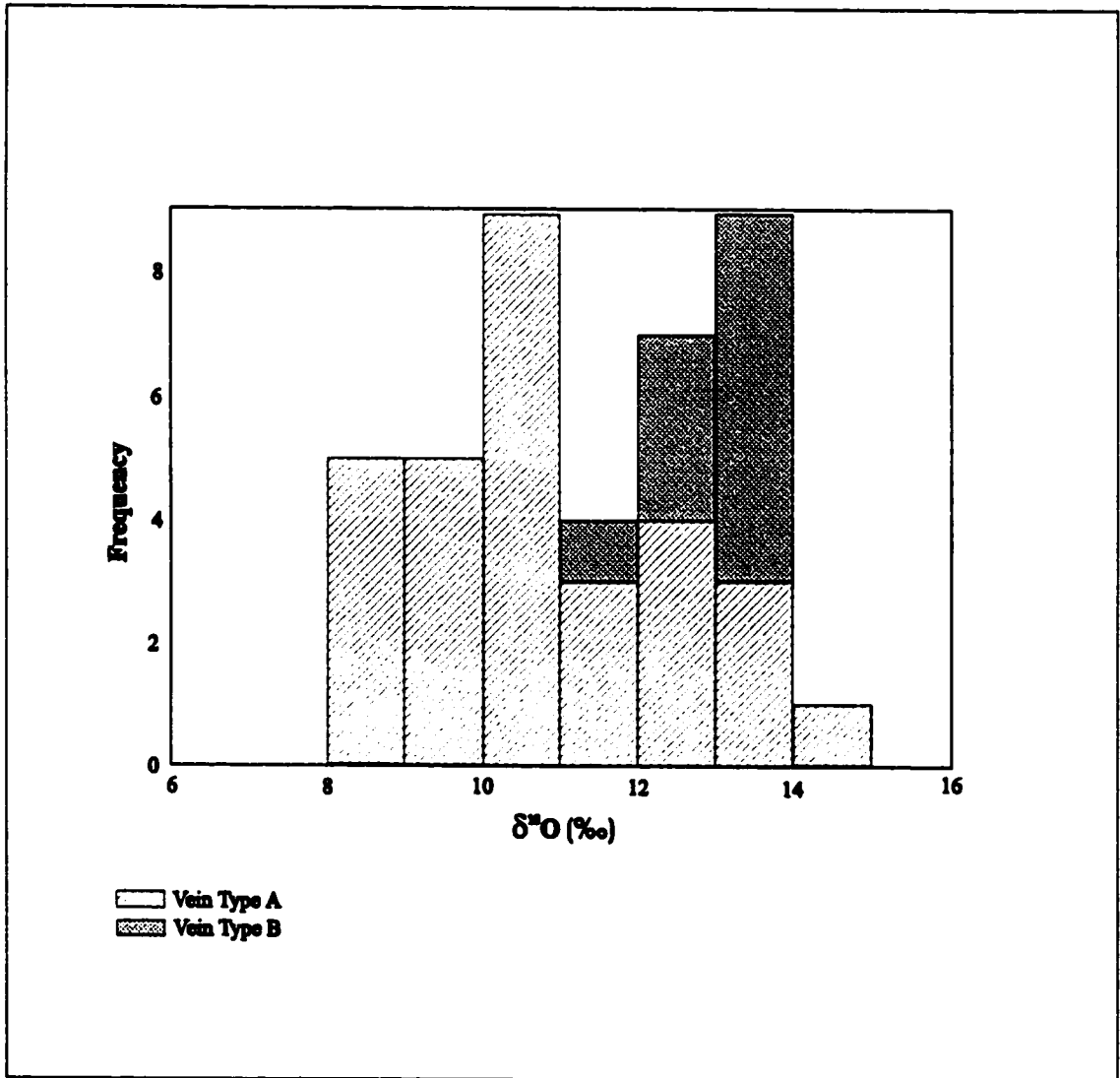


**Figure 6.1.**  $\delta^{18}\text{O}$  isotopic compositions of quartz from the Mallery Lake veins. The veins are split into two major categories (A and B) based on silica textures.

### ***Isotopic composition of the fluid***

It is possible to obtain an estimate of  $\delta^{18}\text{O}$  fluid values by using the average fluid inclusion trapping temperature for a sample to correct for fractionation between the quartz and water (Clayton *et al.*, 1972). However, as noted earlier, most of these samples do not contain a single fluid inclusion population, but typically show evidence for the presence of at least two distinct types of fluid inclusions during quartz deposition. Two possible  $\delta^{18}\text{O}$  fluid values have therefore been calculated using the average trapping temperatures of the different fluid inclusion populations, to provide maximum and minimum estimates. On this basis, if the quartz was dominantly deposited from the high salinity ( $\text{CaCl}_2\text{-NaCl-H}_2\text{O}$ ), low temperature fluid, then the fluid would have a range of  $\delta^{18}\text{O}$  between  $-11.0\text{‰}$  and  $-4.3\text{‰}$ , with a mean of  $-8.0 \pm 2.1\text{‰}$  ( $n=9$ ). Alternatively, if the majority of the quartz was precipitated from the higher temperature, low salinity waters, then a range of  $\delta^{18}\text{O}$  values from  $-5.6\text{‰}$  to  $-2.2\text{‰}$  is indicated, with an average of  $-3.9 \pm 1.7\text{‰}$  ( $n=3$ ). These estimates for  $\delta^{18}\text{O}$  and  $\delta\text{D}$  fluid data are listed in Table 6.2 and plotted in Figure 6.2. The present day meteoric water line (MWL) is also shown in Figure 6.2, and it is believed that the compositions of ancient meteoric waters (1.8 – 1.9 Ga, Kimiwan) differed little from these values (Muehlenbachs *et al.*, 1994).

**Table 6.2**

Average trapping temperatures (Tt) and calculated  $\delta^{18}\text{O}$  water values of two possible fluids that may have been involved in forming the veins in the Mallery Lake area. The  $\delta^{18}\text{O}$  water values are calculated by using the quartz – water fractionation equation of Clayton *et al.* (1972) for the trapped waters, extrapolated below 200 °C for lower temperature fluids.

Sample Number	Vein Type	$\delta\text{D}\text{‰}$ (quartz FI)	$\delta^{18}\text{O}\text{‰}$ (quartz)	High Salinity Fluid Tt (°C ave.)	Possible High Salinity $\delta^{18}\text{O}$ (water)	Low Salinity Fluid Tt (°C ave.)	Possible Low Salinity $\delta^{18}\text{O}$ (water)
14257	A	-134	10.2	99	-11	165	-4.0
ST-26-2	A		8.6	126	-9.2		
ST-12-6	A		8.3			169	-5.6
703534	A	-107	9.9	129	-7.6		
14290	A	-68	10.1	137	-6.6		
17 Vein	A	-104	10.4	113	-8.8		
ST-10-13	A		13.5	81	-10.1		
Fluorite zone	A		11.5			171	-2.2
ST-28-2	A	-100	12.9	133	-4.3		
703527	B	-119	13.8	102	-6.3		
703530	B	-114	13.7	109	-8.2		

## Discussion

A moderate relationship between silica texture and oxygen isotopic composition, and location of vein types A and B can be observed. Close to the Mallery Lake peninsula, the majority of the Type A silica veins range in  $\delta^{18}\text{O}$  values from 8.3 to 11.5‰ (Figure 3.2), whereas west and southeast of the peninsula, Type A veins typically have higher  $\delta^{18}\text{O}$  values, from 12.9 to 13.6‰ (Figure 3.1). Exceptions to these elevated  $\delta^{18}\text{O}$  values, for the Type A veins, with increased distance from the Mallery Lake peninsula, were determined for select veins in the Chalcedonic Stockwork zone and veins from localities ST-12-6 and ST-10-13. Type B veins also have elevated  $\delta^{18}\text{O}$  values, although they are distinct in being characterized by secondary silica textures and high gold grades. The partial overlap of the  $\delta^{18}\text{O}$  values of vein types A and B could be explained by: (1) isotopic disequilibrium between the host rocks and the hydrothermal fluid



as the temperature of the fluid decreases with increasing distance from a putative heat source; and (2) a change in the source of fluid, or variation in the proportions of the two known fluids during vein formation. The feasibility of these two explanations is examined below.

(1) Lower degrees of water/rock interaction as fluid temperatures decrease with increased distance from the heat source: For this explanation to be viable, the extent of host rock alteration should decrease as the distance increases from the assumed heat source. However, there appears to be no regional-scale variation in the alteration of the host rocks, as all stockworks are surrounded by a phyllic halo. Furthermore, the fluid inclusion studies do not indicate any systematic temperature variation that might indicate the location of a central heat source.

(2) Changes in the source fluid or a variation in the proportions of the two known fluid types: As discussed previously, results of microthermometric analysis show a bimodal distribution of salinity and temperature for the fluid inclusions from the Mallery Lake veins. However, the proportion of these two fluids in any given vein cannot be determined for a majority of the stockworks, because much of the silica has been recrystallized. Thus, it is not clear that the Type A and B veins were precipitated dominantly by one fluid type or another. Nevertheless, the bimodality of both the isotopic and fluid inclusion data might be taken to support this interpretation.

The large range in the  $\delta D$  values also suggests that at least two different waters were involved in vein formation. However, the isolation of each fluid inclusion type to distinct growth bands suggests that mixing of these fluid types

did not take place to any significant degree (Chapter 5). The large range of  $\delta D$  values of fluid inclusion waters may reflect mechanical mixing during laboratory extraction of these two different fluid inclusion populations, rather than fluid mixing during vein formation.

Calculation of  $\delta^{18}O$  fluid signatures from silica veins in the Mallery Lake area is complicated by the bimodal spatial association in fluid inclusion populations on the scale of tens of micrometers (Chapter 5). It is not possible to assess the relative contribution of these two fluids to the bulk  $\delta^{18}O$  and  $\delta D$  values, but limiting-case values have been calculated (Table 6.2; Figure 6.2). These calculated  $\delta^{18}O$  fluid values assume that the fluids that deposited the quartz were either (a) dominantly the lower temperature, saline fluid, or (b) the higher temperature, dilute fluid. Fournier (1985) showed that a positive correlation exists between temperature and silica solubility. Thus, the higher temperature, dilute fluids can be expected to have carried the majority of  $SiO_2$  in solution, and may therefore have been responsible for the bulk of the quartz vein deposition in the Mallery Lake vein system. This being the case, then the isotopic composition of the silica would largely reflect the isotopic composition of the higher temperature, dilute fluid type (and overlap in isotope compositions between the two fluid types), rather than the lower temperature, saline fluid (i.e.  $\delta^{18}O_{fluid} = -5.6$  to  $-2.2\text{‰}$ ). Therefore, it is probable that the isotopic composition of the lower temperature, saline fluid is unknown.

While it is stressed that this is an hypothetical interpretation, the derived  $\delta^{18}\text{O}_{\text{fluid}}$  values are very similar to those obtained for typical Phanerozoic low-sulphidation epithermal deposits, and imply the involvement of meteoric water, possibly with contributions from magmatic sources.

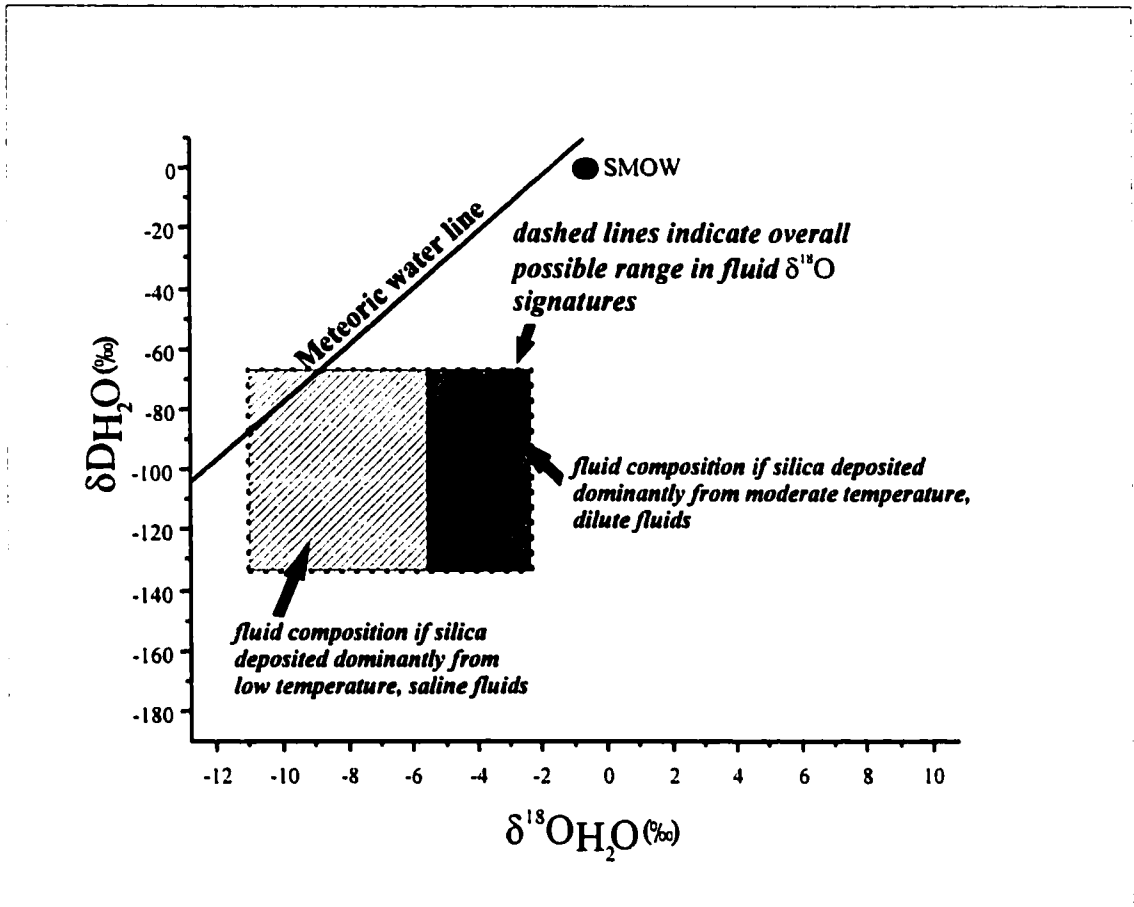


**Figure 6.2.** Possible isotopic compositions of fluids from the Mallery Lake epithermal system. Dashed box outlines the measured  $\delta\text{D}$  and overall possible  $\delta^{18}\text{O}$  fluid range (Table 6.2).

## **CHAPTER 7**

### **RADIOGENIC ANALYSIS OF THE PITZ FORMATION AND NUEL TIN INTRUSIVE SUITE IN THE MALLERY LAKE AREA**

#### **Introduction**

Zircon ( $Zr[SiO_4]$ ) is a common accessory mineral of intrusive and extrusive felsic to intermediate igneous rocks that crystallizes directly from the magma. It is a chemically and physically robust mineral that typically contains high concentrations of uranium and thorium with negligible common lead, thus potentially forming an excellent geochronometer (Heaman and Parrish, 1991). The purpose of this study is to provide temporal constraints for the timing of the Pitz Formation rhyodacite flows (ATPR-2) and a syenite (ATSD-1) of the Neultin Intrusive Suite using U-Pb zircon geochronology (sample locations shown in Figure 3.1) to establish whether these rocks could have been directly involved in the formation of the Mallery Lake epithermal vein stockworks.

#### **Analytical Procedures**

Two samples, weighing between 15 and 25 kilograms, were pulverized using a jaw crusher and Bico disk mill. Zircons were extracted by standard mineral separation techniques involving a Wilfley table, heavy liquid (methylene iodide), and Frantz Isodynamic Separator. After extraction, zircons were separated into fractions based on morphological shape, size, colouration, turbidity, fractures, and presence of inclusions. Some fractions underwent abrasion in order to reduce the effects of surface-related lead loss (Krogh, 1982). All samples were

prepared and analyzed using the radiogenic isotope facilities at the University of Alberta. Bohm *et al.* (1999, in press) outline the procedures involved in chemical preparation and subsequent analysis of zircon fractions. The first zircon fractions were analyzed by use of a VG-354 mass spectrometer, whereas later fractions were analyzed with a Sector 54 mass spectrometer. Analytical procedure blanks during this study are estimated to be 2 pg Pb and 0.5 pg U. The total Pb blank is less than 4 pg, as depicted by the total amount of common Pb measured in two fractions (Table 7.1). Data collected on the VG 354 were corrected for mass discrimination (0.088%/amu Pb and 0.155%/amu U), whereas mass discrimination corrections on the S54 mass spectrometer were (0.1531%/amu Pb and 0.1365%/amu U). The two-stage crustal lead model of Stacey and Kramers (1975) was used to correct for the composition of initial common lead. Ages were calculated using the decay constants for  $^{238}\text{U}$  ( $1.55125 \times 10^{-10} \text{ yr.}^{-1}$ ) and for  $^{235}\text{U}$  ( $9.8485 \times 10^{-10} \text{ yr.}^{-1}$ ) recommended by Jaffey *et al.* (1971). The errors listed in Table 7.1 are reported as one sigma and were calculated by propagating all known sources of uncertainty using an in-house program. All age calculations and associated errors were calculated by using Isoplot software (Ludwig, 1998).

## Results

Zircons extracted from the Nuelin syenite and Pitz Formation rhyodacite (ATSD-1 and ATPR-2, respectively) are colourless to pinkish in colour and have uranium concentrations between 43 and 187 ppm (Table 7.1). Total common lead

**Table 7.1. U - Pb isotopic data of zircon fractions from Pitz Formation rhodacite (ATPR-2) and Nueltin syenite (ATSD-1)**

Description	Weight ( $\mu\text{g}$ )	U (ppm)	Th (ppm)	Pb (ppm)	Th/U	TC:Pb (pg)	$^{206}\text{Pb}/^{238}\text{Pb}$ ( $\pm \times 10^{-4}$ )	$^{207}\text{Pb}/^{235}\text{U}$ ( $\pm \times 10^{-3}$ )	$^{207}\text{Pb}/^{206}\text{Pb}$ ( $\pm \times 10^{-3}$ )	Model Ages (Ma)				%Disc
										$^{206}\text{Pb}/^{238}\text{U}$	$^{207}\text{Pb}/^{235}\text{U}$	$^{206}\text{Pb}/^{238}\text{U}$	$^{207}\text{Pb}/^{235}\text{U}$	
<b>ATPR-2</b>														
ATPR-2-1: z, #1, small, nabr, shed, col, trans, few inc	2	43	27	14	0.63	5	458	0.2757 $\pm$ 9	4.144 $\pm$ 22	0.1090 $\pm$ 5	1570 $\pm$ 5	1663 $\pm$ 4	1783 $\pm$ 8	13.5
ATPR-2-2: z, #38, small, abr, frag, col, trans, no inc	5	118	60	42	0.51	16	668	0.3041 $\pm$ 10	4.382 $\pm$ 19	0.1045 $\pm$ 5	1712 $\pm$ 5	1709 $\pm$ 4	1706 $\pm$ 7	-0.4
ATPR-2-3: z, #34, small, abr, frag, col, trans, few inc	5	121	69	38	0.57	4	2278	0.2837 $\pm$ 6	4.143 $\pm$ 11	0.1059 $\pm$ 1	1610 $\pm$ 3	1663 $\pm$ 2	1731 $\pm$ 2	7.9
ATPR-2-4: z, #6, small, nabr, euh, slipink, trans, few inc, SS4	3	56	39	29	0.69	35	104	0.2889 $\pm$ 12	4.261 $\pm$ 37	0.1070 $\pm$ 10	1636 $\pm$ 6	1686 $\pm$ 8	1749 $\pm$ 16	7.3
<b>ATSD-1</b>														
ATSD-1-1: z, #4, large, nabr, euh, slipink, trans, inc	11	187	93	54	0.50	51	617	0.2464 $\pm$ 5	3.606 $\pm$ 10	0.1062 $\pm$ 2	1420 $\pm$ 3	1551 $\pm$ 2	1734 $\pm$ 3	20.2
ATSD-1-2: z, #25, large, abr, euh, slipink, trans, few inc	59	89	49	30	0.55	27	3787	0.3072 $\pm$ 6	4.567 $\pm$ 10	0.1078 $\pm$ 1	1727 $\pm$ 3	1743 $\pm$ 2	1763 $\pm$ 1	2.4
ATSD-1-3: z, #36, small, arb, euh, slipink, trans, few inc, l103	23	82	46	28	0.56	4	8713	0.3115 $\pm$ 6	4.625 $\pm$ 9	0.1077 $\pm$ 1	1748 $\pm$ 3	1754 $\pm$ 2	1761 $\pm$ 1	0.8
ATSD-1-5: z, #29, small, abr, euh, slipink, trans, few inc, SS4	16	115	65	41	0.57	40	871	0.3071 $\pm$ 6	4.547 $\pm$ 10	0.1074 $\pm$ 1	1726 $\pm$ 3	1740 $\pm$ 2	1756 $\pm$ 2	1.9
ATSD-1-6: z, #13, large, abr, euh, slipink, trans, few inc, SS4	37	95	48	33	0.51	39	1729	0.3083 $\pm$ 6	4.526 $\pm$ 10	0.1065 $\pm$ 1	1732 $\pm$ 3	1736 $\pm$ 2	1740 $\pm$ 2	0.5

z=zircon, (#)=number of grains, abr=abraded, nabr=non-abraded, euh=euhedral, shed=subhedral, frag=fragments col=colourless, slipink=slight pink coloration, trans=transparent, inc=inclusions, SS4=SS4 mass spectrometer  
 \*\* all zircon fractions collected from 0 degree non-magnetic Franz separation

(TCPb), in these zircon samples ranged from 4 to 51 pg. The Th/U ratios for the two samples overlap and range from 0.50 to 0.69 (Table 7.1).

Four zircon fractions were analyzed from the Pitz Formation rhyodacite sample (ATPR-2), and five zircon fractions were analysed from the syenite intrusion (ATSD-1). These data are plotted on a concordia diagram in Figure 7.1. Of the four zircon fractions analyzed from the Pitz Formation, all are discordant except for ATPR-2-2. Fractions ATPR-2-1 and ATPR-2-4 were not abraded due to small fraction size, which may explain their discordance. Fraction ATPR-2-2 was composed of 38 colourless, transparent, fragmented zircon grains free of inclusions and was abraded. This fraction yielded a concordant  $^{207}\text{Pb}/^{206}\text{Pb}$  age (within the  $2\sigma$ -error ellipse) of  $1706\pm 7\text{Ma}$ . In contrast, the  $^{207}\text{Pb}/^{206}\text{Pb}$  ratios for the discordant fractions ATPR-2-1, ATPR-2-3, and ATPR-2-4 yield ages between  $1731\pm 2\text{Ma}$  and  $1783\pm 8\text{Ma}$ , indicating that the zircons in sample ATPR-2 do not define a simple lead loss pattern.

The five zircon fractions extracted from the syenite intrusion (ATSD-1-1, 2, 3, 5, 6) range in their degree of discordance from as high as ~ 20% for ATSD-1-1, to as low as 0.5% for ATSD-1-6. Fraction ATSD-1-6, consisting of 13 large, euhedral, transparent, slightly pink, abraded zircons containing a few inclusions, has a slightly discordant  $^{207}\text{Pb}/^{206}\text{Pb}$  age of  $1740\pm 2\text{Ma}$  and does not fit a discordia line defined by the other four analyses. The latter fractions (ATSD-1-1, 2, 3, 5) define a discordia with an upper intercept age at  $1762\pm 11\text{Ma}$ , and a lower intercept at  $182\pm 150\text{Ma}$ , with an MSWD (Mean Square of Weighted Deviates) of



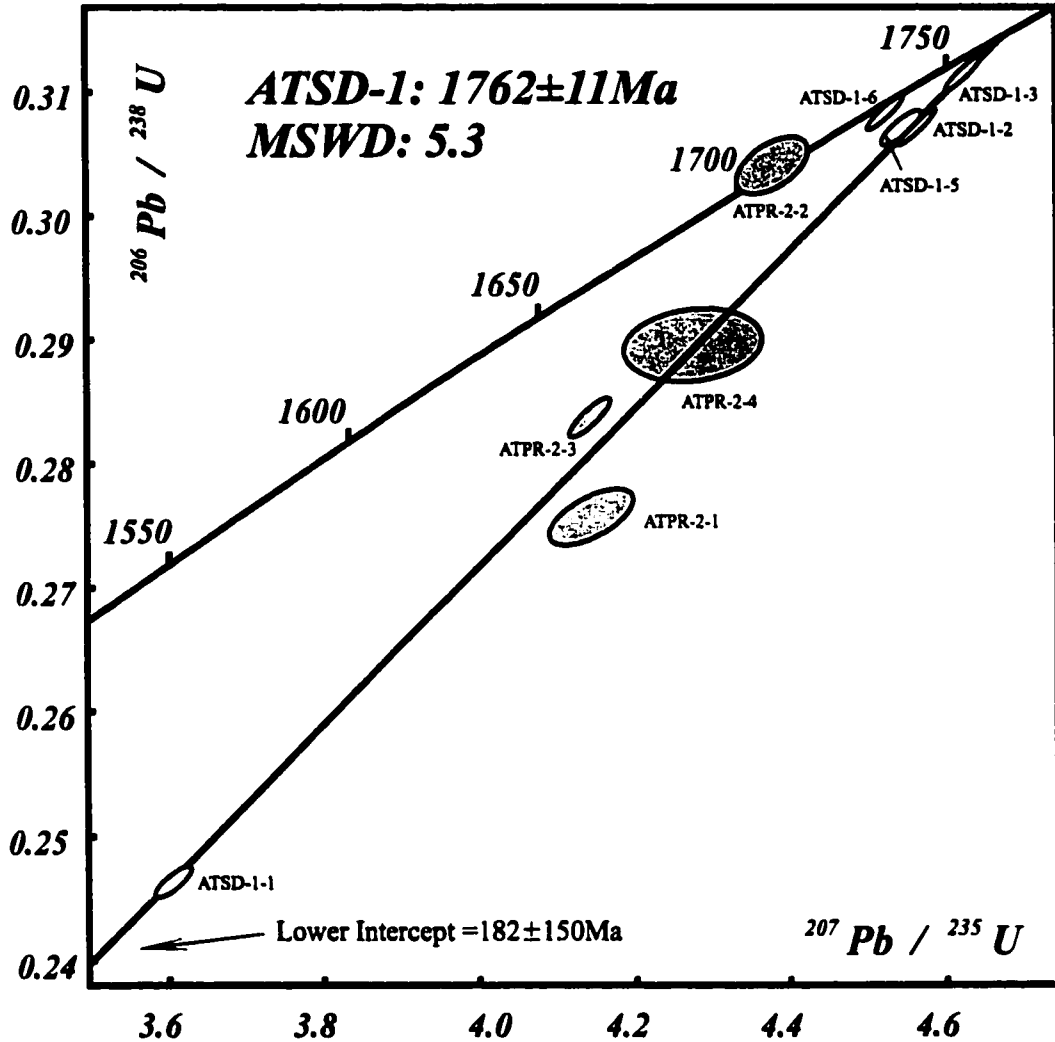


Figure 7.1. U - Pb Host Rock Ages. Two samples were analysed: (1) the Pitz Formation rhyodacite flows (ATPR) shown by the grey error ellipses; and (2) a syenite of the Nueltn Intrusive Suite (ATSD) that is shown by the white error ellipses. All error ellipses are recorded as two-sigma. A regression line was fit to four of the ATSD zircon fractions, indicating an age of  $1762 \pm 11 \text{ Ma}$ , whereas zircon fraction ATSD-1-6 has a slightly discordant  $^{207}\text{Pb}/^{206}\text{Pb}$  age of  $1740 \pm 2 \text{ Ma}$ . The zircon fraction ATPR-2-2 has a concordant  $^{207}\text{Pb}/^{206}\text{Pb}$  age of  $1706 \pm 7 \text{ Ma}$ .

5.3, indicating scatter only marginally in excess of analytical uncertainty resulting from geological variations such as minor inheritance.

## **Discussion**

Interpretation of the ATSD-1 best-fit regression line, formed by the four zircon fractions (ATSD-1-1, 2, 3, 5), is not obvious. One interpretation is that the  $1762 \pm 11$  Ma upper intercept age could represent the time of inherited zircon crystallization. However, an argument against this hypothesis is the narrow range in Th/U ratios of the syenite zircon fractions (0.50 - 0.57; Table 7.1). The consistency of the Th/U ratio data may indicate a high degree of homogeneity in the melt at the time of zircon crystallization. A wider range in Th/U ratios would be expected for zircons containing an inherited Pb component, as it is unlikely that the younger magma would have the same Th/U ratio as the older rock that provided the inherited signature. No visible core / overgrowth relationships were observed in the zircon fractions.

The  $^{207}\text{Pb}/^{206}\text{Pb}$  age of  $1740 \pm 2$  Ma for the fraction ATSD-1-6, although slightly discordant, may represent a more accurate estimate for the age of primary zircon crystallization. This  $^{207}\text{Pb}/^{206}\text{Pb}$  age could be interpreted as the time of emplacement of the syenite body. The difference in apparent age between fraction ATSD-1-6 and the best-fit regression line is approximately 20 m.y.. The  $1762 \pm 11$  Ma age could possibly be the initial age of zircon crystallization, while the  $1740 \pm 2$  Ma age may define a second pulse of magmatism. A 20 m.y. delay between magma pulses in an anorogenic extensional setting is plausible, as is

proposed for the timing associated with the volcanism of the Rio Grande Rift (Christiansen *et al.*, 1986; Oldow *et al.*, 1989).

Interpretation of the zircon results from the Pitz Formation sample is also not definitive. Three of the four zircon fractions analyzed from the Pitz Formation sample (ATPR-2), are discordant whereas ATPR-2-2 is concordant. The three discordant fractions do not define a discordia line and their discordance may be caused by a combination of lead loss (episodic or continuous) and minor inheritance (Faure, 1986). The concordant fraction has a  $^{207}\text{Pb}/^{206}\text{Pb}$  age of  $1706\pm 7\text{Ma}$ , which is interpreted to be the age of rhyodacite emplacement. The large  $2\sigma$ -error ellipses of some of the Pitz Formation zircon fractions is due to small fraction sizes (2-5  $\mu\text{g}$ ), and low uranium concentration levels. The wide range in  $^{207}\text{Pb}/^{206}\text{Pb}$  ages for the different fractions ( $1706\pm 7\text{Ma}$  to  $1783\pm 8\text{Ma}$ ) is evidence for inheritance (caused by the contamination of rhyodacitic magma with somewhat older crustal material). Further supporting evidence for mixing between zircon populations may be evident in the range of Th/U ratios (0.69 to 0.51; Table 7.1).

Peterson and van Breemen (1999) claim that the Pitz Formation is the external equivalent of the Nueltin Intrusive Suite based on their geochemical similarities and field cross cutting relationships. The concordant age of  $1706\pm 7\text{Ma}$  for the Pitz Formation fraction ATPR-2-2 does not coincide with the unpublished U-Pb zircon age of  $1752\pm 2\text{Ma}$  attained by J.C. Roddick for a Pitz rhyolite sample located west of Pamiutuq pluton (pers. comm., T. Peterson, 1999).

The upper intercept age of  $1762 \pm 11$  Ma obtained for the syenite is consistent with the range in ages (1750 to 1757 Ma) proposed for emplacement of the Neultin Intrusive suite in the vicinity of the Baker Lake Basin (pers. comm., A.N. LeCheminant, 1999; Loveridge *et al.* 1987). Thus the Pitz Formation and the Neultin Intrusive suite do not appear to be coeval, but represent distinct magmatic events at approximately 1740 and 1706 Ma.

## **CHAPTER 8**

### **Sm-Nd ANALYSIS OF HYDROTHERMAL FLUORITE IN THE MALLERY LAKE AREA**

#### **Introduction**

Radiogenic isotopes have application to hydrothermal systems in two principle areas: (1) determining the timing of the hydrothermal events in the system (geochronology), and (2) isotopic “tracers” of the source material (isotope geochemistry). Many hydrothermal systems present particular problems for direct isotopic dating due to a lack of suitable minerals. The U-Pb, K-Ar, and Rb-Sr systems frequently provide suspect results because of continuous or episodic chemical and thermal fluctuations associated with later fluid flow events via preexisting fracture conduits (Chesley *et al.*, 1991). The Sm-Nd system has potential for dating hydrothermal systems because of the geochemical coherence of the rare earth element series (Halliday *et al.*, 1990; Chesley *et al.*, 1991; Chesley *et al.*, 1994). Analyses of Sm and Nd for absolute age dating can be problematic due to the elements’ similarities in atomic radii (1.08Å (Nd) and 1.04 Å (Sm)) and charge (3<sup>+</sup>). These similarities result in low chemical fractionation between Sm and Nd, hence Sm/Nd ratios in the majority of minerals range from only 0.15 to 0.37 (Faure, 1986). Fluorite, however, contains elevated REE concentrations and shows significant variations in the Sm/Nd ratio. The Mallery Lake Epithermal System has an abundance of hydrothermal fluorite, and therefore a Sm-Nd study was initiated.

## Isotope Calculations and Notation

### *Sm-Nd Decay Relationship*

The standard isochron equation that expresses the Sm-Nd decay relationship is as follows:

$$[^{143}\text{Nd}/^{144}\text{Nd}]_{(\text{present})} = [^{143}\text{Nd}/^{144}\text{Nd}]_{(\text{initial})} + [^{147}\text{Sm}/^{144}\text{Nd}]_{(\text{present})} (e^{\lambda_{147}t} - 1)$$

Where  $\lambda_{147}$  is the decay constant ( $6.54 \times 10^{-12} \text{a}^{-1}$ ) and “t” is the age of the particular system.

### *Epsilon Notation*

The epsilon notation ( $\epsilon\text{Nd}$ ) measures the variation of a sample or sample suite from the uniform reservoir values of Chondritic Uniform Reservoir (CHUR; Rollinson, 1993). Preferred present day CHUR values for  $^{143}\text{Nd}/^{144}\text{Nd}$  and  $^{147}\text{Sm}/^{144}\text{Nd}$  are 0.512638 (Goldstein *et al.*, 1984) and 0.1967 (Jacobsen and Wasserburg, 1980), respectively. The epsilon notation ( $\epsilon\text{Nd}$  at a given time) is expressed as follows:

$$\epsilon\text{Nd}_{(t)} = [^{143}\text{Nd}/^{144}\text{Nd}_{\text{sample}(t)} / ^{143}\text{Nd}/^{144}\text{Nd}_{\text{CHUR}(t)} - 1] \times 10^4$$

### *Model Ages (CHUR and Depleted Mantle (DM))*

The model age refers to the length of time that a sample has been separated from the mantle. This age can be expressed as two different standards: (1) Depleted Mantle (DM) Reservoir ( $T_{\text{DM}}$ ), and (2) CHUR. The age of this depleted mantle is calculated using the following expression:

$$T_{\text{DM}} = 1/\lambda \cdot \ln \left\{ 1 + \left[ \frac{(^{143}\text{Nd}/^{144}\text{Nd}_{\text{sample, today}} - ^{143}\text{Nd}/^{144}\text{Nd}_{\text{DM, today}})}{(^{147}\text{Sm}/^{144}\text{Nd}_{\text{sample, today}} - ^{147}\text{Sm}/^{144}\text{Nd}_{\text{DM, today}})} \right] \right\}$$

Present day depleted mantle  $^{143}\text{Nd}/^{144}\text{Nd}$  and  $^{147}\text{Sm}/^{144}\text{Nd}$  values of 0.513163 and 0.2137 are used for the calculations (Goldstein *et al.*, 1984). Alternately, a model age can be calculated in terms of CHUR by substituting the  $^{143}\text{Nd}/^{144}\text{Nd}$  and  $^{147}\text{Sm}/^{144}\text{Nd}$  Depleted Mantle values of Goldstein *et al.* (1984) for the CHUR values of Goldstein *et al.* (1984) and Jacobsen and Wasserburg (1980) discussed previously.

## **Samples**

Hydrothermal fluorites were sampled based on color, host rock mineralogy, and location (Figure 3.1). All fluorite samples were collected from in situ silica veins except for two (samples Mauso and T-Rex). These two fluorite samples were extracted from a large quartz boulder in field location ST-10-13. Reconnaissance fluid inclusion studies conducted on fluorite extracted from the Mallery Lake hydrothermal veins revealed an intimate association between fluorite and the high salinity (Type 2) fluid described in Chapter 5, and the absence of Type 1 fluid inclusions. Saline (dominantly Ca-Na-Cl rich) fluids with moderate homogenization temperatures (typically between 90°C - 160°C) are characteristic of the deposition of fluorite in other fluorite-bearing ore deposits (Rogers, 1978; Halliday *et al.*, 1990; Chesley *et al.*, 1991; Chesley *et al.*, 1994). It is therefore proposed that the fluorite in the Mallery Lake hydrothermal system was deposited by the saline (Type 2) fluid.

## **REE Analyses**

Prior to conducting the geochronological or isotopic tracer study on the hydrothermal fluorites, four fluorite samples (Chal 1207, Caldera, T-Rex, and Mauso) were sent to Activation Laboratories. The relative abundance of REE was measured for

**Table 8.1. Fluorite rare earth elements normalized to chondritic elemental values**

Sample	La*	Ce*	Pr*	Nd*	Sm*	Eu*	Gd*	Td*	Dy*	Ho*	Er*	Tm*	Yb*	Lu*
Caldera 1	2.479664	1.7659362	1.3722628	0.9845288	0.5627706	0.2298851	0.2614379	0.1724138	0.1574803	0.1175088	0.1606426	0.1404494	0.1209677	0.1312336
Chal 1207	63.215259	43.051202	40.927007	31.786217	26.406926	11.356322	19.509804	20.344828	15.669291	15.158637	15.903614	18.651686	18.228606	16.561668
Mauso Purple	4.1688373	3.3960293	2.9709029	2.6441632	2.0779221	1.6551724	1.5696275	1.0344828	0.7349031	0.5875441	0.6425703	0.5617978	0.6241935	0.4724409
T-Rex Green	12.643052	20.167189	37.817518	57.66526	70.562771	51.632184	48.99281	20.862069	11.653543	7.6380729	0.6425703	1.1797753	0.6854839	0.6036745

All analysis conducted at Activation Laboratories via ICP-MS (Inductively coupled plasma emission mass spectrometry)

\* Chondritic values used in normalizing REE (concentrations in ppm)

Average CI (#7) -- T & M -- Isotope Dilution Mass Spectrometry (IDMS) from Taylor and McLennan (1985).



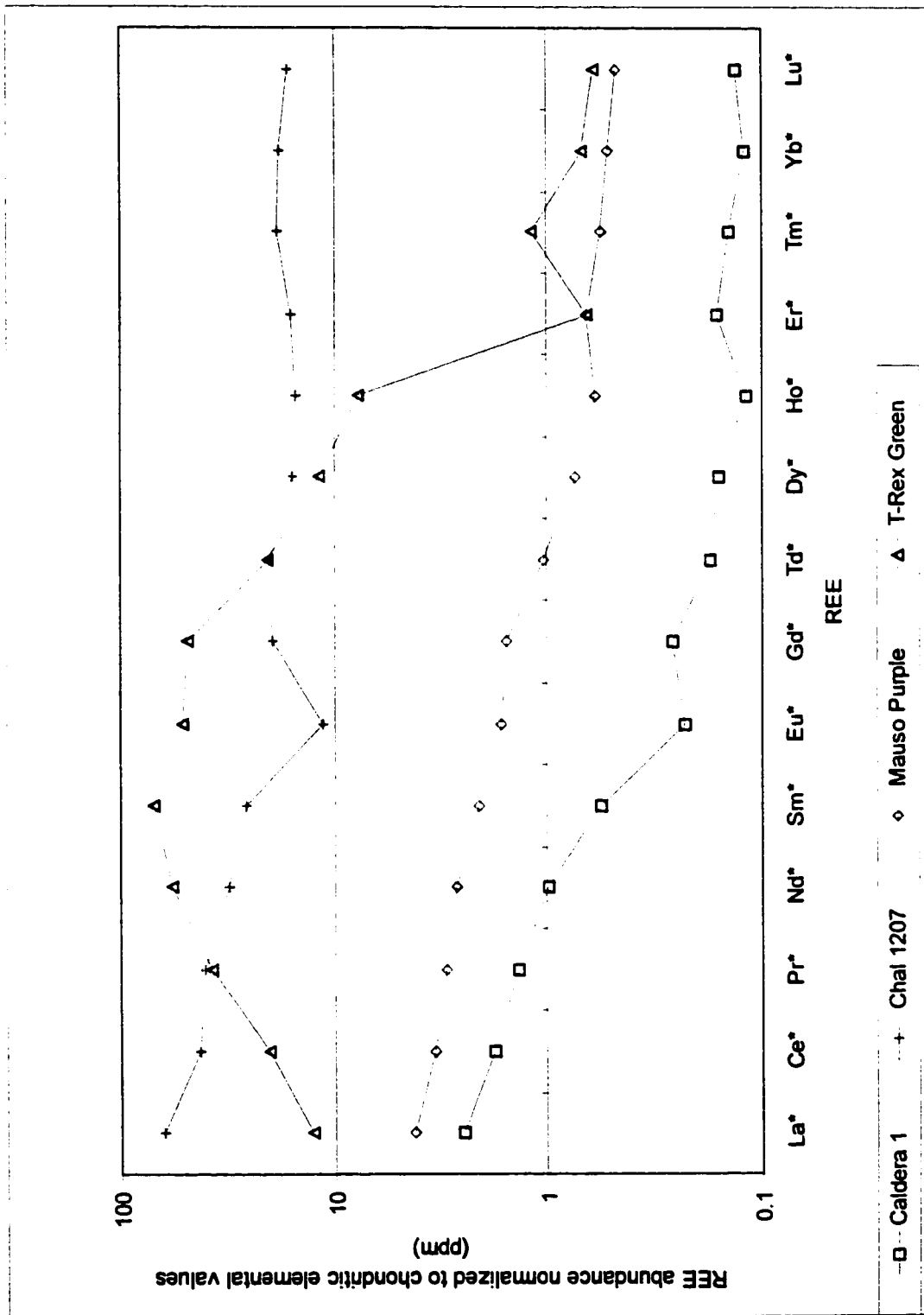


Figure 8.1. Rare earth element pattern of four fluorite samples from the Mallery Lake epithermal system

these samples by ICP-MS analysis. The REE patterns were normalized to the chondritic element values of Taylor and McLennan (1985). The results of these REE analyses indicate that samples Chal 1207, Caldera, and Mauso, have a higher abundance of light REE relative to heavy REE (Table 8.1; Figure 8.1). The concentrations of light REE (La to Gd) to heavy REE (Tb to Lu) for these three samples are consistent with typical patterns for fluorites (Naldrett *et al.*, 1987). Sample T-Rex has a very different REE abundance pattern from typical fluorite, and therefore is interpreted to have limited usefulness in geochronology. Furthermore, the intimate spatial associations between sample Mauso with T-Rex renders sample Mauso as also suspect.

### **Sm-Nd Analytical Procedures**

Samples were processed using conventional crushing and separation techniques. Sample weights are dependent on the concentration of Nd within each sample and therefore varied from 50 µg to 250 µg. All Sm and Nd analyses were conducted in the University of Alberta Radiogenic Isotope Laboratory. Fluorite sample powders were spiked with a  $^{150}\text{Nd}$  and  $^{149}\text{Sm}$  tracer solution and dissolved in 6 ml of a 1:1 mixture of 16 N nitric acid and 6.2 N hydrochloric acid in sealed PFA teflon vessels at ~ 160°C for 48 to 72 hours. The teflon sample vessels were then uncapped and the solution evaporated to dryness. This procedure was repeated until total dissolution of the sample was attained and all fluoride ions were driven from the residue. The samples were then re-dissolved in 6 ml of 6.2 N hydrochloric acid for ~ 24 hours and subsequently dried down. This procedure was repeated to ensure total conversion of fluoride compounds to chloride form. Samples were then re-dissolved in 6 ml 0.75 N hydrochloric acid, for a ~24 hour

period, in preparation for column chemistry. The rare earth elements were separated from the solution using BioRad AG50-X8 200-400 mesh cation resin in PFA teflon columns. Sm and Nd were separated from the other REE and each other by using Di(2-ethylhexyl phosphate) based chromatography (HDEHP). The isotopic compositions, of the separated Sm and Nd, were then determined on either a VG-354 or MM30 mass spectrometer. The raw ratios for Sm and Nd were corrected for variable mass-discrimination to  $^{146}\text{Nd}/^{144}\text{Nd} = 0.7219$  and  $^{152}\text{Sm}/^{154}\text{Sm} = 1.17537$  using the exponential law (Wasserburg *et al.*, 1981). Repeated runs of the La Jolla Nd isotope standard gave an average  $^{143}\text{Nd}/^{144}\text{Nd} = 0.511833$  with an external reproducibility error of  $\pm 0.000011(2\sigma)$ . The reproducibility errors of the samples, which are based on local and universal standards (ST-2 and BCR-1), are 0.00015 for  $^{143}\text{Nd}/^{144}\text{Nd}$  and 0.002 for  $^{147}\text{Sm}/^{144}\text{Nd}$  ( $1\sigma$ ; Rho value of zero). Total procedure blanks for Nd and Sm were determined to be 130.89 pg and 234.88 pg, within the accepted procedure blank range of <400 pg and <800 pg normally attained (pers comm. R. Creaser, 1999).

## Results

### *Isotopic Ratios (Integrity of the Isochron)*

Sm-Nd isotopic compositions of 12 fluorite samples are listed in Table 8.2. The fluorite samples yielded  $^{147}\text{Sm}/^{144}\text{Nd}$  ratio values from 0.11 (Caldera) to 0.52 (AT 10-7-3), a spread of over two times that of most minerals. Samples AT 19-9, Caldera, Chal 1207, and the AT-10-7 series plot in a linear array, whereas samples T-Rex and Mausó scatter below this line (Figure 8.2) and are therefore dismissed on the basis of poor locational constraint. Fluorite collected from locality ST-10-7 are purple to

**Table 8.2. Sm - Nd fluorite data (Mallery Lake)**

Sample Number	Sample Location	Host Rock Lithology	Color	Sm (ppm)	Nd (ppm)	I/Nd (ppm)	Sm/Nd	$^{147}\text{Sm}/^{144}\text{Nd}$ (2 $\sigma$ error)	$^{143}\text{Nd}/^{144}\text{Nd}$ (2 $\sigma$ error)	$^{143}\text{Nd}/^{144}\text{Nd}$ (t=1.435 Ga)
AT 10-7-1	ST 10-7	PF <sup>*</sup>	purple	6.50	10.79	0.09	0.60	0.3643±20	0.513707±6	0.51027
AT 10-7-2	ST 10-7	PF <sup>*</sup>	white	12.09	18.22	0.05	0.66	0.4011±20	0.514105±35	0.51027
AT 10-7-3	ST 10-7	PF <sup>*</sup>	purple-white	8.99	10.42	0.10	0.86	0.5215±20	0.515238±7	0.51032
AT 10-7-4	ST 10-7	PF <sup>*</sup>	white	7.17	8.89	0.11	0.81	0.4880±20	0.514900±6	0.51030
AT 10-7-5	ST 10-7	PF <sup>*</sup>	purple	8.42	14.20	0.07	0.59	0.3585±20	0.513663±5	0.51028
AT 10-7-6	ST 10-7	PF <sup>*</sup>	purple-white	3.55	7.86	0.13	0.45	0.2731±20	0.512911±5	0.51034
AT 10-7-(original)	ST 10-7	PF <sup>*</sup>	white	13.61	20.36	0.05	0.67	0.4044±20	0.514106±6	0.51029
Chal 1207	Chal Zn	PF <sup>*</sup>	purple	5.31	20.74	0.05	0.26	0.1548±20	0.511728±9	0.51027
Caldera	Fl Zn	AG <sup>*</sup>	purple	1.38	7.49	0.13	0.18	0.1115±20	0.511366±10	0.51031
AT 19-9	Zone 1	AG <sup>*</sup>	purple	0.91	3.18	0.31	0.29	0.1740±20	0.511962±9	0.51032
Mauso	ST 10-13	CIF <sup>*</sup>	purple	0.33	1.55	0.65	0.21	0.1293±20	0.511171±10	0.50995
T-Rex	ST 10-13	CIF <sup>*</sup>	green	13.29	34.62	0.03	0.38	0.2321±20	0.511654±11	0.50946

AG=Archean Gneiss, CIF=Christopher Island Formation, t=time

Ratio errors indicate the uncertainty associated with each measurement of the mass spectrometer (2 $\sigma$ ), not to be confused with the reproducibility to one standard of deviation of the population used for regression line fitting, plotting, and age determination.

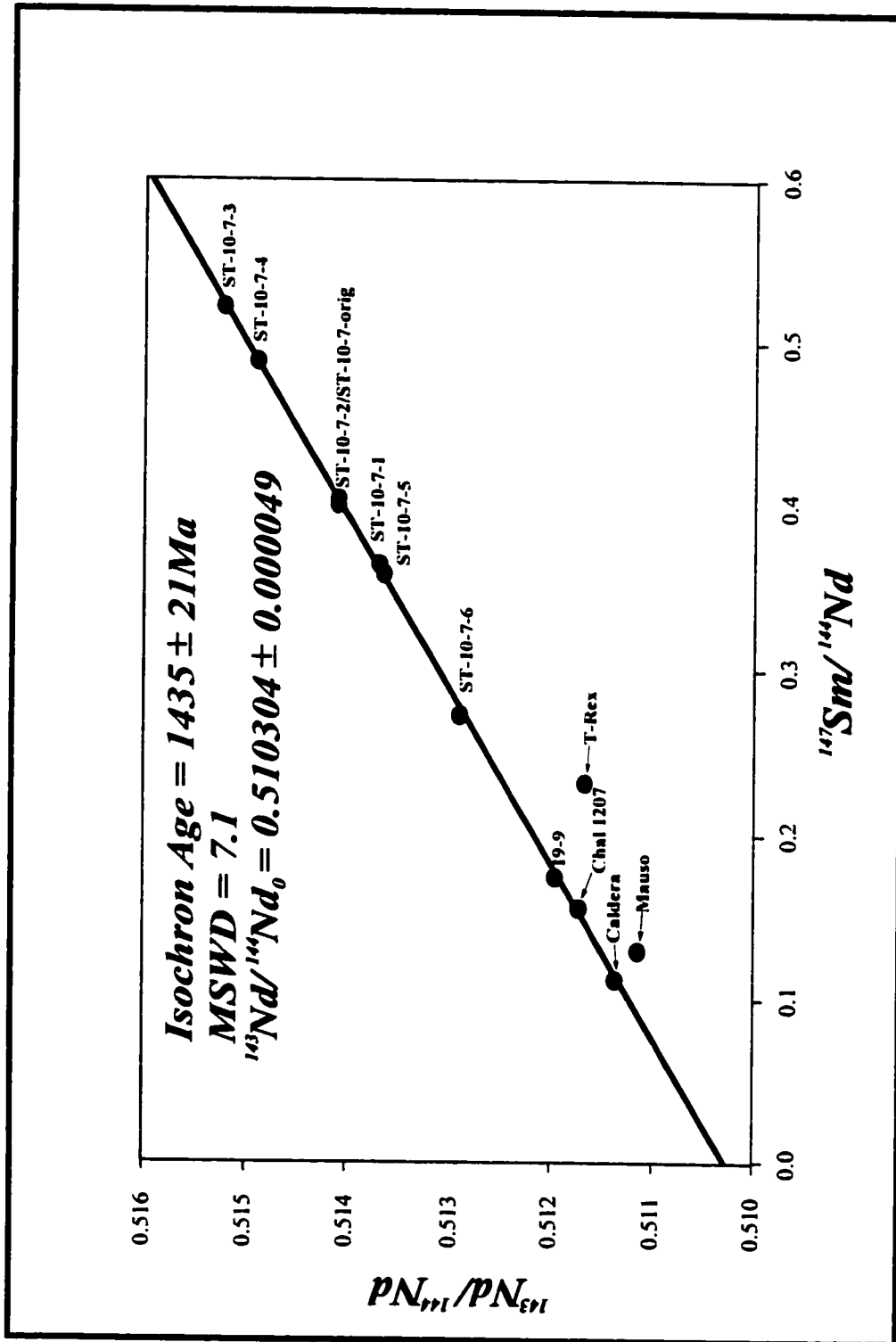


**Figure 8.2.**  $^{147}\text{Sm}/^{146}\text{Nd}$  versus  $^{143}\text{Nd}/^{144}\text{Nd}$  isochron diagram for 12 fluorite vein samples from the Mallery Lake area. Samples Mauro and T-Rex were not included in determination of the regression line (see text). Samples with the prefix ST-10-7 were all taken from the same outcrop location (see Figure 3.1).

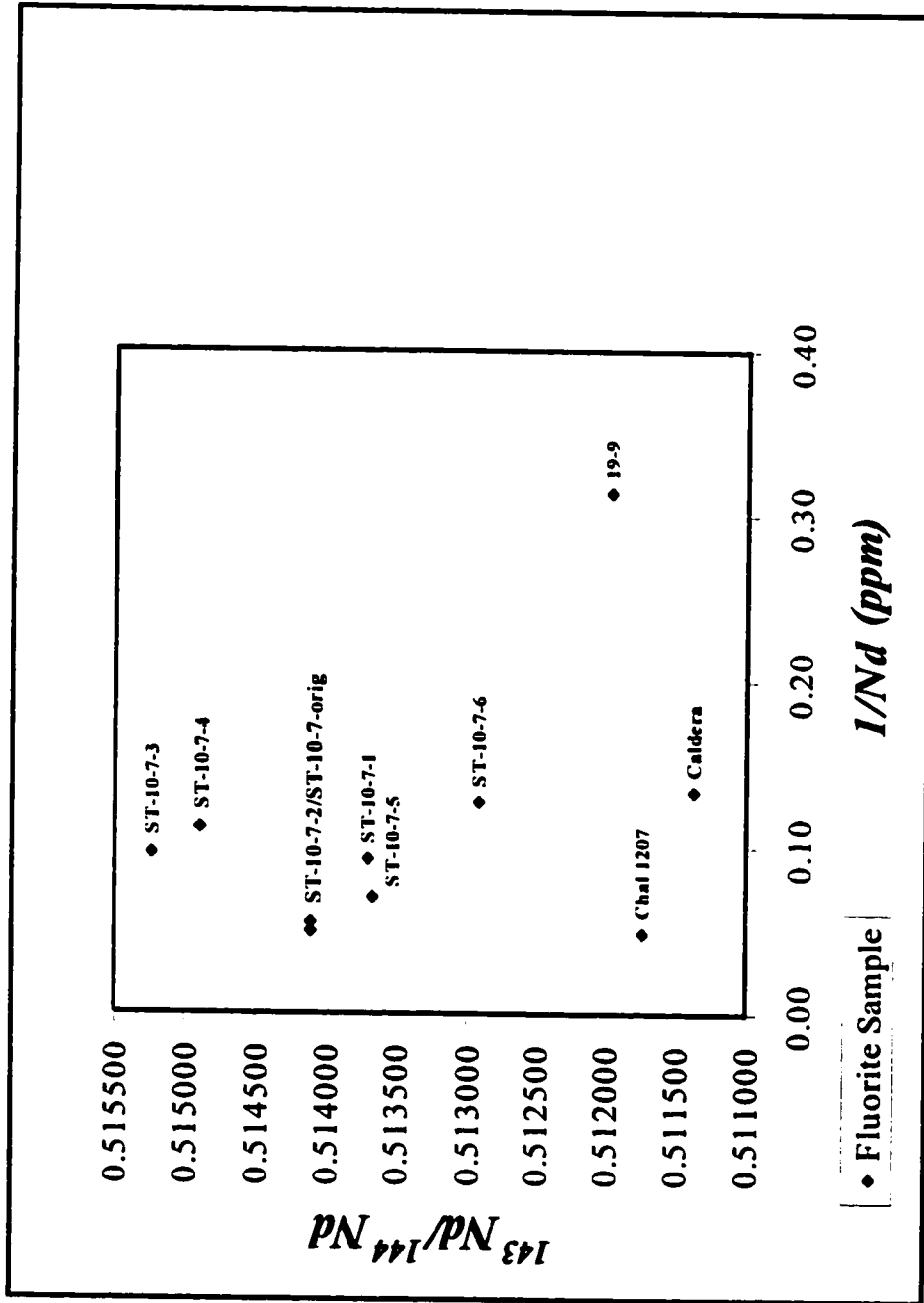


**Figure 8.3.**  $^{143}\text{Nd}/^{144}\text{Nd}$  vs.  $1/\text{Nd}$  (ppm). The  $^{143}\text{Nd}/^{144}\text{Nd}$  ratios are observed to be independent of the Nd concentrations for the fluorite samples, and therefore indicates that the isotopic ratios are not a function of mixing between two end-member populations.

purple-white in coloration, and have isotopic ratios ranging from  $^{143}\text{Nd}/^{144}\text{Nd} = 0.512911$  to  $0.515238$  and  $^{147}\text{Sm}/^{144}\text{Nd} = 0.2731$  to  $0.5215$ . Naldrett *et al.* (1987) determined that there is no relation between the enrichment or depletion of REE and variation and color, but rather that color variation is an indication of the thermal history of the fluorite, or its exposure to light. It is possible that the transition in colors from purple to purple-white for the fluorite at location ST-10-7 may reflect cooling of the hydrothermal fluids during continued fluorite deposition, or fluorite that was bleached by sun light as the sample was taken from the surface of the outcrop.

The linear array of data in Figure 8.2 might be interpreted either as an isochron or as a mixing trend. In order to test which interpretation is correct  $^{143}\text{Nd}/^{144}\text{Nd}$  ratios vs.  $1/\text{Nd}$  ppm concentrations for the ten collinear samples (excluding samples Mauso and T-Rex) are plotted in Figure 8.3. The  $^{143}\text{Nd}/^{144}\text{Nd}$  ratios are observed to be independent of Nd concentrations, indicating that the isotopic ratios are not a function of mixing between two end-member populations. The data are therefore interpreted to have age significance.

Regression of these ten analyses yields an isochron with an age of  $1435 \pm 21 \text{ Ma}$  ( $2\sigma$ ), an MSWD (Mean Square of Weighted Deviates) of 7.1, and an initial ratio of  $0.510304 \pm 0.000049$ . The slightly elevated MSWD of 7.1 infers geologic variation causing scatter around the best-fit regression line as determined by a York fit (Model 3). Two plausible explanations for the geological scatter are: (1) the extent of host rock alteration; and (2) variations in the initial  $^{143}\text{Nd}/^{144}\text{Nd}$  isotopic values of the host rock.

The regression calculated using only fluorite from locality ST-10-7 does not change the age or MSWD of the isochron significantly (i.e., an age of  $1435 \pm 53$  Ma and an MSWD of 6.6).

#### *Initial Nd Isotopic Compositions*

An  $\epsilon\text{Nd}_{(1435\text{Ma})}$  value of  $-9.4 \pm 1$  ( $2\sigma$ ) was calculated for the fluorite suite, using their average present day  $^{143}\text{Nd}/^{144}\text{Nd}$  and  $^{147}\text{Sm}/^{144}\text{Nd}$  values of 0.513354 and 0.323521 determined by the York fit (Model 3) program, and the  $^{143}\text{Nd}/^{144}\text{Nd}$  calculated CHUR value of 0.51078 at 1435 Ma.  $\epsilon\text{Nd}_0$  values at  $\sim 1.71$  Ga (age of sample ATPR 2-2) and 1435 Ma were also calculated for the Pitz Formation using the Sm-Nd data of Dudas *et al.* (1991; Table 8.3). The results of this analysis indicate that at 1435 Ma the six Pitz Formation  $\epsilon\text{Nd}$  values ranged from -10.8 to -12.3 (Table 8.3), a difference of only  $\sim 0.4$  epsilon units from that of the fluorite suite. This close similarity suggests that most of the Nd in the hydrothermal fluorites was derived from the Pitz Formation, with minor contributions from a more primitive material.



**Table 8.3. 79LAA-T250 Pitz Formation (data from Dudas *et al.*, 1991)**

Sample	Sample Location	Lithology	Sm (ppm)	Nd (ppm)	$^{147}\text{Sm}/^{144}\text{Nd}$ ( $\pm 2$ sigma)	$^{143}\text{Nd}/^{144}\text{Nd}$ ( $t^*=1.71$ Ga)	$^{143}\text{Nd}/^{144}\text{Nd}$ ( $t^*=1.71$ Ga)	$\epsilon_{\text{Nd}}$ , 1.71 Ga ( $t^*=1.71$ Ga)	$\epsilon_{\text{Nd}}$ , 1.435 Ga ( $t^*=1.435$ Ga)	$\epsilon_{\text{Nd}}$ , today ( $t^*=$ present day)	$^{40}\text{Ar}/^{39}\text{Ar}$ T <sub>DM</sub> Ga
1	79LAA-T250	PF*	17.90	87.51	0.12364	0.511357±6	0.50997	-9.17±0.09	-11.53	-24.99	3.04
2	79LAA-T250	PF*	17.91	87.43	0.12378	0.511388±7	0.51000	-8.51±0.14	-10.95	-24.38	2.99
3	79LAA-T250	PF*	17.89	86.67	0.12474	0.511347±1	0.50995	-9.52±0.32	-11.93	-25.18	3.09
4	79LAA-T250	PF*	17.89	87.43	0.12365	0.511386±1	0.51000	-8.52±0.24	-10.96	-24.42	2.99
5	79LAA-T250	PF*	17.89	87.51	0.12355	0.511373±1	0.50999	-8.75±0.23	-11.20	-24.68	3.01
6	79LAA-T250	PF*	17.74	86.80	0.12349	0.511335±9	0.50995	-9.48±0.18	-11.93	-25.42	3.07

PF\* = Pitz Formation,  $t^*$  = age of Pitz Formation zircon analysis (U - Pb chapter),  $t$  = time

$^{40}\text{Ar}/^{39}\text{Ar}$  T<sub>DM</sub> are recalculated using the  $^{143}\text{Nd}/^{144}\text{Nd}$  value of 0.613163 and the  $^{147}\text{Sm}/^{144}\text{Nd}$  value of 0.2137 (Goldstein *et al.*, 1984)

## CHAPTER 9

### DISCUSSION

#### **Metal transport and deposition in the ore-bearing fluid at Mallery Lake**

Microthermometric and semi-quantitative EDS microprobe analysis indicate that metals were deposited in the early event of silica deposition (703527) and the later event that is characterized by quartz-hematite veins (703530). By identifying the fluid type as well as its conditions, the ligand(s) involved in metal transport can be inferred.

#### *Metal ligand classification*

Seward and Barnes (1997) classify metal complexes, using the electron donor-acceptor theory, as hard (class “a”) and soft (class “b”) Lewis acids and bases. Hard metals (electron acceptors) prefer to bind to hard ligands (electron donors), forming a complex characterized by a high charge and/or small radius. In contrast, soft metals have an availability of electrons that can easily be dislocated. Due to this electron availability, soft metals typically form covalent bonds with soft donors. Classifications of these metals are shown in Table 9.1.

**Table 9.1.** Classification of some metals and ligands in terms of Class “a” and Class “b” behavior (Seward and Barnes, 1997)

<b>Class “a” Metals</b>	<b>Borderline</b>	<b>Class “b” Metals</b>
H <sup>+</sup> , Li <sup>+</sup> , Na <sup>+</sup> , K <sup>+</sup> , Be <sup>3+</sup> , Ca <sup>2+</sup> , Mg <sup>2+</sup> , Sr <sup>2+</sup> , Al <sup>3+</sup> , Fe <sup>3+</sup> , Cr <sup>3+</sup> , La <sup>3+</sup>	Divalent transition metals including Zn <sup>2+</sup> , Pb <sup>2+</sup> , and Bi <sup>3+</sup>	Cu <sup>+</sup> , Ag <sup>+</sup> , Au <sup>+</sup> , Au <sup>3+</sup> , Hg <sup>2+</sup> , Cd <sup>2+</sup> , Sn <sup>2+</sup> , Tl <sup>+</sup> , Tl <sup>3+</sup>
<b>Class “a” Ligands</b>	<b>Borderline</b>	<b>Class “b” Ligands</b>
F <sup>-</sup> , OH <sup>-</sup> , NH <sub>3</sub> , NO <sub>3</sub> <sup>-</sup> , HCO <sub>3</sub> <sup>-</sup> , CO <sub>3</sub> <sup>2-</sup> , HSO <sub>4</sub> <sup>-</sup> , SO <sub>4</sub> <sup>2-</sup> , H <sub>3</sub> SiO <sub>4</sub> <sup>-</sup> , HPO <sub>4</sub> <sup>2-</sup> , PO <sub>4</sub> <sup>3-</sup> , CH <sub>3</sub> COO <sup>-</sup>	Cl <sup>-</sup> , Br <sup>-</sup>	I <sup>-</sup> , HS <sup>-</sup> , S <sub>2</sub> O <sub>3</sub> <sup>2-</sup> , SCN <sup>-</sup> , CN <sup>-</sup>

Chloride and hydrosulphide ions are ubiquitous in most hydrothermal fluids, and are considered probable ligands in the transport of base and precious metals (Seward, 1991). Ligands such as bromide and iodide have a higher complex stability than chloride, but are typically not present in sufficient concentration in hydrothermal fluids to be viable for metal transport.

### ***Physical-chemical conditions of the ore-bearing fluid***

Vein and alteration mineralogy provides indications of the hydrothermal fluid conditions. The host rock alteration intimately associated with the silicification at Mallery Lake is phyllic with traces of argillic (Chapter 3). Mineralogically, alteration is characterized by adularia followed by a phyllic overprint of sericite and illite, grading to kaolinite in the argillic patches.

Aside from the native silver of Sample 703527 (Table 3.3), and the electrum and trace acanthite-argentite identified in the cross-cutting quartz-hematite veins of Sample 703530 (Table 3.3), there is evidence of oxide and minor sulfide ore mineral deposition. The two vein stages (primary and later quartz-hematite) and their wall rocks contain oxidized metals such as ilmenite and/or titanomagnetite, pyrophanite, rutile, ilmenorutile, and hematite (Chapter 3). Furthermore, there is an association between the two vein stages and minor to trace quantities of base metal sulfides such as chalcopyrite, pyrite, galena, sphalerite, and barite (Chapter 3). Coprecipitation of the ore mineral phases is indicated by the intergrowth of rutile and pyrite, as well as pyrite with barite (Plate 3.2A). Furthermore, an intimate association between hematite

and monazite blebs was frequently observed in the altered Pitz Formation rhyolite flows in the Chalcedonic Stockwork zone.

The association of hematite with monazite blebs indicates that the fluid had a high oxidation state as cesium only decouples from the other rare-earth elements under such conditions (Feng and Abercrombie, 1994). As well, the high oxidation fugacity of the fluid is evident by the coprecipitation of sulfides with sulfates and oxides, the intimate association between hematite and electrum, and the presence of iron in the Type 2 precious metal-bearing fluid inclusion decrepitation residues of samples 703527 and 703530. There is also evidence that the ore-bearing fluids may have been moderately acidic, as indicated by the spatial association between kaolinite and precious metals in Sample 703530 (Seward, 1991).

### ***Solubility and metal transport***

Jaireth (1992), Watkinson *et al.* (1992), Feng and Abercrombie (1994), Mernagh *et al.* (1994), Gammons *et al.* (1997), and Wilkinson *et al.* (1999) stress the importance of oxidized, acidic, low temperature saline fluids (typically characterized by high Ca:Na ratios) in the transport and deposition of precious metals in some environments. These authors argue for precious metal transport as chloride complexes in such systems. Microthermometric and petrographic studies indicate that the Mallery Lake epithermal system contained a fluid (Type 2) that was highly oxidized, saline, mildly acidic, and had low temperatures (typically between 90°C and 150°C; Figure 5.3). Supporting evidence for the involvement of the Type 2 fluid in metal transportation was indicated by the

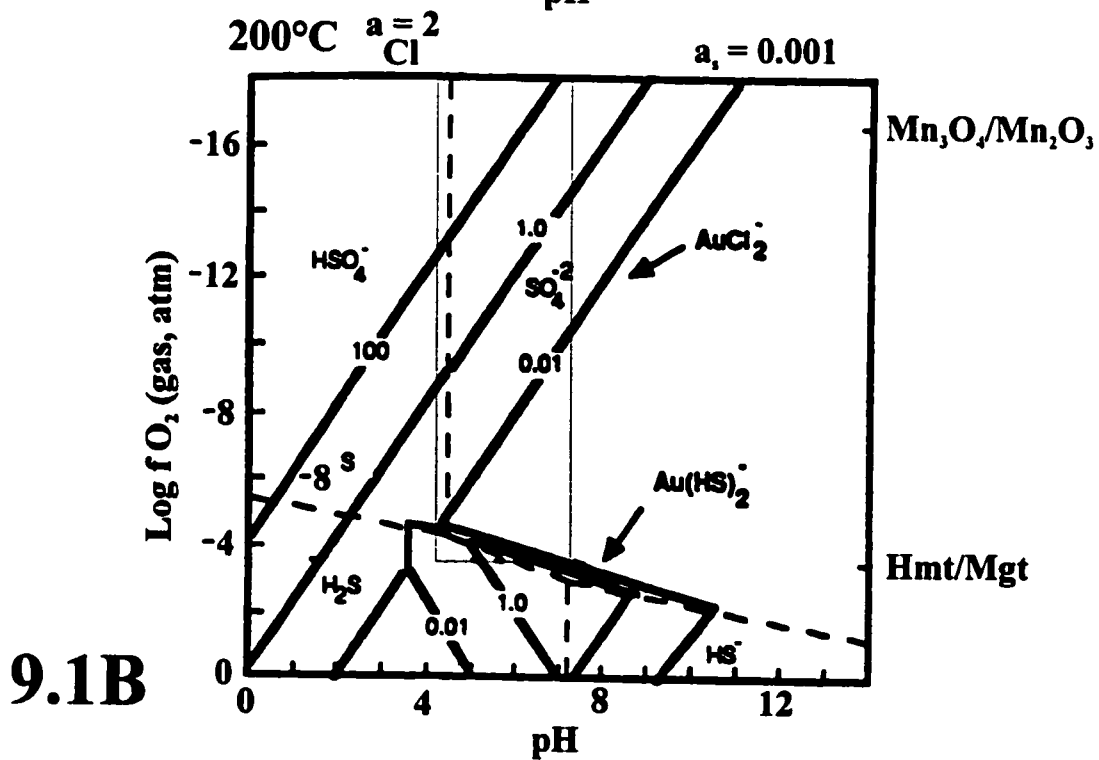
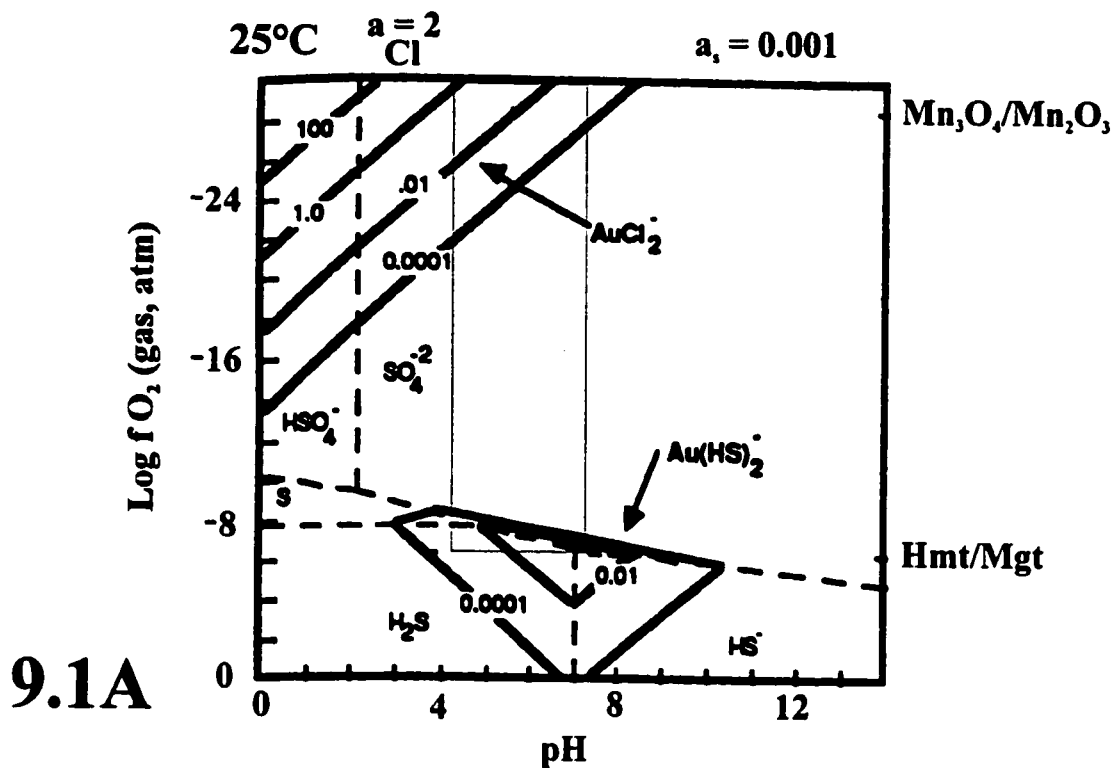
presence of Ag-, Au-, Cu-salts following thermal decrepitation of Sample 703534, as determined by semi-quantitative EDS microprobe analysis (Figure 5.4). This saline Type 2 fluid is similar to those fluids described by other authors as being suitable for precious metal transport. In contrast, the dilute (Type 1) fluid appears to offer little potential as an ore-forming fluid because it contains almost no chloride and presumably little bisulfide if it is oxidized (Figure 9.1A and 9.1B; Jaireth, 1992).

### ***Mechanisms of precious metal deposition***

Figures 9.1a and 9.1b show that oxidized, acidic, saline fluids are capable of transporting elevated quantities of precious metals. These figures further show that an increase in pH, or decrease in temperature or oxidation state of the ore-bearing fluid would destabilize the chloro-complexed precious metals and cause ore deposition. Events that would trigger these effects could include boiling, simple cooling, or mixing of the oxidized ore-bearing fluid with either a more reduced fluid, and/or an altered or unaltered wall rock (Jaireth, 1992; Gammons *et al*, 1997). Because hydrothermal systems are typically dynamic, it is important to approach the question as to the factors involved in ore deposition at Mallery Lake holistically, by not restricting the study to the ore-bearing fluid conditions, but by also examining the alteration assemblage of the ore-bearing veins.

No evidence for boiling or fluid mixing was observed in the Type 2 fluid and so it is possible that simple cooling of this fluid was responsible for deposition of ore.

**Figures 9.1a and 9.1b.** Log  $fH_2$  – pH gold solubility diagrams (Jaireth, 1992). These two figures are Log  $fH_2$  – pH diagrams that show gold solubility at 25°C and 200°C at a chlorine activity = 2. Figure 9.1a shows that a 25°C near-neutral fluid that has an oxidation state equivalent to the hematite/magnetite buffer would complex and transport gold as an  $Au(HS)_2^-$  complex. If however the oxygen fugacity of this fluid increased within the range of the  $Mn_3O_4/Mn_2O_3$  stability field, the gold would complex as  $AuCl_2^-$ , carrying 0.001 ppb and 10 ppb at 200°C (Figure 9.1a and 9.1b). The dashed lines in the two figures outline the stability fields of the sulfur species, where the activity of sulfur is 0.001. The position of the Hmt/Mgt (hematite-magnetite) and  $Mn_3O_4 - Mn_2O_3$  buffers are shown by the arrows on the right hand side of the diagrams. As the temperatures of the Type 2 fluid falls between those of Figures 9.1a and 9.1b, the gray boxes indicate possible conditions under which gold was complexed and transported in the Mallery Lake system.



As mentioned previously, the alteration assemblage that was intimately associated with the silicification of the Chalcedonic Stockwork zone was primarily phyllic, with traces of argillic. The phyllic alteration includes the minerals: silica, sericite, hematite, and clays such as illite. Theoretically, potassium feldspar reprecipitates as adularia as a result of a temperature drop, and the devolatilization of CO<sub>2</sub> from the fluid during an event of boiling (White, 1995). Evidence for CO<sub>2</sub> in the form of clathrate melts and dawsonite pseudodaughter minerals was observed in the Type 1B fluids (Chapter 5). If the majority of the silica and adularia was deposited from the higher temperature (Type 1) fluids, then it is possible that this fluid was also responsible for the other aspects of the phyllic alteration assemblage as well. During the ascent of the higher temperature (Type 1) fluids, it is possible that these fluids would move the oxidation-reduction interface deeper into the system by buffering the host rocks. If this is the case, the pulses of the slightly acidic, saline, lower temperature (Type 2) fluid would not be extensively reduced by wall rock reaction during their ascent. The Type 2 fluid interaction with the adularia, sericite, and illite would eventually cause the alteration assemblage in localized patches to advance to argillic, indicated by the formation of kaolinite. In summary, the Type 1 fluid may have been responsible for the pervasive phyllic alteration of the host rock, and Type 2 fluids for the argillic alteration in localized areas.

The source of the high salinity, oxidized Type 2 fluid needs to be addressed. Frapé and Fritz (1982), Frapé *et al.* (1984), and Frapé and Fritz (1987) report the



abundance of high salinity  $\text{CaCl}_2\text{-NaCl}$  fluid in the Archean basement host rocks of Yellowknife, Thompson, and Sudbury. Fluid inclusion studies at Canadian shield-hosted precious metal deposits such as the Con Mine, Giant Mine, Negus Mine, NWT (Boyle, 1961), McIntyre Mine, Ontario (Langford and Hancox, 1936), Sturgeon River Gold mines, Ontario (Bruce, 1941), mines located in the Sudbury Basin, Ontario (Frape and Fritz, 1981), and Copper Rand Mine, Quebec (Guha and Kanwar, 1987), indicate a strong association between saline (typically Ca-Na-Cl) fluid and precious metals. It is thus suggested that saline fluids under oxidized, slightly acidic fluid conditions were responsible for the transport and deposition of precious metals in these shield deposits. The saline fluid may have been oxidized either prior to hydrothermal circulation, or by interaction with an overlying oxidized horizon (i.e. interaction with units such as the Kunwak Formation discussed in Chapter 2).

### **Comparison of the Mallery Lake vein system to Phanerozoic low sulfidation epithermal systems**

The Proterozoic Mallery Lake epithermal system shares similarities and differences to those of Phanerozoic low-sulfidation systems such as the Pajingo Mine (Australia), the Acupan Mine (Philippines), the Emperor Mine (Fiji), and the Hishikari Mine located in Japan (Table 9.2). The Mallery Lake epithermal system is comparable to the four Phanerozoic epithermal systems in terms of host rock lithology, silica vein textures, and alteration assemblages (Table 9.2). Differences between the Mallery Lake epithermal system from that of Phanerozoic low-sulfidation

**Table 9.2. Comparison of the Mallery Lake epithermal system to four Phanerozoic low sulfidation epithermal systems.**

	<b>Mallery Lake, Canada</b>	<b>Pajingo, Australia</b>	<b>Acupan, Philippines</b>	<b>Emperor, Fiji</b>	<b>Hishikari, Japan</b>
<b>Host rocks</b>	ultrabasic - acidic intrusive/extrusive, clastic units	intermediate intrusive/extrusive, clastic units	basic - intermediate extrusive, clastic units	basic - intermediate extrusive	intermediate extrusive, clastic
<b>Age of system</b>	1435±21 Ma (Sm-Nd -- fluorite)	late Cretaceous?	1.4 - 0.9 Ma (K-Ar - argillic cap)	4.8 Ma - 3.8 Ma (K-Ar - Tauva rocks)	1.01±0.08 Ma - 0.78±0.16 Ma (K-Ar - Adularia)
<b>Alteration mineralogy</b>	sericite, illite, adularia, fluorite, carbonate, quartz, chalcodony, chlorite, minor kaolinite and monazite	quartz, illite, smectite, adularia, chlorite, kaolinite, epidote, carbonate, albite	quartz, sericite, adularia, carbonate, anhydrite, kaolinite	chlorite, quartz, sericite, adularia, carbonate, roescolite	chlorite, smectite, quartz, adularia, carbonate, kaolinite, truscottite
<b>Alteration classification</b>	phyllitic, propylitic and trace argillic	propylitic, phyllic, intermediate argillic	propylitic, phyllic, advanced argillic (cap)	propylitic, phyllic	propylitic, phyllic, argillic
<b>Characteristics of Ore-bearing fluid</b>	saline (23 wt. % - 31 wt. % CaCl <sub>2</sub> -NaCl), low temperature (90°C - 150°C), slightly acidic, oxidized fluid	dilute (<2.5 wt. % NaCl equiv.) with trace CO <sub>2</sub> , moderate temperature (170°C - 315°C), neutral - to slightly acidic, reduced fluid	dilute (<5.1 wt. % NaCl equiv.) with trace CO <sub>2</sub> , moderate temperature (220°C - 310°C), neutral, reduced? fluid	dilute (~5.5 wt. % NaCl equiv.) with trace CO <sub>2</sub> , moderate temperature (160°C - 300°C), neutral (~5.5), reduced fluid	dilute (?), moderate temperature (~200°C), neutral pH, reduced (?) fluid
<b>Characteristics of vein textures</b>	recrystallized crustiform, colloform, and cockade chalcodony, comb quartz, brecciation	recrystallized crustiform-colloform chalcodony, crystalline quartz, brecciation	crustiform, comb, and vuggy silica, brecciation, cryptocrystalline grey quartz	crustiform vein quartz in association with telluride and sulfide bands	crustiform, colloform chalcodony, massive quartz, brecciation
<b>Character of mineralization</b>	recrystallized colloform, cockade, crustiform chalcodony	Associated with intense brecciation, colloform bands, adularia needles	associated with vein breccia, wall rocks sericitized and chloritized, gold occurs as inclusions in pyrite	crustiform and replacement textures in association with veinlets of native gold and tellurides along with carbonates and other silicates	Adularia - quartz veins associated with breccia fragments with colloform, crustiform telluride, sulfide, selenide bands
<b>Metal association</b>	gold, silver, copper, electrum, minor (Zn, Pb, Cu, Fe, Ti) oxides / sulfides	gold, silver, electrum, Ag tellurides, minor (Zn, Pb, Cu, Fe) oxides sulfides	gold, (Au, Ag, Au-Ag, Pb, Hg) tellurides, (Zn, Pb, Cu, Fe) sulfides	(Au, Ag, Au-Ag, Ni, Pb, Hg) tellurides, (As, Zn, Pb, Cu, Fe) sulfides	electrum, (Fe, Cu, Sb, Ag- Se) sulfides, Ag selenides
<b>References</b>		Bobis <i>et al.</i> , 1995	Cooke and Bloom, 1990 Cooke <i>et al.</i> , 1996	Ahmad <i>et al.</i> , 1987	Isawa <i>et al.</i> , 1993 Nagayama, 1993

systems are apparent in the composition and properties of the proposed ore-bearing fluid (Table 9.2). Microthermometric studies and the analysis of thermal decrepitation residues provide evidence for the transport and deposition of ore in the Mallery Lake epithermal system by an oxidized, saline, slightly acidic, low temperature fluid. This ore-bearing fluid is very different from the ore-bearing fluid of the Phanerozoic low-sulfidation epithermal systems, as typically ore is transported by dilute, neutral, reduced to slightly oxidized fluid with moderate temperatures (Table 9.2). Under these conditions the most viable transport ligand would be by the hydrosulfide ion (Figure 9.1). Furthermore, the Mallery Lake epithermal system appears to be slightly different from the four mentioned Phanerozoic low-sulfidation systems in its relative abundance of oxide to sulfide minerals, although an oxide to sulfide ratio for the Mallery Lake epithermal system has not been quantitative. The low abundance of sulfides in the Mallery Lake epithermal system is consistent with the proposal that the sulfide ion was in low abundance, and under the proposed conditions had little involvement in the transport and deposition of ore. It would however be short sighted to totally dismiss the involvement of the bisulphide complex in the transport of precious metals as oxygen fugacities may have fluctuated through the life of the Mallery Lake hydrothermal system.

In summary, it is plausible that the chloride ion in the Type 2 saline fluid acted as the major ligand in transporting and depositing precious metals from the hydrothermal system in the Mallery Lake epithermal system, based on supporting

evidence provided by destructive and non-destructive fluid inclusion studies. The differences in the proposed ore-bearing fluid appears to be the only major feature that distinguishes the Proterozoic Mallery Lake vein system from the Phanerozoic low-sulfidation epithermal systems. No textural distinction can be made between the veins of the Mallery Lake and the Phanerozoic low-sulfidation epithermal systems, as the majority of the vein silica in the Mallery Lake vein system is proposed to have been transported and deposited by the dilute, higher temperature (Type 1) fluid (Chapter 6).

### **Age of the hydrothermal system**

Zircons from the Pitz Formation rhyolite flows (ATPR-2) and a syenite body of the Neultin Intrusive Suite (ATSD-1), both host rocks for the Mallery Lake epithermal deposit, were dated by the U – Pb method. A flow of the Pitz Formation was determined to have a minimum  $^{207}\text{Pb}/^{206}\text{Pb}$  emplacement age of  $1706\pm 7\text{Ma}$  whereas the uranium - lead systematics of the Neultin syenite indicate a range of possible ages between 1740 and 1762Ma (Chapter 7). Fluorite samples were also collected from the epithermal veins for determining a direct age for the mineralization event by the Sm-Nd method. These data form an isochron with an age of  $1435\pm 21\text{Ma}$  with an MSWD of 7.1 (Chapter 8). This substantial age difference between the host rocks and hydrothermal fluorite indicates that the Pitz Formation rhyodacites and the Neultin Intrusive Suite did not provide the heat source that drove the fluids involved in vein formation.

During the late 1970s and early 1980s there was a boom in exploration for uranium in Northern Canada. Exploration focussed heavily on the Athabasca basin of

Northern Saskatchewan and the Thelon basin, District of Keewatin, NWT. Radiometric analysis of many of the 20 major Athabasca basin uranium showings and deposits constrained the majority of hydrothermal ore precipitation to a period between 1330Ma and 1380Ma (Cumming and Krstic, 1992). One anomalous U-Pb age,  $1514 \pm 18$  Ma, was recorded as an early phase of uranium mineralization at the McArthur River deposit (Cumming and Krstic, 1992). Regional studies in the vicinity of the Thelon Basin, due to further uranium exploration, has resulted in the discovery of a hydrothermal event that may have begun as early as 1563 Ma and continued as late as 1300Ma (Hunt and Roddick, 1988; Davidson and Gandhi, 1989; Table 9.3). The mixing of the hydrothermal muscovite with older relic metamorphic alteration may have caused these suspect dates (Hunt and Roddick, 1988; 1992). Age data that are slightly younger than this range, as seen with GSC 88-49, may reflect an event caused by renewed fluid migration during the intrusions of the 1.27 Mackenzie diabase dykes (Hunt and Roddick, 1988; LeCheminant and Heaman, 1989). Miller *et al.* (1989) proposed that this hydrothermal event be tied to uranium deposition in the Schultz Lake area, and Kiggivik (Lone Gull). Kiggivik is an unconformity-type uranium deposit that occurs in fault zones that cut the extensively eroded metasedimentary basement of the Thelon basin (Fuchs and Hilger, 1989). Because uranium mineralization has been constrained to an age of  $1403 \pm 10$ Ma (i.e. pitchblende), Hunt and Roddick (1992) propose that regional fluid flow, causing the intense argillic alteration at Schultz Lake and Kiggivik, may have persisted after the period of ore deposition (Table 9.3). The uranium-lead analysis of the pitchblende from Kiggivik is close to the Sm-Nd age attained from the fluorite extractions of Mallery Lake.

**Table 9.3. Hydrothermal events recorded in the vicinity of the mid Proterozoic Thelon Basin**

Sample Location	Sample Number	Dating Method	Age data 2σ error	Host Rock Alteration	References
Kiggivik (Lone Gull)	GSC 88-47	K - Ar (whole rock)	1386±24 Ma.	Intensely altered & mineralized greywacke	Hunt & Roddick, 1988
"	GSC 88-44	K - Ar (whole rock)	1358±20 Ma.	Intensely altered & mineralized granite	"
"	"	K - Ar (whole rock)	1360±21 Ma.	"	"
"	"	K - Ar (whole rock)	1362±21 Ma.	"	"
"	GSC 88-45	K - Ar (whole rock)	1563±24 Ma.	Fine grained clay-bearing metagreywacke	"
"	?	U - Pb (Pitchblende)	1403±10 Ma.	Uranium Pitchblende ore	Fuchs & Hilger, 1989
NE Thelon basin (unconformity)	GSC 88-49	K - Ar (illite)	1266±31 Ma.	Extracted from a fluorapatite + illite + hematite/specularite + quartz cemented conglomerate	Hunt & Roddick, 1988
NE Thelon basin (100 m south of GSC 88- 49)	GSC 88-50	K - Ar (illite)	1386±37 Ma.	Illite from a massive banded specularite + fluorapatite vein hosted in a saprolitic metagreywacke	"
Schultz Lake (16 km of Kiggavik)	GSC 91-120	K - Ar (whole rock)	1395±13 Ma.	Intensely altered metagreywacke	Hunt & Roddick, 1991
"	GSC 91-121	K - Ar (whole rock)	1378±15 Ma.	Intensely altered quartz + feldspar porphyry	"
"	GSC 92-52	K - Ar (illite)	1335±16 Ma.	Intensely altered unfoliated granite	Hunt & Roddick, 1992
"	GSC 92-53	K - Ar (illite)	1347±13 Ma.	"	Hunt & Roddick, 1992
"	GSC 92-55	K - Ar (illite)	1344±17 Ma.	Intensely altered metapelite	Hunt & Roddick, 1992
"	GSC 92-54	K - Ar (illite)	1477±22 Ma.	Intensely altered pelitic metasediment interbedded arenaceous laminae	Hunt & Roddick, 1992
Boomerange Lake	?	U - Pb (whole rock)	1300±? Ma.	Porous, friable, fine to medium grained gray to dark gray sandstone	Davidson & Gandhi, 1989

Although speculative at this point, due to the lack of hydrothermal age data collected in the Keewatin, it is proposed that a regional fluid flow event may have been responsible for hydrothermal system development at Mallery Lake. The question as to what forces may have acted as a driving mechanism in triggering such extensive fluid flow on a regional scale is still under considerable debate.

## CHAPTER 10

### CONCLUSIONS

Two fluid populations (Type 1 and 2) were identified in the veins of the Mallery Lake epithermal system. The Type 1 fluid has moderate homogenization temperatures (typically between 150°C and 200°C), low salinity levels (~ 3 to 0 wt. %), and shows textural evidence of boiling in some samples. Also, the presence of clathrate melts and dawsonite ( $\text{NaAl}(\text{CO}_3)(\text{OH})_2$ ) pseudodaughter crystals were observed in some Type 1 fluid inclusions, indicating the presence of minor amounts of  $\text{CO}_2$ .

The Type 2 fluid is characterized by high salinities (23 to 31 wt. %),  $\text{CaCl}_2$ - $\text{NaCl}$  compositions, and low temperatures (90°C to 150°C). Studies conducted by Jaireth (1992) and Gammons *et al.* (1997) indicate that low temperature, saline, slightly acidic, oxidized fluids have great potential for the transport of precious metals as a chloro-complex. Furthermore, semi-quantitative EDS microprobe analyses of Type 2 fluid inclusion decrepitation residues reveal the presence of Ag-, Au-, Cu-salts, as well as the presence of iron. Because the Type 2 fluids satisfy these conditions, they are argued to be responsible for metal transport in the Mallery Lake epithermal system.

The average homogenization temperature of the Type 1 fluid is greater than that of the Type 2 fluid, and has potentially higher silica solubility. Boiling of the Type 1 fluid would drop the temperature of these fluids rapidly, causing a high rate of silica deposition. If the majority of the silica was deposited by this mechanism from Type 1 fluids, it is possible that the calculated stable isotope fluid values would dominantly reflect the



signature of these fluids. However, there may be no connection between the fluids that precipitated the silica and that which was responsible for precious metal deposition.

U-Pb dates for the Neultin Intrusive Suite and the Pitz Formation rhyolite flows in the Mallery Lake area indicate two magmatic events: an earlier intrusive event between  $1762 \pm 1$  Ma and  $1740 \pm 2$  Ma, and volcanism at  $1706 \pm 7$  Ma. The conclusion from this study is that, although the Pitz Formation flows and the Neultin Intrusive Suite appear to be associated geochemically, each may represent distinctly different magmatic events.

Sm-Nd analyses of fluorite extracted from the epithermal veins indicate an isochron age of  $1435 \pm 21$  Ma, interpreted as the age of the hydrothermal system. This age is consistent with the ages of other hydrothermal events from the Thelon and Athabasca basins. The difference between the age of the hydrothermal event and the host rocks of almost 300 Ma indicates that the host-rocks were not directly involved in ore formation. Instead, a large-scale regional hydrothermal event may have triggered the hydrothermal system in the Mallery Lake area.

Classifying the Mallery Lake epithermal system into a rigid framework has been avoided in this thesis as the system shows characteristics of low- and high-sulphidation systems. The abundance of sericite indicates a phyllic alteration assemblage that probably formed by the flow of the higher temperature, low salinity (Type 1) fluid. The cooler, saline, slightly acidic (Type 2) fluid is proposed to have locally leached the phyllic alteration mineral assemblage to kaolinite, and been responsible for ore transport and deposition. The transport of ore by a saline, oxidized, mildly acidic, lower temperature

fluid appears to be the major distinguishing factor that separates the Proterozoic Mallery Lake vein system from typical Phanerozoic low-sulfidation epithermal systems (Table 9.2).

### **Recommendations for further work**

Future work could be conducted on the Mallery Lake epithermal system in the following areas: (1) A drill program would allow for a new dimension of the deposit to be studied, as all work to this point has been done from surficial mapping and sample collection. Core attained from a drilling program would aid in further interpretation of the physical and chemical conditions of the fluids involved in ore transport and deposition. (2) Laser ablation ICP-MS stable isotope analysis would be a valuable tool in obtaining information regarding the elemental concentrations of individual fluid inclusions. (3) Although hydrothermal mineral ages in the Thelon, Athabasca, and Baker Lake Basins indicate a possible correlation, the question as to possible tectonic events (i.e. an orogenic or anorogenic event) that could trigger such a wide spread hydrothermal disturbance remains unaddressed.

## References

- Ahmad, M., Solomon, M., and Walshe, J.L. 1987. Mineralogical and geochemical studies of the emperor gold telluride deposit, Fiji. *Economic Geology*, **82**: 345-370.
- Aspler, L.B. 1989. Sedimentology, structure, and economic geology of the Poorfish-Windy thrust-fold belt, Ennadai Lake area, District of Keewatin, and the shelf to foredeep transition in the foreland of Trans-Hudson Orogen. *In* Current research, part C. Geological Survey of Canada, Paper 89-1C, pp. 143-155.
- Berger, B.R. and Henley, R.W. 1989. Advances in the understanding of epithermal gold-silver deposits, with special reference to the western United States. *Economic Geology*, Monograph 6, pp. 405-423.
- Biczok, J.L. 1996. 1996 exploration report: Mallery Lake project. Assessment report on behalf of Phelps Dodge, Corporation of Canada, Limited.
- Blake, D.H. 1980. Volcanic rocks of the Paleohelikian Dubawnt Group in the Baker Lake-Angikuni Lake area, District of Keewatin, NWT. *In* Geological Survey of Canada, Bulletin 309.
- Bobis, R.E. 1994. A review of the description, classification and origin of quartz textures in low sulphidation epithermal veins. *Journal of the Geological Society of the Philippines*. Vol. 99, 1: 15 - 39.
- Bobis, R.E., Morrison, G.W., and Jaireth, S. 1995. Anatomy of a Carbonaceous epithermal ore shoot at Pajingo, Queensland: settings, zoning, alteration, and geochemistry: *Economic Geology*, **90**: 1776-1798.
- Bodnar, R.J., Reynolds, T.J., and Kuehn, C.A. 1985. Fluid inclusion systematics in epithermal systems. *In* Geology and geochemistry of epithermal systems. *Edited by* B.R. Berger, and P.M. Bethke. *Reviews in Economic Geology*, Vol. 2, pp. 73-97.
- Bodnar, R.J., and Vityk, M.O. 1995. Interpretation of microthermometric data for H<sub>2</sub>O-NaCl fluid inclusions. *In* Fluid Inclusions in Minerals: Methods and Applications. *Edited by* B. De Vivo, and M.L. Frezzotti. Short Course, pp. 117-130.
- Bohm, C.O., Heaman, L.M., and Corkery, M.T. 1999. Archean crustal evolution of the northwestern Superior craton margin: U-Pb zircon results from the Split Lake Block. *Canadian Journal of Earth Sciences*. (in press).

- Bonham, H.F., Jr. 1986. Models for volcanic-hosted epithermal precious metal deposits; A review. *In* Volcanism, hydrothermal systems and related mineralization. International Volcanological Congress, Symposium 5, Hamilton, New Zealand, 1986, Proceedings: University of Auckland Centre for Continuing Education, Auckland, N.Z., pp. 13-17.
- Boyle, R.W., 1961. Geology, geochemistry and origin of the gold deposits of the Yellowknife district, Northwest Territories. *In* Geological Survey of Canada, Bulletin 280.
- Brown, P.E. 1998. Fluid inclusion modelling for hydrothermal systems. *In* Techniques in hydrothermal ore deposits geology. Edited by J. P. Richards, and P. B. Larson. Reviews in Economic Geology, Vol. 10, pp. 151-171.
- Brownlow, A.H., 1996. Geochemistry. 2<sup>nd</sup> ed. Prentice-Hall Canada, Toronto.
- Bruce, E.L. 1941. Concentrated saline water from the Sturgeon River Gold Mines. *In* Transactions of the Royal Society of Canada, Vol. 35, pp. 25-29.
- Candela, P.A. 1997. A Review of shallow, ore-related granites: textures, volatiles, and ore metals. *Journal of Petrology*, Vol. 38, 12: 1619-1633.
- Chesley, J.T., Halliday, A.N., Kyser, T.K., and Spry, P.G. 1994. Direct dating of Mississippi Valley-Type mineralization: Use of Sm-Nd in fluorite. *Economic Geology*, 89: 1192-1199.
- Chesley, J.T., Halliday, A.N., and Scrivener, R.C. 1991. Samarium-Neodymium direct dating of fluorite mineralization. *Science*, 252: 949-951.
- Christiansen, E.H., Sheridan, M.F., and Burt, D.M. 1986. The geology and geochemistry of Cenozoic Topaz Rhyolites from the Western United States. Geological Society of America, Special Paper 205.
- Clayton, R.N., O'Neil, J.R., and Mayeda, T.K. 1972. Oxygen isotope exchange between quartz and water. *Journal of Geophysical Research*, 77: 3057-3067.
- Cooke, D.R., and Bloom, M.S. 1990. Epithermal and subjacent porphyry mineralization, Acupan, Baguio District, Philippines: a fluid-inclusion and paragenetic study. *Journal of Geochemical Research*, 35: 297-340.

- Cooke, D.R., McPhail, D.C., and Bloom, M.S. 1996. Epithermal gold mineralization, Acupan, Baguio District, Philippines: geology, mineralization, alteration, and the thermochemical environment of ore deposition. *Economic Geology*, **91**: 243-272.
- Coplen, T.B., Kendall, C., and Hopple, J. 1983. Comparison of stable isotope reference samples. *Nature*, **302**: 236-238.
- Cumming, G.L., and Krstic, D. 1992. The age of unconformity-related uranium mineralization in the Athabasca Basin, northern Saskatchewan. *Canadian Journal of Earth Sciences*, **29**: 1623-1639.
- Davidson, G.I. and Gandhi, S.S. 1989. Unconformity-related U-Au Mineralization in the Middle Proterozoic Thelon sandstone, Boomerang Lake Prospect, Northwest Territories, Canada. *Economic Geology*, **84**: 143-157.
- Davis, D. W., Lowenstein, T. K. and Spencer, R. J. 1990. Melting behavior of fluid inclusions in laboratory-grown halite crystals in the systems NaCl-H<sub>2</sub>O, NaCl-KCl-H<sub>2</sub>O, NaCl-MgCl<sub>2</sub>-H<sub>2</sub>O and NaCl-CaCl<sub>2</sub>-H<sub>2</sub>O. *Geochimica et Cosmochimica Acta*, **54**: 591-601.
- Donaldson, J.A. 1965. The Dubawnt Group, Districts of Keewatin and Mackenzie. *In* Geological Survey of Canada, Paper 64-20.
- Donaldson, J.A. 1969. Descriptive Notes (with particular reference to the late Proterozoic Dubawnt Group) to accompany a geological map of central Thelon Plane, District of Keewatin and Mackenzie (65M, N W 1/2, 66B, C, D, 75P E 1/2, 76 A E 1/2) *In* Report of Activities, Paper 68-49.
- Dong, G., Morrison, G., and Jaireth, S. 1995. Quartz textures in epithermal veins, Queensland - classification, origin and implication. *Economic Geology*, **90**: 1841-1856.
- Dowling, K., and Morrison, G.W. 1989. Application of quartz texture to the classification of gold deposits using North Queensland examples. *Economic Geology Monograph* 6, pp. 342-355.
- Dube, B., Dunning, G., and Lauziere, K. 1998. Geology of the Hope Brook Mine, Newfoundland, Canada: A preserved late Proterozoic high-sulfidation epithermal gold deposit and its implications for exploration. *In* *Economic Geology*, **93**: 405-436.

- Dudas, F.O., LeCheminant, A.N., and Sullivan, R.W. 1991. Reconnaissance Nd isotopic study of granitoid rocks from the Baker Lake region, District of Keewatin, N.W.T., and observations on analytical procedures. *In* Radiogenic age and isotopic studies, report 4. Geological Survey of Canada, Paper 90-2, pp. 101-112
- Evans, A.M. 1993. Ore geology and industrial minerals: an introduction. 3<sup>rd</sup> ed. Blackwell Scientific Publications, London.
- Faure, G. 1986. Principles of Isotope Geochemistry. 2<sup>nd</sup> ed. John Wiley & Sons, New York.
- Feng, R., and Abercrombie, H.J. 1994. Disseminated Au-Ag-Cu mineralization in the Western Canadian Sedimentary Basin, Fort MacKay, northeastern Alberta: a new gold deposit type. *In* Current Research, part E. Geological Survey of Canada, paper 1994-E, pp. 121-132.
- Fournier, R.O. 1985. The behaviour of silica in hydrothermal solution. *In* Geology and geochemistry of epithermal systems. *Edited by* B.R. Berger, and P.M. Bethke. Reviews in Economic Geology, Vol. 2, pp. 45-61.
- Frape, S.K., and Fritz, P. 1982. The chemistry and isotopic composition of saline groundwaters from the Sudbury Basin, Ontario. *In* Canadian Journal of Earth Sciences, 19: 645-661.
- Frape, S.K., and Fritz, P. 1987. Geochemical trends for groundwaters from the Canadian Shield. *In* Saline water and gases in crystalline rocks. *Edited by* P. Fritz, and S. K. Frape. Geological Association of Canada Special Paper 33, pp. 19-38.
- Frape, S.K., and Fritz, P., and McNutt, R.H. 1984. Water-rock interaction and chemistry of groundwaters from the Canadian shield. *In* Geochimica et Cosmochimica Acta, 48: 1617-1627.
- Fuchs, H.D. and Hilger, W. 1989. Kiggavik (Lone Gull): An unconformity related uranium deposit in the Thelon Basin, Northwest Territories, Canada. *In* Uranium Resources and Geology of North America, International Atomic Energy Agency, IAEA-TECDOC-500, pp. 429-454.
- Gall, Q., Peterson, T.D., and Donaldson, J.A. 1992. A proposed revision of Early Proterozoic stratigraphy of the Thelon and Baker Lake basins, Northwest Territories. *In* Current Research, part C. Geological Survey of Canada, Paper 92-1 C, pp. 129-137.

- Gammons, C.H., Yu, Y., and Williams-Jones, A.E. 1997. The disproportionation of gold(I) chloride complexes at 25 to 200°C. *Geochimica et Cosmochimica Acta*, **61**: 1971-1983.
- Gilber, J.M., and Park, C.F. Jr. 1986. *The geology of ore deposits*. W.H. Freeman and Company, New York.
- Goldstein, R.H., and Reynolds, T.J. 1994. Systematics of fluid inclusions in diagenetic minerals: SEPM Short Course, Vol. 31.
- Goldstein, S.L., O'Noin, R.K., and Hamilton, P.J. 1984. A Sm – Nd study of atmospheric dust and particulates from major river systems. *Earth Planetary Scientific Letters*, **70**: 221-236.
- Guha, J., and Kanwar, R. 1987. Vug brines-fluid inclusions: A key to the understanding of secondary gold enrichment processes and the evolution of deep brines in the Canadian shield. *In Saline water and gases in crystalline rocks. Edited by P. Fritz, and S. K. Frape. Geological Association of Canada Special Paper 33, pp. 89-101.*
- Hallberg, A. 1994. The Enåsen gold deposit, central Sweden. *Mineral Deposita*, **29**: 150-162.
- Halliday, A.N., Shepherd, T.J., Dickin, A.P., and Chesley, J.T. 1990. Sm-Nd evidence for the age and origin of a Mississippi Valley Type ore deposit. *Nature*, **344**: 54-56.
- Heald, P., Foley, N.K., Hayba, D.O. 1987. Comparative Anatomy of Volcanic-Hosted Epithermal Deposits: Acid-Sulfate and Adularia-Sericite Types. *In Economic Geology*, **82**: 1-26.
- Heaman, L.M., and Parrish, R. 1991. U-Pb geochronology of accessory minerals. *In Applications of Radiogenic Isotope Systems to Problems in Geology. Edited by L.H. Heaman, and J.N. Ludden. Mineralogical Association of Canada, Short Course Handbook, Vol. 19.*
- Hedenquist, J.W. 1987. Mineralization associated with volcanic-related hydrothermal systems in the circum-Pacific Basin. *In Transactions of the Fourth Circum-Pacific Energy and Mineral Resources Conference, Singapore. Edited by M.K. Horn. American Association of Petroleum Geologists, pp. 513 – 524.*
- Henley, R.W. 1985. *The Geothermal Framework of Epithermal Deposits. Geology and Geochemistry of Epithermal Systems. Edited by B.R. Berger, and P.M. Bethke. The Economic Geology Publishing Company, Vol.2, pp. 1-24.*

- Henley, R.W. and Brown, K.L. 1985. A practical guide to the thermodynamics of geothermal fluids and hydrothermal ore deposits. *In* Geology and geochemistry of epithermal systems. *Edited by* B.R. Berger, and P.M. Bethke. *Reviews in Economic Geology*, Vol. 2, pp. 45-61.
- Hunt, P.A., and Roddick, J.C. 1988. A composition of K – Ar ages, report 18. *In* Radiogenic age and isotopic studies: Report 2. Geological Survey of Canada, Paper 88-2, pp. 127-153.
- Hunt, P.A., and Roddick, J.C. 1991. A composition of K – Ar ages, report 21. *In* Radiogenic age and isotopic studies: Report 5. Geological Survey of Canada, Paper 91-2, pp. 242-243.
- Hunt, P.A., and Roddick, J.C. 1992. A composition of K – Ar ages, report 22. *In* Radiogenic age and isotopic studies: report 6. Geological Survey of Canada, Paper 92-2, pp. 199-201.
- Izawa, E., Kurihara, M., and Itaya, T. 1993. K-Ar ages and the initial Ar isotopic ratio of adularia-quartz veins from the Hishikari gold deposit, Japan. *In* High grade epithermal gold mineralization: The Hishikari deposit. *Edited by* N. Shikazono, K. Naito, and E. Izawa. *Resource Geological Special Issue*, No. 14, 1993. The Society of Resource Geology. pp. 63-70.
- Jacobsen, S.B., and Wasserburg, G.J. 1980. Sm – Nd isotopic evolution of chondrites. *Earth and Planetary Scientific Letters*, **50**: 139–155.
- Jaffey, A.H., Flynn, K.F., Glendenin, L.E., Bentley, W.C., and Essling, A.M. 1971. Precision measurements of half-lives and specific activities of  $^{235}\text{U}$  and  $^{238}\text{U}$ . *Physics Reviews C*. **4**: p. 1889-1906.
- Jaireth, S. 1992. The calculated solubility of platinum and gold in oxygen-saturated fluids and the genesis of platinum and gold mineralization in the unconformity-related uranium deposits. *Mineralium Deposita*, **27**: 42-54.
- Krogh, T.E. 1982. Improved accuracy of U – Pb zircon ages by the creation of more concordant systems using an air abrasion technique. *Geochimica et Cosmochimica Acta*, **46**: 637-649.
- Kyser, T.K. 1987. Equilibrium Fractionation Factors for Stable Isotopes. *In* MAC Short Course in Stable Geochemistry of Low Temperature Fluids. Edited by T.K. Kyser, Saskatoon, Vol.13, pp.1-76.
- Langford, G.B., and Hancox, E.G. 1936. Hypogene anhydrate from the McIntyre mine, Porcupine district, Ontario: *Economic Geology*, **31**: pp. 600-609.



- Layton-Matthews, D. 1997. The Agate Zone, Mallery Lake Epithermal System, District of Keewatin, NWT: A Petrographic, Lithochemical, and Alteration Study of the Pitz Formation. Undergraduate Thesis, University of Manitoba, Manitoba.
- LeCheminant, A.N., and Heaman, L.M. 1989. Mackenzie igneous events, Canada; middle Proterozoic hotspot magmatism associated with ocean opening. *Earth and Planetary Science Letters*, **96**: 1-2, pp. 38-48.
- LeCheminant, A.N., Lambert, M.B., and Booth, G.W. 1979. Geological studies, Tebesjuak Lake area, District of Keewatin. *In* Current Research, Part A, Geological Survey of Canada, Paper 79-1A, pp. 179-186.
- LeCheminant, A.N., Miller, A.R., Booth, G.W., Murray, M.J., and Jenner, G.A. 1980. Geology of the Tebesjuak Lake Map Area, District of Keewatin: A progress Report with notes on Uranium and Base Metal Mineralization. *In* Current Research, Part A, Geological Survey of Canada, Paper 80-1A, pp. 339-346.
- LeCheminant, A.N., Ianelli, T.R., Zaitlin, B., and Miller, A.R. 1981. Geology of the Tebesjuak Lake Area, District of Keewatin: A Progress Report. *In* Current Research, Part B, Geological Survey of Canada, Paper 81-1B, pp. 113-128.
- LeCheminant, A.N., Jackson, M.J., Galley, A.G., Smith, S.L., and Donaldson, J.A. 1984. Early Proterozoic Amer Group, Beverly Lake Map Area, District of Keewatin. *In* Current Research, Part B, Geological Survey of Canada, Paper 84-1B, pp. 159-172.
- LeCheminant, A.N., Miller, A.R., and LeCheminant, G.M. 1987a. Early Proterozoic alkaline igneous rocks, District of Keewatin, Canada: petrogenesis and mineralization. *In* Geochemistry and mineralization of Proterozoic volcanic suites. *Edited by* T.C. Pharaoh, R.D. Beckinsale, and D. Richard. Geological Society of London, Special Publication 33, pp.219-240.
- LeCheminant, A.N., Roddick, J.C., and Henderson, J.R. 1987b. Geochronology of Archean and early Proterozoic magmatism in the Baker Lake – Wager Bay region, N.W.T. Geological Association of Canada and Mineralogical Association of Canada, Program with Abstracts, Vol. 12.
- Lofgren, G. 1970. Experimental devitrification rate of rhyolite glass, *Geological Society of America Bulletin*, **81**: 553-560.
- Lofgren, G. 1971a. Spherulitic textures in glassy and crystalline rocks. *Journal of Geophysical Research*, Vol. 76, **23**: 5635-5648.

- Lofgren, G. 1971b. Experimentally produced devitrification textures in natural rhyolitic glass. *Geological Society of America Bulletin*, **82**: 111-124.
- Loveridge, W.D., Eade, K.E., and Roddick, J.C. 1987. A U-Pb age on zircon from a granite pluton, Kamilukuak Lake Area, District of Keewatin, establishes a lower limit for the age of the Christopher Island Formation, Dubawnt Group. *In Radiogenic Age and Isotopic Studies: Report 1*, Geological Survey of Canada, Paper 87-2, pp. 67-71.
- Ludwig, K.R. 1998. Isoplot /Ex, a geochronological toolkit for Microsoft Excel, version 1.00 b: Berkeley Geochronology Center, Special Publication No.1.
- Mernagh, T.P., Heinrich, C.A., Leckie, J.F., Carville, D.P., Gilbert, D.J., Valenta, R.K., and Wyborn, L.A.I. 1994. Chemistry of low-temperature hydrothermal gold, platinum, and palladium ( $\pm$ uranium) mineralization at Coronation Hill, Northern Territory, Australia. *Economic Geology*, **89**: 1053-1073.
- Miller, A.R., Cumming, G.L., and Krstic, D. 1989. U-Pb, Pb-Pb, and K-Ar isotopic study and petrography of uraniferous phosphate-bearing rocks in the Thelon Formation, Dubawnt Group, Northwest Territories, Canada. *Canadian Journal of Earth Sciences*, **26**: 867-880.
- Muehlenbachs, K., Burwash, R.A., and Chacko, T. 1994. The oxygen and hydrogen isotope composition of Alberta basement rocks: Possible implications for crustal structure and paleogeographic reconstructions of the basement terrains. *In Lithoprobe: Alberta basement transects. Report of transect workshop, February 14-15, 1994. Ramada Hotel, Calgary. Lithoprobe Report #37.*
- Nagayama, T. 1993. Pressure loss, boiling and vein formation: An example model for the mineral precipitation in the Hishikari vein deposits. *In High grade epithermal gold mineralization: The Hishikari deposit. Edited by N. Shikazono, K. Naito, and E. Izawa. Resource Geological Special Issue, No. 14, 1993. The Society of Resource Geology. pp. 29-36.*
- Naldrett, D.L., Lachaine, A., and Naldrett, S.N. 1987. Rare-Earth elements, thermal history, and the colour of natural fluorites. *Canadian Journal of Earth Sciences*, **24**: 2082-2088.
- Oakes, C. S. Bodnar, R. J. and Simonson, J. M. 1990. The system NaCl-CaCl<sub>2</sub>-H<sub>2</sub>O: I. The ice liquidous at 1 atm. pressure. *Geochimica et Cosmochimica Acta*, **54**: 603-610.

- Oakes, C. S., Sheets, R. W., Bodnar, R. J., and Simonson, J. M. 1992. (NaCl+CaCl<sub>2</sub>)<sub>aq</sub>: Phase equilibria and volumetric properties: (extended abstract) PACROFI IV Abstracts with Program, pp. 128-132.
- Oldow, J.S., Bally, A.W., Ave Lallemand, H.G., and Leeman, W.P. 1989. Phanerozoic evolution of the North American Cordillera; United States and Canada, *In* Bally, A.W., and Palmer, A.R., eds., *The Geology of North America - An overview*: Boulder, Colorado, Geological Society of America, *The Geology of North America*, Vol. A, pp. 139-232.
- O'Neil, J.R. 1986. Theoretical and experimental aspects of isotope fractionation. *In* *Stable isotopes in high temperature geologic processes*. Edited by J.W. Valley, H.P. Taylor, Jr., and J.R. O'Neil. Mineralogical Society of America, Washington, D.C. pp. 1-40.
- Panteleyev, A. 1994. A Canadian Cordilleran model for epithermal gold-silver deposits. *In* *Ore deposit models*. Edited by R.G. Roberts, and P.A. Sheahan. Reprint Series 4: Geoscience Canada, St. John's, Newfoundland. pp. 31-43.
- Peterson, T.D. 1992. Early Proterozoic ultrapotassic volcanism of the Keewatin Hinterland, Canada. *In* *Proceedings, 5th International Kimberlite Conference: Kimberlites, related rocks and mantle xenoliths*. Edited by H.O.A. Meyer, and O.H. Leanardos. CPRM, Vol. 1, Brasilia, pp. 221-235.
- Peterson, T.D., Born, P. 1994. Archean and Lower Proterozoic geology of western Dubawnt Lake, Northwest Territories. *In* *Current Research 1994-C*. Geological Survey of Canada, pp. 157-164.
- Peterson, T.D., Esperança, S., LeCheminant, A.N. 1994. Geochemistry and origin of the Proterozoic ultrapotassic rocks of the Churchill Province, Canada. *Mineralogy and Petrology*, **51**: 251-276.
- Peterson, T.D., LeCheminant, A.N., Rainbird, R.H. 1989. Preliminary report on the geology of northwestern Dubawnt Lake area, District of Keewatin, N.W.T. *In* *Current Research, Part C*. Geological Survey of Canada, Paper 89-1C, pp. 173-183.
- Peterson, T.D., Rainbird, R.H. 1990. Tectonic and petrological significance of Regional lamproite-minette volcanism on the Thelon and Trans-Hudson hinterlands, Northwest Territories. *In* *Current Research Part C*, Geological Survey of Canada, Paper 90-1C, pp. 69-79.

- Peterson, T.D., and van Breemen, O. 1999. Review and progress report of Proterozoic granitoid rocks of the western Churchill Province, Northwest Territories (Nunavut). *In* Current Research 1999-C. Geological Survey of Canada, pp. 119-127.
- Rainbird, R.H., Peterson, T.D. 1990. Physical volcanology and sedimentology of lower Dubawnt Group strata, Dubawnt Lake, District of Keewatin, N.W.T. *In* Current Research Part C. Geological Survey of Canada, Paper 90-1C, pp. 207-217.
- Roedder, E. 1984. Fluid inclusions. Mineralogical Society of America, Reviews in Mineralogy, Vol. 12.
- Rogers, P.J. 1978. Fluid inclusion studies on fluorite from the Askrigg Block. *In* Transactions/Section B. Institute of Mining and Metallurgy, Vol 87, pp. B125-B131.
- Rollinson, H. 1993. Using Geochemical Data: Evaluation, Presentation, Interpretation. Addison Wesley Longman Limited, Essex.
- Saunders, J.A. 1990. Colloidal transport of gold and silica in epithermal precious-metal systems: Evidence from the Sleeper deposits, Nevada. *Geology*, **18**: 757-760.
- Seward, T.M. 1991. The hydrothermal geochemistry of gold. *In* Gold metallogeny and exploration. *Edited by* R.P. Foster, Blackie and Son, Glasgow, pp. 37-62.
- Seward, T.M. and Barnes, H.L. 1997. Metal transport by hydrothermal ore fluids. *In* Geochemistry of hydrothermal ore deposits. *Edited by* H.L. Barnes. pp. 435-486.
- Sillitoe, R.H. 1993. Epithermal models: genetic types, geometrical controls and shallow features. *In* Mineral Deposit Modeling. *Edited by* R.V. Kirkham, W.D. Sinclair, R.I. Thorpe, and J.M. Duke. Geological Association of Canada, Special Paper 40, pp. 403-417.
- Spencer, R.J., Lowenstein, T.K. 1992. Phase equilibria in the system  $MgCl_2-H_2O$ : (extended abstract) PACROFI IV Abstracts with Program, pp. 138-141.
- Stacey, J.S., and Kramers, J.D. 1975. Approximation of terrestrial lead isotope evolution by a two-stage model. *Earth and Planetary Science Letters* **26**: 207-221.

- Taylor, B.E. 1996. Epithermal gold deposits. *In* Geology of Canadian mineral deposit types. *Edited by* O.R. Eckstrand, W.D. Sinclair, and R.I. Thorpe. Geological Survey of Canada, No. 8, pp. 329-350.
- Taylor, S.R., and McLennan, S.M. 1985. The continental crust: its composition and evolution. Blackwell, Oxford.
- Tella, S., HeyWood, W.W., and Loveridge, W.D. 1985. A U - Pb age on zircon from a quartz syenite intrusion, Amer Lake, District of Keewatin, NWT. Geological Survey of Canada, Paper 85-1B, pp. 367-370.
- Touret, J.L.R. 1995. Fluid inclusions in sedimentary and diagenetic environments. *In* Fluid Inclusions in Minerals: Methods and Applications. *Edited by* B. De Vivo, and M.L. Frezzotti, Short Course, pp. 251 – 269.
- Vanko, D. A., Bodnar, R. J. and Sterner, S. M. 1988. Synthetic fluid inclusions: VIII. Vapor-saturated halite solubility in part of the system NaCl-CaCl<sub>2</sub>-H<sub>2</sub>O, with application to fluid inclusions from oceanic hydrothermal systems. *Geochimica et Cosmochimica Acta*, **52**: 2451-2456.
- Wasserburg, G.L., Jacobsen, D.J., DePaulo, M.T., and Wen, T. 1981. Precise determination of Sm/Nd ratios, Sm and Nd isotope abundances in standard solutions. *Geochimica et Cosmochimica Acta*, **45**: 2311-2323.
- Watkinson, D.H, and Melling, D.R. 1992. Hydrothermal origin of platinum-group mineralization in low-temperature copper sulfide-rich assemblages, Salt Chuck Intrusion, Alaska. *Economic Geology*, **87**: 175-184.
- Were, Jr., R.W., Bodnar, R.J., Bethke, P.M., and Barton, Jr., P.B. 1979. A novel gas-flow fluid inclusion heating/freezing stage (abst.). *Geological Society of America Abstracts and Programs*, **11**:539.
- White, N. 1995. Clay Alteration: Its significance for Exploration. BHP unpublished report.
- White N.C., Hedenquist, J.W. 1990. Epithermal environments and styles of mineralization: variations and their causes, and guidelines for exploration. *In* *Journal of Geochemical Exploration*, **36**: 445-474.
- Wilkinson, J.J., Boyce, A.J., Earls, G., and Fallick, A.E. 1999. Gold remobilization by low-temperature brines: Evidence from the Curraghinalt Gold Deposit, Northern Ireland. *Economic Geology*, **94**: 289–296.
- Wilson, M. 1989. *Igneous Petrogenesis: A global tectonic approach*. Chapman & Hall, London.

Yanatieva, O.K. 1946. Polytherms of solubility of salts in the tropic system  
CaCl<sub>2</sub>- MgCl<sub>2</sub>-H<sub>2</sub>O and CaCl<sub>2</sub>-NaCl-H<sub>2</sub>O. Zhur. Prikl. Khim, 19: 709-  
722.